SURFACE CHEMISTRY ON THE HETEROGENEOUS METAL SURFACE INVESTIGATED BY THE SUM FREQUENCY GENERATION MICROSCOPE

A Dissertation Presented to

The Faculty of the Department of Chemistry

University of Houston

In Partial Fulfillment

of the Requirements for the Degree

Doctor of Philosophy

By

Ming Fang

May 2016

SURFACE CHEMISTRY ON THE HETEROGENEOUS METAL SURFACE INVESTIGATED BY THE SUM FREQUENCY GENERATION MICROSCOPE

Ming Fang

APPROVED:

Dr. Steven Baldelli, Chairman

Dr. Shoujun Xu

Dr. Ding-Shyue (Jerry) Yang

Dr. Jeremy May

Dr. Lars C. Grabow

Dr. Dan Wells, Dean
College of Natural Science and Mathematics

“If a cluttered desk is a sign of a cluttered mind, of what, then, is an empty desk a sign?”

-Albert Einstein

ACKNOWLEDGEMENTS

After I graduated from college, I started my Ph.D. program of Physical Chemistry in University of Houston from the 2011 spring semester. During the past five years in United States, I find myself in a new way. I learnt not only the Physical Chemistry but also the American culture and sophisticated view about life. Finishing the Ph.D. program and obtaining the Ph.D. degree only mean a new start of a new kind of life. An unknown future with dream makes me very excited.

In these five years, I would like to thank the previous group members in Prof. Baldelli's group including Greggy, Joonhee and Xiaojun at first. They were very kind to me and taught me a lot experimental knowledge such as laser, UHV, and microscope, when I started to perform research. They helped me to accommodate the research life very quickly. I also want to thank Desheng for showing me the mystery of microscopy. Before he joined our group, I thought that microscopy is simple. But then I realized that I just knew too less for getting a comprehensive understanding of the mysterious microscopy. Besides that, I also want to thank Desheng, Zhe, Michelle, and Daniela who made my life in the lab less boring than usual.

My special thanks to Dr. Steven Baldelli for the guidance and support throughout this endeavor. Thank you for your valuable knowledge and never-ending passion for Science which always encourage me to keep forwarding.

To all of the present and past time in the University of Houston, I had the pleasure to enjoy my graduate school time with Siheng, Yuanyuan, Pengzhi, Qiongzheng and

Dengke. I thank you for all the great time, parties and friendship. I would like to express the huge thank to my sister Yan. You bring me a lot unusual insight to my life.

Last, but certainly not the least, I dedicate this work to my family, my parents. The constant and strong encouragement and support from my family made me strong enough to achieve my goals and aspirations in life. Best wishes with my family and loved ones.

ABSTRACT

Various surface phenomena, which are closely related to catalysis, corrosion, biology, etc., occur at a metal surface specifically due to unique nature of surface. Sum Frequency Generation (SFG) microscopy has been established as a powerful technique to investigate surface chemistry on heterogeneous metal surface. In this present work, the possibility about extending the application of SFG microscopy is described in detail.

A new-generation SFG imaging setup with an improved spatial resolution and data acquisition speed has been developed and presented in the second chapter. In addition, the SFG theory and other experimental setups are introduced in the first two chapters. The main part of research presented in this thesis is about that the self-assembled monolayer of octadecanethiol (ODT) on the microcrystalline copper surface. The crystal grain and grain boundaries of the microcrystalline copper surface are mapped in the SFG image based on the strong brightness contrast of the SFG signal across the boundary. Local SFG spectra reveal significant difference with each other, as well as with the average SFG spectra, indicating the heterogeneity of the monolayer results from the copper grains with distinct crystallographic facets and orientations on copper surface. In addition, the statistical orientation analysis of amplitude ratio of CH_3-sym/CH_3-asym and corresponding contour maps imply that the orientation of ODT molecules is affected by the underlying copper. This work demonstrates that SFG imaging is a good approach to build the local spatial correlation of the optical non-resonant response of the metal surface to the conformation and orientation of the local adsorbed molecule. Besides that, the adsorption of near-atmospheric pressure methanol on the polycrystalline copper surface is investigated by

SFG imaging. Methoxy is found as a stable intermediate which stably and abundantly exists on the metal surface. The pre-adsorbed oxygen promotes the dissociation of methanol with formation of a more ordered and higher density methoxy monolayer on copper surface. Another system studied by SFG imaging is the CO adsorption on a polycrystalline platinum surface. The stretching vibration mode from linearly bonded of CO adsorbed on the platinum surface is identified by the SFG spectra. The resonant frequency of CO stretching vibration varies on the different crystal domain areas.

The significant advantage of SFG microscopy over averaged SFG spectroscopy, as well as other surface techniques, is demonstrated in its ability to spatially correlate local molecular behaviors in response to the local properties of the metal surface. This work further demonstrates the powerful capability of SFG microscopy in characterizing molecular behaviors on the metal surfaces, as well as exploits the potential in analyzing surface chemistry on a heterogeneous metal surfaces.

TABLE OF CONTENTS

Chapter 2. Theory and Experimentation

Appendix D:

LIST OF FIGURES

LIST OF TABLES

CHAPTER 1. Introduction

1.1. Surface chemistry and its application on the metal surface

Ninety five years ago, Irving Langmuir made a statement in a famous paper about the heterogeneous catalysis which has been regarded as the birth of surface science: "Most finely divided catalysts must have structures of great complexity".[1] Normally, the surface/ interface is defined as the boundary separating any two different phases of matters, such as a solid-liquid interface, a solid-gas interface, or a liquid-gas interface, etc. Two kinds of immiscible liquids could also form an interface between each other, such as a water/oil interface. An interface consists of the top 2-10 atomic or molecular layers where the physical properties such as the atom structures are significantly different from the bulk media.[2] The uneven forces between molecules across the interfacial layer determined the unique properties and structures of interfaces.[3] All chemical and physical processes involve molecules crossing the interface, even though the number of molecules or atoms exposed at the interface are relatively small compared with the bulk media. Various surface phenomena, which are closely related with industry and practical applications, such as surfactants, heterogeneous catalysis, semiconductor device fabrication, fuel cells, self-assembled monolayers, and adhesives, occurred at the interface specifically due to its unique nature. It is therefore vital that the molecular properties and behaviors at the interface be thoroughly understood. Surface science is not only fundamentally but also practically important.

Metals are materials with good electrical and thermal conductivity, and have been widely used in our environment. About 91 of the 118 elements in the periodic table are

metallic (some elements appear in both metallic and non-metallic forms). Most metals interact with the surrounding environments through various chemical processes, which occur as a chemical reaction on the metal surface. These chemical processes are seen in industry and the natural world. For example, the atmospheric corrosion of stainless steels could be eliminated by a highly protective chromium oxide coating treatment. The noble-metal catalysts in the car converter removes most of the worst output of the combustion engine such as nitrogen oxide.[4] Hence, the precise understanding about the metal surface reactivity would determine how well the metal material behaves in its intended function. In terms of the inherent complexity of these practical chemical processes, it imposes high demands on the analytical method in order to comprehensively understand the surface chemistry on metal surfaces.

Despite the significant importance of metal surfaces in both fundamental science and technological applications, the understanding of chemical reactions and molecular behavior on metal surfaces is still primitive, especially at the atomic or molecular level. This arises from the fact that the metal interface is complex resulting from factors including oxidation, defects, and grain structures. Moreover, the chemical species of the interface, which play an important role in influencing surface reactivity, present in very low concentrations. Consequently, it is highly demanding for a surface technique which is able to derive its signal as near exclusively as possible from within the top surface range. In today's world with the development of techniques such as x-ray photoelectron spectroscopy (XPS), secondary ion mass spectrometry (SIMS), and auger electron spectroscopy (AES), a significant impact on metal surface research has been achieved and benefitted strongly for both fundamental and applied surface analysis.[2,5] However, it is a

characteristic of most surface analysis techniques that they are carried out based on the spatially averaged signals on various area sizes. The surface heterogeneities on metal surfaces including oxidation, defects, and grain structures result in surface complexities.[6-8] For example, crystal domains of various sizes naturally form on most metallic material surfaces. It would induce heterogeneous corrosion process due to the variation of local physical and chemical properties.[9-12] Furthermore, most catalysis processes on metal surfaces such as CO adsorption and reaction with oxygen on the polycrystalline platinum surface are heterogeneous with various reaction rates on different sites.[13,14] Therefore, enormous local chemical information would be overlooked and an inaccurate interpretation of surface chemistry might happen if the signal are acquired from the entire surface instead of analyzing the individual regions of interest on the surface.[15] A full investigation of the surface phenomena of metal surfaces demands a microscopic study about the surface heterogeneity, as well as local chemical processes.

Such demands to map variation in the chemistry across the metal surface with spatial resolution arises in a wide variety of microscopy technologies. Over the years those techniques have been carried out to probe different aspects of the surface properties and found wide applications in basic surface science and applied industry.[16-19] For instance, probe scanning microscopies including scanning tunneling microscopy (STM) and atomic force microscopy (AFM), are powerful and popular techniques for probing the metal surface structure and morphology. The impressive images with excellent spatial resolution to single atomic level have significantly advanced the surface chemistry studies. However the chemical information provided by these techniques is not straight-forward and lacking. Additionally, these techniques lack the capability of elucidating the molecular

conformation information on most metal surface. Photoemission electron microscopy (PEEM) is capable of measuring electron binding energies to determine the component atoms with surface sensitivity, as well as micrometer spatial resolution. However, those techniques, which are based on the scattering, absorption, and reflection of photons, electrons, neutrons, atoms, and ions, could only be applied in ultra-high vacuum (UHV) systems. This constraint imposes severe restrictions since the surface processes which are able to be studied are greatly reduced such as the liquid interface. Besides that, only a few complete surface reaction mechanisms had been derived based on systems studied under UHV conditions (pressure gap).[20] Microscopic studies of surfaces under high pressure, which are common in practical applications of metals, had been mostly left behind. In principle, modeling complex chemical processes on the heterogeneous metal surfaces requires analytical techniques, which have to be very sensitive to detect molecules at a level below $10^{15}/cm^2$, to yield the molecular level information, and, at the same time, to be applicable under non-vacuum conditions. Fortunately, the SFG imaging technique overcomes these difficulties. As a surface-specific spectroscopy technique applied in the imaging mode, SFG imaging could yield a molecular-level understanding of the processes of adsorption and reactions at metal surfaces with high spatial resolution. The ability of SFG imaging to study the metal-adsorbate interaction has been theoretically and experimentally demonstrated in this thesis.

1.2. Sum frequency generation imaging

1.2.1 Sum frequency generation

Since the past century, non-linear optical phenomena including Pockels and Faraday effect have been observed. Soon after the initial invention of pulsed lasers at the end of 1950s, experimental observation and theoretical understanding of more nonlinear optical phenomena including second harmonic generation (SHG) and SFG have been realized.[21-25] The SFG signal generated from a monolayer of coumarin dye on fused silica was attained by the group of Shen the first time. Soon SFG has been rapidly developed into a powerful surface technique for versatile studies of chemical bonding, identity, structure, conformation and molecular reaction on almost all kinds of surfaces and interfaces in these three decades.[3,26-33] In a typical SFG setup, two incident beams, a visible beam and a tunable infrared beam, interacted simultaneously with the atom or molecule to instantaneously produce a new photon with the sum of the two frequencies. There will be a resonant enhancement of the SFG signal when the infrared frequency matches the frequency of a vibrational mode of the molecules at the interface. This results in a peak or a dip from scanning the infrared frequency, therefore yielding a vibrational spectrum called the SFG spectrum. Compared with other vibrational spectroscopy methods, the unique advantage of SFG lies in its intrinsic surface sensitivity. Under the electric dipole approximation, symmetry requirements for second-order optical processes only allow the SFG signal to be generated from the interface between two isotropic medium and consequently make SFG surface-specific.[34]

1.2.2 Introduction of SFG imaging

SFG vibrational spectroscopy is a nonlinear optical technique that probes the nonlinear response of materials, as described by the second-order susceptibility $\chi^{(2)}$. The

combination of chemical sensitivity and surface selectivity has rendered SFG a popular tool for studying molecular properties at interfaces. However, the spatially averaged SFG signal is not sensitive to surface heterogeneities in samples that manifest themselves on the microscopic scale. To resolve such issue, SFG adopted in a microscopic/imaging mode emerged by Florsheimer et al in 1999 at the first time and was referred to as SFG imaging.[35] In their SFG imaging setup, the SFG signal was collected by an intensified charge-coupled device (CCD) camera from a fused silica prism with a Langmuir-Blodgett (LB) monolayer deposited on the surface. The collection direction of the SFG signal was set at an oblique angle. It required an optical design to avoid the distortion of images and to enable the whole image in focus over the entire field of view. The near-field configuration of SFG imaging was developed by several groups and undistorted SFG images were obtained with spatial resolution as high as 190 nm.[36,37] However, such near-field SFG imaging setups were difficult to be widely used due to extremely weak SFG signals. Only materials with huge nonlinear susceptibilities such as GaAs were able to generate enough signals to achieve a good SFG image in a reasonable time frame. Later, a 1:1 telescope and diffraction grating were employed to solve the image distortion issue from wide-field SFG imaging and was rapidly applied by Kuhnke et. al[38] and Baldelli et. al.[15,39-45] This type of SFG microscope has demonstrated its power in the image quality and reliablity for surface chemistry studies with a more widespread application to more complex systems in various fields of technological importance such as self-assembled monolayers (SAMs) and gas (i.e., CO, methanol) adsorption on metal surfaces.[1,39,40,42,46,47]

To date, a number of new SFG imaging setups based on either a point scanning or wide-field illumination configuration have been reported. For example, Conboy *et al.*

described an SFG imaging setup, which utilizes a single focusing lens in conjunction with a confocal stop that was capable of resolving both vertical and horizontal line-widths of varying sizes in the micrometer scale.[48] Ge and her coworkers reported a novel confocal SFG microscope with imaging studies on collagen structures.[49] In their SFG imaging setup, the incident beam was focused with a beam size approximately equal to the diffraction limit. The SFG signal was collected by a PMT in scanning mode to reconstruct the SFG image with sub-micron spatial resolution. In addition, Baldelli *et al.* developed a unique SFG imaging setup to collect the SFG signal with the combination of a digital mirror device (DMD) with a PMT instead of CCD. The SFG image was then reconstructed through a comprehensive sensing method.[50] Most recently, Mason *et al.* built a microscope through combining sample scanning SFG imaging with confocal fluorescence microscope. It allowed the surfaces to be probed both spectrally and visually with contrast generation derived from two distinct techniques.[51]

Among the various kinds of SFG imaging configuration, the wide-field reflection SFG imaging setup is the most attractive since such microscope design is easy to build and operate.[41] Such imaging configuration not only enables fast image acquirement with high spatial resolution, but also allows the independent characterization of alternative vibrational modes with different polarization resolved conditions, which is especially useful for relating the properties of chemical group vibrations to molecular orientations at interfaces.

1.2.3 Comparison with other spectroscopic microscopes

The most-striking advantage of SFG over other microscopic techniques is the intrinsically high interface sensitivity due to the nonlinear interaction of light with matter. Other vibrational microscopy techniques including Fourier transform infrared microscopy (FTIR microscopy)[52,53] and Raman microscopy[54,55] are also able to probe the surface at molecular levels with varied spatial resolution; however, these techniques cannot distinguish the signal from the bulk contribution considering the bulk exhibits a vibrational features in the same spectral range as the surface species. For practical consideration, a key advantage of SFG imaging is the up-conversion of the IR beam into the visible/near-ultraviolet (UV) range. This enabled the use of a highly sensitive detection device such as photomultiplier tube (PMT) or a CCD. Moreover, it was well known that in IR and Raman studies the congestion of various vibrational modes in the C-H stretching region made spectral assignments notoriously complex even with the simplest molecules. As an intrinsically coherent spectroscopy, it was feasible to use the polarization analysis and selection rules to discern complex vibrational spectra by SFG spectroscopy. In addition, as a coherent optical process, another advantage of SFG imaging lies in its capabilities to analyze the orientation of molecules on surfaces compared with the linear vibrational spectroscopy technique such as an IR microscope. Detecting different polarization combination of the IR, visible, and SFG beam enables the determination of orientation information of molecular groups at the interface under investigation. Despite all of these advantages for interface studies, SFG imaging is limited for becoming a common analytical instrument for general practice because of its weak signal levels. An intense pulsed laser is always required to generate enough SFG signals. The time spent on maintenance and optimization of the laser systems, together with the high costs, restricts the widespread

applications of SFG imaging. Nevertheless, tremendous progress in instrument implementations have dealt with these technique difficulties and have allowed SFG imaging to be a much more useful technique for future surface science research.

1.2.4. The SFG research on the metal surface

Molecular level understanding of the molecular behavior on metal surfaces is crucial for addressing important problems such as catalysis in surface chemistry. SFG, as well as SHG, has been proven to be effective for probing chemical bonding, chemical structure, and molecular reactions at the metal surface. SHG has been applied to investigate the surface electronic properties of metals.[56,57] In the past three decades, SFG was extensively applied for the research of various metal surface systems, such as surface catalysis and electrochemical interface.[58,59] SFG's ability to study the metal-adsorbate interaction and the metal surface was theoretically described.[60] Remarkably, most metals including copper and silver give rise to a large non-resonant background signal which arises from the optical non-linearity of the metal surface itself.[61] This background provides an internal reference for phase measurements and greatly optimizes the SFG signal. However, it also complicates the interpretation of the SFG spectrum with the modification of the spectral profile through the interference between non-resonant and resonant components. Consequently, it needs to be taken into account when interpreting the spectrum. Another feature of SFG studies on metals is that the component of the local electric field normal to the surface is enhanced; however, the parallel component becomes smaller because of the boundary conditions of the electric field on metal surfaces.[62,63] This is particularly true for the light beam in the IR frequency range.[64] The P-polarized light has

an electric field parallel to the plane of incidence, while the S-polarized light is perpendicular to the plane of incidence. Consequently, these two elements of nonlinear susceptibility which are the $\chi_{ssp}^{(2)}$ and $\chi_{ppp}^{(2)}$ dominate the SFG signal on the metal surface. The last feature is that all metals are opaque to the visible light. Thus, the metal surface usually has a lower damage threshold compared with the dielectric surfaces.[58,62]

The theory of SHG generated in the metal bulk medium has been well developed during recent years.[22,65,66] However, the interpretation of the SFG process on metal surfaces is still unclear. It is well known that the surface nonlinear susceptibility of a metal strongly depends on the surface electronic distribution of the metal.[67,68] Traditionally, SFG signal generated from the metal surface was explained by employing the jellium mode, which is derived from the non-resonant polarizability of nearly free electrons.[66,69-71] In this model, only this element of nonlinear susceptibility which is χ_{zzz} would be affected by the spatial dispersion of nearly free electrons, where z denotes the direction normal to the surface plane. Such explanation provides a simple and clear physical model. However, this model could not explain the azimuthal anisotropy of SFG signal on the metal surface. In metals, if the electrons are totally free, the nonlinear polarizability should be isotropic.[72,73] If a suitable amount of the nonlinear polarizability is due to interband transitions, some anisotropy of the second order polarizability might be expected from the metal surface.[56] Previous works also demonstrated that the nonlinear response of metals has two parts: the first part originated from a bulk current that extends roughly one optical skin depth into the metal, and the another part originated from the surface current, which is presented in a layer of only a few angstroms.[70,74,75]

The remarkable nonlinear background of metal surfaces originated from the metal surface electron is unique compared with dielectric surfaces. The convolution of the resonant and non-resonant susceptibilities leads to the wide variety of line shapes observed in the SFG spectra, which causes the interpretation of SFG spectrum on metal surfaces difficult and ambiguous. However, the local spatial correlation of the non-resonant response with the conformation and orientation of adsorbed molecules is very useful in understanding how the local metal features influence the property of top-layer molecules. This makes it of utmost importance to deduce the non-resonant response on the metal surface as completely as possible by systematic studies. Such works have been introduced in the fifth chapter, which focuses on a systematic investigation of SAMs on a micro polycrystalline copper surface with the goal to further develop SFG as a tool for metal surface analysis.

1.3. Corrosion studies about the grain boundaries and grain on the copper surface covered with SAMs monolayer

SAMs of alkanethiol on metal surfaces has been extensively studied due to their simple chemical adsorption, densely packed structure, excellent stability, and wide application including the formation of a hydrophobic barrier to protect the metal surface from corrosion.[76-80] It was further concluded that the SAMs with longer hydrocarbon chain length have better inhibition ability for the metal surface.[81] Currently, one popular technique for monitoring the corrosion behavior of metal surfaces covered with SAMs monolayer is SFG spectroscopy, which can provide detailed information and understanding of the molecular composition, conformation, and interaction with the

underneath metal surface at a molecular level.[82] In the work done by Fonder et al., SFG studies have been applied to monitor the protection efficiency of the ordered monolayer of alkanethiols on a metal surface for corrosion.[83] Recently, Hosseinpour et. al. investigated the oxidation of ODT-covered copper in dry air by SFG and observed the formation of a thin layer of copper (I) oxide beneath the ODT monolayer based on the phase change of the SFG spectra.[77] However, the local chemical information can be overlooked since all these SFG studies were based on an average spectral analysis of the surface without detecting local heterogeneous chemical information. In recent studies, the SFG imaging technique have been developed and demonstrated good capability for studying monolayers on a heterogeneous metal surface with high spatial resolution.[39,41,45] The localized corrosion processes including Cu_2O formation occurring on copper surfaces in an oxygenated environment have been firstly studied by Santos et. al.[39]

Various-sized crystal domains with different crystallographic orientations naturally forms on most metallic material surfaces, including copper.[9,10] The local physical and chemical properties of adsorbed monolayers, associated with surface functionalities such as wettability, corrosion, and other technological applications would be strongly affected by the local surface atom arrangement.[11,12] Generally, the atmospheric corrosion process of metals with SAMs is complicated due to various heterogeneous chemical processes, which originates from crystal grains with different crystallographic orientations that exist on most polycrystalline metallic material surfaces.[9,10] Recent studies indicated that the localized corrosion on a copper surface could be induced by the heterogeneity across microscopic crystal grains and grain boundaries (GBs).[84-86] Additionally, the features, including surface current difference across grains,[6,7] extensive mis-orientation between

grains,[8] and grain sizes[87,88] contribute to heterogeneous corrosion occurring on the surfaces. Thus, the comprehensive understanding about the role of crystallographic orientations on local metallic corrosion processes and inhibition is of critical important due to its significance to the modern world.[89]

1.4. Overview of the thesis

In this past decade, SFG imaging technique has been widespread used to study various surface systems and proved to be a useful tool to study the heterogeneous surface chemistry. The focus of this study is to present a detailed description of the SFG imaging technique and its advantages in studying the molecular behavior on heterogeneous metal surfaces. The overall goal is to advance this technique as a powerful analytical research technique for qualitatively and quantitatively measuring the surface chemistry in complex metal surfaces associated with catalysis, corrosion, and biological systems. The metal surface systems studied in this thesis consist of two main parts, including gas adsorption on a metal surface and monolayers on a metal surface.

In the next chapter, a detailed theory of SFG vibrational spectroscopy is introduced. Besides that, the experimental setup of SFG imaging including the picosecond laser source, OPG/OPA system, the SFG microscope setup is described. The ultra-high vacuum system and hydrogen annealing oven, which are used to prepare a clean metal sample, is described.

In the third chapter, the adsorption of methanol at a near-atmospheric pressure on the polycrystalline copper surface has been studied using a combination of SFG and temperature programmed desorption. The role of oxygen atoms on the copper surfaces in

the adsorption of methanol is investigate by the SFG imaging. Based on the statistical analysis of SFG images, the heterogeneities of the methoxy monolayer with/without oxygen are compared.

The following chapter is about an octadecanethiol (ODT) self-assembled monolayer on microcrystalline copper investigated by SFG imaging. The crystal grain and grain boundaries of the copper surface are mapped in the SFG image based on the strong brightness contrast of the SFG signal across the boundary. Local SFG spectra reveal significant differences with each other, as well as with the average SFG spectra, indicating the heterogeneity of the copper surface resulting from copper grains with distinct crystallographic facets and orientations. In addition, the statistical orientational analysis of the amplitude ratio of CH_3-sym/CH_3-asym and the corresponding contour maps imply that the orientation of ODT molecules is affected by the underlying copper.

The fifth chapter addresses that the metal surface usually has a strong non-linear background which results from the surface electronic properties of the metal. The local metal property variation introduces the metal surface heterogeneity, which may cause the molecular behavior in a local area to vary from each other. SFG imaging is very powerful in building the local spatial correlation of the optical non-resonant response of the metal surface to conformation and orientation of the adsorbed molecule. The relationship between the local chemistry of interfacial molecule with their local special chemical environment may be deduced. However, in order to deduce the structural information, it is critical to understand the behavior of the nonlinear optical fields at different surfaces. The systematic formulation of the optical field and transformation of the nonlinear

susceptibility to hyper-polarizability are discussed with SFG intensity simulation on dielectric, semiconductor, and metal surfaces.

In the sixth chapter, the CO adsorption on a polycrystalline platinum surface investigated by SFG imaging is presented. SFG spectra identify the linearly bonded of CO adsorbed on the polycrystalline platinum surface based on the stretching vibration mode of CO. Crystal domain structures on the polycrystalline platinum surface are demonstrated on the SFG image. In order to deduce the heterogeneity on the polycrystalline platinum surface, the image statistical analysis based on CO stretching frequency is performed. The resonant frequency of CO stretching vibration varies on the different crystal domain areas.

In the last chapter, a summary of the work is given, together with an outlook and suggestions for future work.

1.5. References

(1) Langmuir, I. *T. Faraday Soc.* **1922**, *17*, 621.

(2) Vickerman, J. C.; Gilmore, I. S. *Surface analysis: the principal techniques*; Wiley Online Library, 2009; Vol. 2.

(3) Lu, R.; Gan, W.; Wu, B. H.; Chen, H.; Wang, H. F. *J. Phys. Chem. B* **2004**, *108*, 7297.

(4) Weatherbee, G. D.; Bartholomew, C. H. *J. Catal.* **1982**, *77*, 460.

(5) Woodruff, D. P.; Delchar, T. A. *Modern techniques of surface science*; Cambridge university press, 1994.

(6) Schreiber, A.; Schultze, J. W.; Lohrengel, M. M.; Karman, F.; Kalman, E. *Electrochim. Acta* **2006**, *51*, 2625.

(7) Lill, K. A.; Hassel, A. W.; Frommeyer, G.; Stratmann, M. *Electrochim. Acta* **2005**, *51*, 978.

(8) Miyamoto, H.; Yoshimura, K.; Mimaki, T.; Yamashita, M. *Corros. Sci.* **2002**, *44*, 1835.

(9) Martinez-Lombardia, E.; Maurice, V.; Lapeire, L.; De Graeve, I.; Verbeken, K.; Kestens, L.; Marcus, P.; Terryn, H. *J. Phys. Chem. C* **2014**, *118*, 25421.

(10) Lapeire, L.; Martinez Lombardia, E.; Verbeken, K.; De Graeve, I.; Kestens, L. A. I.; Terryn, H. *Corros. Sci.* **2013**, *67*, 179.

(11) Nihonyanagi, S.; Miyamoto, D.; Idojiri, S.; Uosaki, K. *J. Am. Chem. Soc.* **2004**, *126*, 7034.

(12) Aaronson, B. D.; Chen, C. H.; Li, H.; Koper, M. T.; Lai, S. C.; Unwin, P. R. *J. Am. Chem. Soc.* **2013**, *135*, 3873.

(13) Ertl, G. *Science* **1991**, *254*, 1750.

(14) Lauterbach, J.; Haas, G.; Rotermund, H.; Ertl, G. *Surf. Sci.* **1993**, *294*, 116.

(15) Santos, G.; Baldelli, S. *J. Phys. Chem. C* **2012**, *116*, 25874.

(16) Claypool, C. L.; Faglioni, F.; Goddard, W. A.; Gray, H. B.; Lewis, N. S.; Marcus, R. *J. Phys. Chem. B* **1997**, *101*, 5978.

(17) Claypool, C. L.; Faglioni, F.; Matzger, A. J.; Goddard, W. A.; Lewis, N. S. *J. Phys. Chem. B* **1999**, *103*, 9690.

(18) Claypool, C. L.; Faglioni, F.; Goddard, W. A.; Lewis, N. S. *J. Phys. Chem. B* **1999**, *103*, 7077.

(19) Yu, H.; Webb, L. J.; Ries, R. S.; Solares, S. D.; Goddard, W. A.; Heath, J. R.; Lewis, N. S. *J. Phys. Chem. B* **2005**, *109*, 671.

(20) Härle, H.; Lehnert, A.; Metka, U.; Volpp, H. R.; Willms, L.; Wolfrum, *Chem. Phys. Lett.* **1998**, *293*, 26.

(21) Franken, P.; Hill, A.; Peters, C. E.; Weinreich, G. *Phys. Rev. Lett.* **1961**, *7*, 118.

(22) Bloembergen, N.; Pershan, P. *Phys. Rev.* **1962**, *128*, 606.

(23) Armstrong, J.; Bloembergen, N.; Ducuing, J.; Pershan, P. *Phys. Rev.* **1962**, *127*, 1918.

(24) Simon, H.; Mitchell, D.; Watson, J. *Phys. Rev. Lett.* **1974**, *33*, 1531.

(25) Bass, M.; Franken, P.; Hill, A.; Peters, C.; Weinreich, G. *Phys. Rev. Lett.* **1962**, *8*, 18.

(26) Zhu, X.; Suhr, H.; Shen, Y. *Phys. Rev. B* **1987**, *35*, 3047.

(27) Somorjai, G. A.; Rupprechter, G. *J. Phys. Chem. B* **1999**, *103*, 1623.

(28) Bain, C. D. *J. Chem. Soc. Faraday Trans.* **1995**, *91*, 1281.

(29) Tian, C. S.; Shen, Y. R. *Surf. Sci. Rep.* **2014**, *69*, 105.

(30) Buck, M.; Himmelhaus, M. *J. Vac. Sci. Technol.* **2001**, *19*, 2717.

(31) Richmond, G. *Chem. Rev.* **2002**, *102*, 2693.

(32) Chen, Z.; Shen, Y. R.; Somorjai, G. A. *Annu. Rev. Phys. Chem.* **2002**, *53*, 437.

(33) Shen, Y. R. *Nature* **1989**, *337*, 519.

(34) Shen, Y. R. Principles of nonlinear optics. Wiley: **1984**.

(35) Flörsheimer, M.; Brillert, C.; Fuchs, H. *Langmuir* **1999**, *15*, 5437.

(36) Shen, Y. R.; Swiatkiewicz, J.; Winiarz, J.; Markowicz, P.; Prasad, P. N. *Appl. Phys. Lett.* **2000**, *77*, 2946.

(37) Humbert, B.; Grausem, J.; Burneau, A.; Spajer, M.; Tadjeddine, A. *Appl. Phys. Lett.* **2001**, *78*, 135.

(38) Hoffmann, D.; Kuhnke, K.; Kern, K. *Rev. Sci. Instrum.* **2002**, *73*, 3221.

(39) Chastang, J. C. In *1983 International Techincal Conference/Europe*; International Society for Optics and Photonics: 1983, p 239.

(40) Cimatu, K.; Baldelli, S. *J. Phys. Chem. B* **2006**, *110*, 1807.

(41) Cimatu, K.; Baldelli, S. *J. Am. Chem. Soc.* **2008**, *130*, 8030.

(42) Cimatu, K.; Moore, H. J.; Barriet, D.; Chinwangso, P.; Lee, T. R.; Baldelli, S. *J. Phys. Chem. C* **2008**, *112*, 14529.

(43) Cimatu, K.; Moore, H. J.; Barriet, D.; Chinwangso, P.; Lee, T. R.; Baldelli, S. *J. Phys. Chem. C* **2008**, *112*, 14529.

(44) Cimatu, K.; Moore, H. J.; Lee, T. R.; Baldelli, S. *J. Phys. Chem. C* **2007**, *111*, 11751.

(45) Cimatu, K. A.; Baldelli, S. *J. Phys. Chem. C* **2009**, *113*, 16575.

(46) Santos, G. M.; Baldelli, S. *J. Phys. Chem. C* **2013**, *117*, 17591.

(47) Vogel, D.; Spiel, C.; Suchorski, Y.; Urich, A.; Schlögl, R.; Rupprechter, G. *Surf. Sci.* **2011**, *605*, 1999.

(48) Cimatu, K.; Baldelli, S. *J. Am. Chem. Soc.* **2008**, *130*, 8030.

(49) Fang, M.; Baldelli, S. *J. Phys. Chem. Lett.* **2015**, *6*, 1454.

(50) Smith, K. A.; Conboy, J. C. *Anal. Chem.* **2012**, *84*, 8122.

(51) Han, Y.; Raghunathan, V.; Feng, R. R.; Maekawa, H.; Chung, C. Y.; Feng, Y.; Potma, E. O.; Ge, N. H. *J. Phys. Chem. B* **2013**, *117*, 6149.

(52) Cai, X.; Hu, B.; Sun, T.; Kelly, K. F.; Baldelli, S. *J. Chem. Phys* **2011**, *135*, 194202.

(53) Allgeyer, E. S.; Sterling, S. M.; Gunewardene, M. S.; Hess, S. T.; Neivandt, D. J.; Mason, M. D. *Langmuir* **2015**, *31*, 987.

(54) Kazarian, S.; Chan, K. *BBA Biomembranes* **2006**, *1758*, 858.

(55) Sahlin, J. J.; Peppas, N. A. *J. Appl. Polym. Sci.* **1997**, *63*, 103.

(56) Ray, K.; McCreery, R. L. *Anal. Chem.* **1997**, *69*, 4680.

(57) Treado, P. J.; Govil, A.; Morris, M. D.; Sternitzke, K. D.; McCreery, R. L. *Appl. Spectrosc.* **1990**, *44*, 1270.

(58) Tom, H.; Aumiller, G. *Phys. Rev. B* **1986**, *33*, 8818.

(59) Hübner, W.; Bennemann, K.; Böhmer, K. *Phys. Rev. B* **1994**, *50*, 17597.

(60) Potterton, E.; Bain, C. *J. Electroanal. Chem.* **1996**, *409*, 109.

(61) Guyot-Sionnest, P.; Superfine, R.; Hunt, J.; Shen, Y. *Chem. Phys. Lett.* **1988**, *144*, 1.

(62) Mendoza, B. S.; Mochán, W. L.; Maytorena, J. A. *Phys. Rev. B* **1999**, *60*, 14334.

(63) Hirose, C.; Akamatsu, N.; Domen, K. *Appl. Spectrosc.* **1992**, *46*, 1051.

(64) Superfine, R.; Guyot-Sionnest, P.; Hunt, J.; Kao, C.; Shen, Y. *Surf. Sci.* **1988**, *200*, L445.

(65) Miragliotta, J.; Polizzotti, R.; Rabinowitz, P.; Cameron, S.; Hall, R. *Chem. Phys.* **1990**, *143*, 123.

(66) Tanaka, Y.; Lin, S.; Aono, M.; Suzuki, T. *Appl. Phys. B-Lasers O.* **1999**, *68*, 713.

(67) Jha, S. S. *Phys. Rev.* **1965**, *140*, A2020.

(68) Bloembergen, N.; Chang, R. K.; Jha, S.; Lee, C. *Phys. Rev.* **1968**, *174*, 813.

(69) Guyot-Sionnest, P.; Tadjeddine, A.; Liebsch, A. *Phys. Rev. Lett.* **1990**, *64*, 1678.

(70) Liebsch, A.; Schaich, W. *Phys. Rev. B* **1989**, *40*, 5401.

(71) Bloembergen, N.; Chang, R.; Jha, S.; Lee, C. *Phys. Rev.* **1969**, *178*, 1528.

(72) Rudnick, J.; Stern, E. A. *Phys. Rev. B* **1971**, *4*, 4274.

(73) Sipe, J.; So, V.; Fukui, M.; Stegeman, G. *Phys. Rev. B* **1980**, *21*, 4389.

(74) Guyot-Sionnest, P.; Hunt, J.; Shen, Y. *Phys. Rev. Lett.* **1987**, *59*, 1597.

(75) Petukhov, A. *Phys. Rev. B* **1995**, *52*, 16901.

(76) Richmond, G. L.; Robinson, J. M.; Shannon, V. L. *Prog. Surf. Sci.* **1988**, *28*, 1.

(77) Liebsch, A. *Surf. Sci.* **1994**, *307–309, Part B*, 1007.

(78) Hosseinpour, S.; Johnson, C. M.; Leygraf, C. *J. Electrochem. Soc.* **2013**, *160*, C270.

(79) Hosseinpour, S.; Hedberg, J.; Baldelli, S.; Leygraf, C.; Johnson, M. *J. Phys. Chem. C* **2011**, *115*, 23871.

(80) Laibinis, P. E.; Whitesides, G. M. *J. Am. Chem. Soc.* **1992**, *114*, 9022.

(81) Nuzzo, R. G.; Allara, D. L. *J. Am. Chem. Soc.* **1983**, *105*, 4481.

(82) Laibinis, P. E.; Whitesides, G. M.; Allara, D. L.; Tao, Y. T.; Parikh, A. N.; Nuzzo, R. G. *J. Am. Chem. Soc.* **1991**, *113*, 7152.

(83) Li, G.; Ma, H.; Jiao, Y.; Chen, S. *J. Serb. Chem. Soc.* **2004**, *69*, 791.

(84) Wang, H. F.; Velarde, L.; Gan, W.; Fu, L. *Annu. Rev. Phys. Chem.* **2015**, *66*, 189.

(85) Fonder, G.; Cecchet, F.; Peremans, A.; Thiry, P. A.; Delhalle, J.; Mekhalif, Z. *Surf. Sci.* **2009**, *603*, 2276.

(86) Park, C. J.; Lohrengel, M. M.; Hamelmann, T.; Pilaski, M.; Kwon, H. S. *Electrochim. Acta* **2002**, *47*, 3395.

(87) Martinez-Lombardia, E.; Lapeire, L.; Maurice, V.; De Graeve, I.; Verbeken, K.; Klein, L. H.; Kestens, L. A. I.; Marcus, P.; Terryn, H. *Electrochem. Commun.* **2014**, *41*, 1.

(88) Martinez-Lombardia, E.; Gonzalez-Garcia, Y.; Lapeire, L.; De Graeve, I.; Verbeken, K.; Kestens, L.; Mol, J. M. C.; Terryn, H. *Electrochim. Acta* **2014**, *116*, 89.

(89) Luo, W.; Xu, Y.; Wang, Q.; Shi, P.; Yan, M. *Corros. Sci.* **2010**, *52*, 3509.

(90) Ralston, K. D.; Birbilis, N. *Corrosion* **2010**, *66*.

(91) Schweitzer, P. A. *Fundamentals of corrosion: mechanisms, causes, and preventative methods*; CRC Press, 2009.

CHAPTER 2. Theory and Experimentation

2.1. Sum frequency generation (SFG) theory

2.1.1 SFG optical process

Sum frequency generation vibrational spectroscopy (SFG-VS) is a second-order nonlinear optical technique in which a tunable IR beam is spatially and temporally overlapped with a visible beam on the surface to generate a SFG output beam.[1] The new generated SFG beam is at the sum frequency of the two incident photons through simultaneous interaction with a nonlinear optical medium or interface. When the IR light comes into resonance with a surface vibrational mode, the intensity of SFG beam would change dramatically. By tuning the IR beam frequency, a plot of IR wavelength vs SFG intensity can be yielded and interpreted as the vibrational spectrum to probe the vibrational spectra of the molecular surface and to provide chemically specific information.[2-9]

To obtain an accurate interpretation of SFG spectrum and capture its intrinsic information about molecular addresses the importance of a comprehensive understanding of the mechanism about SFG. SFG was a second-order nonlinear response to the simultaneous interacting visible and IR electric field. When an external electric field was applied, the electron distribution in the medium oscillated harmonically in response to the applied electric field with an induced dipole generated. Most of such optical response could be perfectly explained by linear optics, that was, the induced dipole responded linear to the applied electric field. However, when the intensity of the applied electric field is extremely high and comparable to the intramolecular field felt by an electron, the linear polarization

of matter is no longer a sufficient approximation. In such case, higher order terms has to be taken into account and included in the expression of total dipole moment $\vec{\mu}$, which then is described by a series of expansion

$$\vec{\mu} = \overrightarrow{\mu^0} + \alpha\vec{E} + \beta : \vec{E}\vec{E} + \gamma \vdots \vec{E}\vec{E}\vec{E} + \cdots \qquad \textbf{Equation 2-1}$$

Here, the $\overrightarrow{\mu^0}$ is the static dipole of the material resulted from the localized electron distribution around an atom or a functional group with higher or lower electronegativity compared with surrounding environment. α is the linear polarizability which describes the polarization induced by the external applied electric field. β is the first order hyper polarizability, and γ is second order hyper polarizability, respectively. The relationship between macroscopic polarizability $\vec{P}$ with external electric field $\vec{E}$ is described by

$$\vec{P} = \chi^{(1)} \cdot \vec{E} + \chi^{(2)} : \vec{E}\vec{E} + \chi^{(3)} \vdots \vec{E}\vec{E}\vec{E} + \cdots \qquad \textbf{Equation 2-2}$$

Here, the coefficients $\chi^{(2)}$ is the n-th order susceptibilities of the medium. In general, the presence of such term could be regarded as an n-th order nonlinearity. The nonlinear optical process originated from $\chi^{(2)}$ is known as second-order optic process including SFG and SHG. If we assumed that external electric field was made up of two electric fields at different frequencies, the electric filed could be given as $\vec{E}_{0,1}\cos(\omega_1 t)$ and $\vec{E}_{0,2}\cos(\omega_2 t)$. Then the second order polarizability, $\vec{P}^{(2)}$ in a bulk medium or monolayer could be represented by:

$$\vec{P}^{(2)} = \chi^{(2)} : \vec{E}_{0,1}\cos(\omega_1 t)\vec{E}_{0,2}\cos(\omega_2 t)$$
$$= \frac{1}{2}\chi^{(2)} : \vec{E}_{0,1}\vec{E}_{0,2}\left\{\cos\left[(\omega_1+\omega_2)t\right] + \cos\left[(\omega_1-\omega_2)t\right]\right\}$$

Equation 2-3

The oscillation frequency of second order nonlinear polarizability is made up of the sum and difference frequencies of the two incident waves. It is the origins of SFG and difference frequency generation (DFG) process, respectively.[10,11] In the case of degeneracy, i.e., $\omega_1 = \omega_2$, SHG process occurs. Compared with linear optical processes such as Raleigh scattering, such nonlinear emission is coherent and directional. The direction of SFG output is determined by momentum conservation parallel to the interface.[12] The second-order nonlinear susceptibility, $\chi^{(2)}$, yields the induced second order polarization at $\omega_{SFG} = \omega_{vis} + \omega_{IR}$. The second-order nonlinear susceptibility, $\chi^{(2)}$, is the macroscopic orientation average of the molecular hyperpolarizability, $\beta^{(2)}$. Through the devolution of the relationship between $\chi^{(2)}$ and $\beta^{(2)}$, the orientation of a surface molecule could be determined.

2.1.2. Surface selectivity

Most of the surface analysis methods involve bombarding the surface with a form of a radiation such as electrons, photons, ions and neutrons, and then, collecting the resulting emitted radiation. Therefore, the surface sensitivity depends on the evanescent length of the radiation. Unlike most surface techniques, the unique surface sensitivity of SFG technique results from that the SFG process is forbidden in a bulk medium with inversion symmetry under the electric dipole approximation.[13]

In general, the electric quadrupole transition, and magnetic quadrupole transition could be neglected due to their relatively small cross section,[1,14,15] The electric dipole transition contributed dominantly to the SFG signal.[16] The surface selectivity originated from the intrinsic symmetry of second-order susceptibility, $\chi^{(2)}$, which is zero in centrosymmetric medium.[4,17,18] As a third-rank tensor, the second-order susceptibility, $\chi^{(2)}$, changed sign under inversion operation :

$$\chi^{(2)}(r) = -\chi^{(2)}(-r) \qquad \textbf{Equation 2-4}$$

For centrosymmetric medium, the tensor had such relationship:

$$-\chi^{(2)}(-r) = -\chi^{(2)}(r) \qquad \textbf{Equation 2-5}$$

Combining Equation 2- and Equation 2-, such relationship could be obtained:

$$\chi^{(2)}(r) = -\chi^{(2)}(r) \qquad \textbf{Equation 2-6}$$

Hence, $\chi^{(2)}$ is zero in bulk media. The SFG signal could only be generated from the interface between the two homogenous media where the inversion symmetry was broken. Therefore, comparing to the general linear spectroscopic techniques which rely on the penetration depth, SFG technique was powerful to study the molecular at the interface, especially on the liquid/gas and liquid/liquid interface.

2.1.3. Molecular level information from SFG vibrational spectroscopy

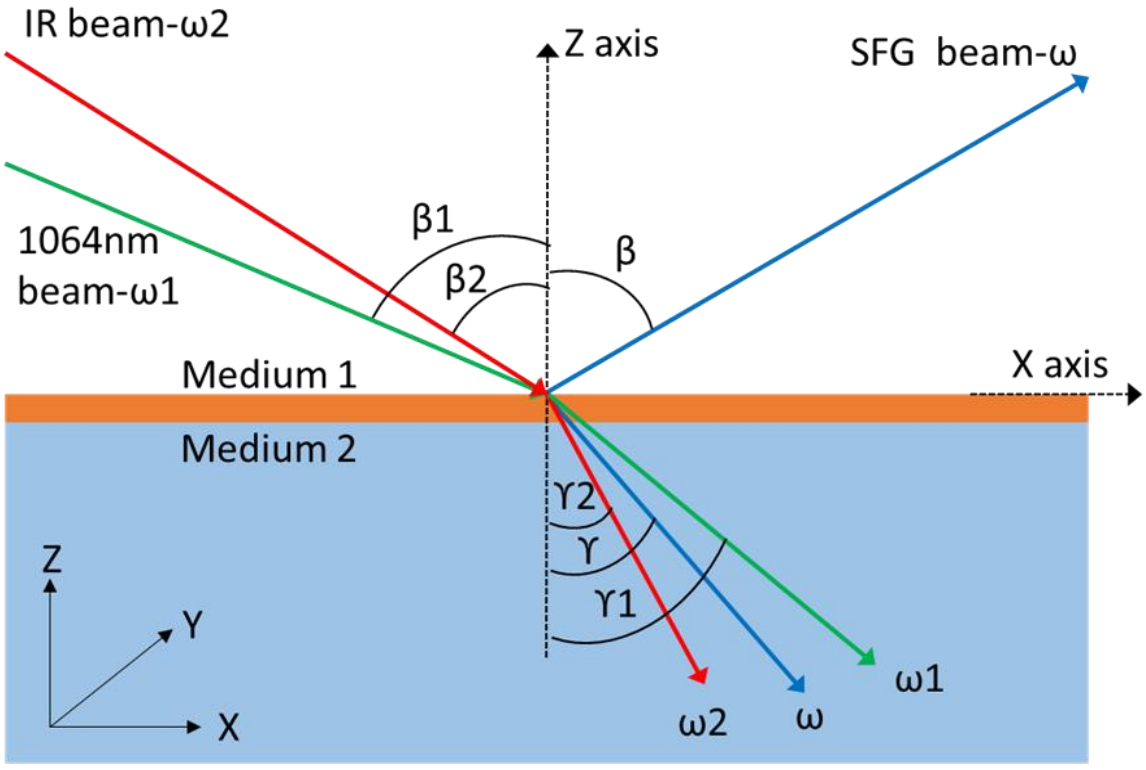

Figure 2-1. The scheme of the co-propagation SFG at interfaces. The incoming beams ($\omega_1$and ω_2) impinge on the surface and generate SFG beam (ω).

The Figure 2-1 presented the scheme of SFG set-up in the co-propagation configuration. Here ω, $\omega_1$and ω_2 represent the frequency of SFG beam, 1064 nm beam, and tunable IR laser beam, respectively; β, $\beta_1$and β_2 are the incident or the reflection angle of SFG beam, 1064 nm beam, and tunable IR beam, respectively. Normally, the right-handed xyz coordinate system is employed to define the configuration of SFG set-up. The light incident plane is defined as the xz plane in which the z axis coincides with the surface normal.

The SFG intensity measured with a spectrally narrow beam pulse is defined as follows in Equation 2-7:[19]

$$I_{SFG}(\omega) \propto \left|\chi_{eff}^{(2)}\right|^2 I(\omega_1) I(\omega_2) \qquad \textbf{Equation 2-7}$$

Where $\chi_{eff}^{(2)}$ is the second order nonlinear surface susceptibility and the I is the light intensity. SFG intensity is proportional to the intensity of the two incident laser beams, as well as the square of the absolute value of the effective susceptibility of interface, $\chi_{eff}^{(2)}$. The second order susceptibility contained all the molecular information. It needs to be noted that the emission direction of SFG signal should satisfy the conservation of momentum. This coherence pertains to the phase-matching conditions and is shown as:

$$n_{SF} k_{SF} \sin\beta = n_{VIS} k_{VIS} \sin\beta_1 + n_{IR} k_{IR} \sin\beta_2 \qquad \textbf{Equation 2-8}$$

Here n is the refractive index, and k is the wave vector for each beam; Θ is the corresponding angle from the surface normal. The second order susceptibility $\chi^{(2)}$ is a third rank tensor with 27 tensor elements, which could be represented as χ_{ijk}. (i, j, k) and denote one of the three axis of laboratory coordinate system (x, y, z). Based on the tensor symmetry,[17,18,20] the independent non-vanishing tensor elements for an achiral rotationally isotropic surface could be derived by symmetry operation as follows

$$\chi^{(2)}_{xxz} = \chi^{(2)}_{yyz}$$
$$\chi^{(2)}_{xzx} = \chi^{(2)}_{yzy}$$
$$\chi^{(2)}_{zxx} = \chi^{(2)}_{zyy}$$
$$\chi^{(2)}_{zzz}$$

Equation 2-9

2.1.4. Fresnel factors of SFG

When a light beam incidents on a monolayer at the interface of two media, the induced dipole in the monolayer and substrate generates a new electric field. Such electric filed is locally applied on each individual molecule within the molecular monolayer. Hence the total local electromagnetic field is different with the applied external electric field.[21-23] The Fresnel factors are derived for a three layer model and formulated to shown such local field effect as follows: [17,19,24]

$$L_{xx}(\Omega) = \frac{2n_1(\Omega)\cos\gamma}{n_1(\Omega)\cos\gamma + n_2(\Omega)\cos\beta}$$
$$L_{yy}(\Omega) = \frac{2n_1(\Omega)\cos\beta}{n_1(\Omega)\cos\beta + n_2(\Omega)\cos\gamma}$$
$$L_{zz}(\Omega) = \frac{2n_1(\Omega)\cos\beta}{n_1(\Omega)\cos\gamma + n_2(\Omega)\cos\beta}\left(\frac{n_1(\Omega)}{n'(\Omega)}\right)^2$$

Equation 2-10

Here Ω is the frequency of light; n_i is the refractive indices of light beam (Ω) in the i-th medium (n' is the refractive index of interface); β and γ are the incident angle and emission angle, respectively. The intrinsic anisotropy of the interface layer causes the anisotropy of the local field factors in the interface layer.[25] SFG spectrum is sensitive to the interfacial optical and electric properties, which make the SFG interpretation more

difficult but important. Consequently, SFG could be used to study such unique dielectric properties of the interfacial layer resulted from the surface anisotropy.

2.1.5. Overall expression of SFG

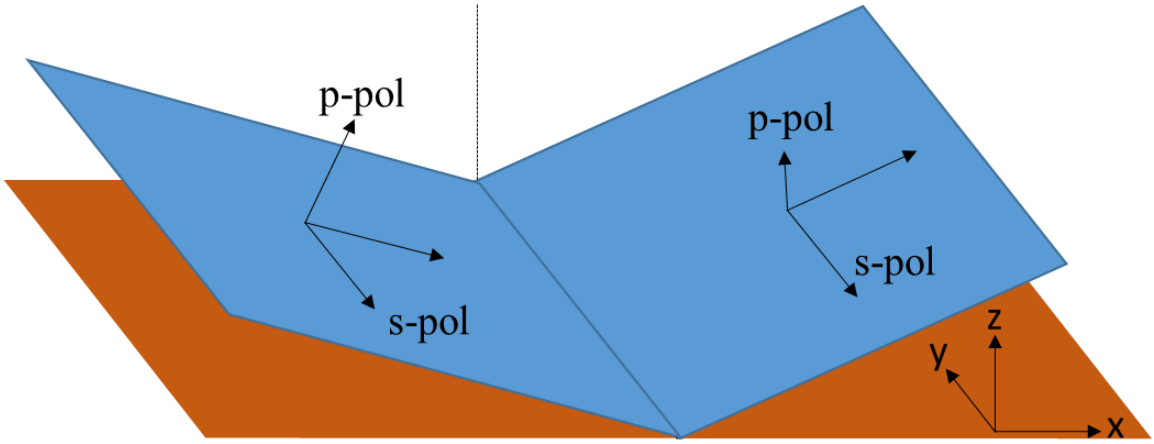

Figure 2-2. S-polarization and P-polarization of incident and reflected lights at the surface in laboratory coordinate system, respectively.

As shown in Figure 2-2, the laser beam could be expressed as a combination of two linear polarizations, *S* and *P*. The *S*- and *P*-polarized lights have the electric field direction perpendicular and parallel to the plane of incidence, respectively. This assignment help to determine each macroscopic susceptibility tensor elements separately according to the polarization combination of three optical fields. *S*-polarized light contains electric component in y direction; p-polarized light contains two electric components which are in x and z directions, respectively. Depending on the experimental polarization and geometry, there are an infinite number of combinations of experimental configuration which includes SSP, SPS, PSS, and PPP in the SFG measurement.[19,26] Since most SFG experiments are performed with a co-propagation geometry in the case that the visible and IR beams impinge in the same quadrant of the xz plane as described in Figure 2-1, the effective

susceptibilities $\chi_{eff}^{(2)}$ for such four polarization combination related to each individual susceptibility element as shown in the following:

$$\begin{aligned}
\chi_{eff,ssp}^{(2)} &= L_{yy}(\omega)L_{yy}(\omega_1)L_{zz}(\omega_2)\sin\beta_2\chi_{yyz}^{(2)} \\
\chi_{eff,sps}^{(2)} &= L_{yy}(\omega)L_{zz}(\omega_1)L_{yy}(\omega_2)\sin\beta_1\chi_{yzy}^{(2)} \\
\chi_{eff,pss}^{(2)} &= L_{zz}(\omega)L_{yy}(\omega_1)L_{yy}(\omega_2)\sin\beta\chi_{zyy}^{(2)} \\
\chi_{eff,ppp}^{(2)} &= -L_{xx}(\omega)L_{xx}(\omega_1)L_{zz}(\omega_2)\cos\beta\cos\beta_1\sin\beta_2\chi_{xxz}^{(2)} \\
&\quad - L_{xx}(\omega)L_{zz}(\omega_1)L_{xx}(\omega_2)\cos\beta\sin\beta_1\cos\beta_2\chi_{xzx}^{(2)} \\
&\quad + L_{zz}(\omega)L_{xx}(\omega_1)L_{xx}(\omega_2)\sin\beta\cos\beta_1\cos\beta_2\chi_{zxx}^{(2)} \\
&\quad + L_{zz}(\omega)L_{zz}(\omega_1)L_{zz}(\omega_2)\cos\beta\cos\beta_1\cos\beta_2\chi_{zzz}^{(2)}
\end{aligned} \qquad \textbf{Equation 2- 11}$$

The second-order susceptibility tensor $\chi_{eff}^{(2)}$, described as the sum of a non-resonant part $\chi_{\mathrm{NR}}^{(2)}$ and resonant part $\chi_{\mathrm{R}}^{(2)}$, correlated the induced second-order polarization response to the incident light intensity, as shown in Equation 2-12.

$$\chi_{eff}^{(2)} = \chi_{\mathrm{R}}{}^{(2)} + \chi_{\mathrm{NR}}{}^{(2)} = \sum_q \frac{A_q}{\omega_q - \omega_{IR} - i\Gamma_q} + A_{NR}e^{i\phi} \qquad \textbf{Equation 2-12}$$

Here N, A_q, ω, ω_q and Γq were surface molecular density, amplitude, frequency of the IR beam, resonant frequency, and damping constant of the q-th vibrational mode, respectively. This equation was also the basis equation for nonlinear model fitting of SFG spectra used for orientation analysis and mapping results.

2.1.6. The phase of SFG measurements

Usually the effective susceptibility $\boldsymbol{\chi}_{eff}^{(2)}$ is composed of two parts, which were the resonant contribution and non-resonant contribution. $\chi_{\mathrm{NR}}^{(2)}$ is contributed from the non-resonant contribution typically attributed to electronic excitation of substrate and the adsorbate. $\chi_{\mathrm{R}}^{(2)}$ denotes the resonant contribution related with a vibrational modes of the adsorbate molecular layer. In general, for dielectric materials including liquid and polymer, the non-resonant susceptibility is typically so small to be negligible compared with resonant susceptibility intensity. However, the metal or semiconductor surface usually contributes a large non-resonant background in same order as the magnitude from the resonant contribution due to the nearly free electrons in the surface region.[27,28] SFG signal contains terms which are the product of the non-resonant and resonant susceptibilities. That term gives rise to interference effects leading to the variety of complex spectral line shapes observed in SFG spectra.[29] When the frequency of an incident infrared beam (ω_{IR}) is resonant with a vibrational mode of adsorbed molecule, q, the $\chi_{\mathrm{R}}^{(2)}$ is dramatically changed, as well as the SFG intensity. Therefore the SFG spectrum provides similar information as could be obtained from conventional IR vibrational spectrum.

2.1.7. Orientation analysis

Besides providing the vibrational fingerprint of a surface species, SFG allows one to determine the orientation of molecular. That requires to relate the macroscopic susceptibility $\chi_{\mathrm{R}}^{(2)}$ which is experimentally accessible to the molecular hyper-polarizability $\beta_{i'j'k'}^{(2)}$. That involves an Euler transformation of $\beta_{i'j'k'}^{(2)}$ from the molecular frame coordinate

system (abc) to the surface coordinate system (ijk). The scheme is based on the ensemble average over on all possible molecular orientations as shown in Equation 2-13:[19]

$$\chi_{ijk}^{(2)} = N_s \sum_{i'j'k'} \left\langle R_{ii'} R_{jj'} R_{kk'} \right\rangle \beta_{i'j'k'}^{(2)} \qquad \textbf{Equation 2-13}$$

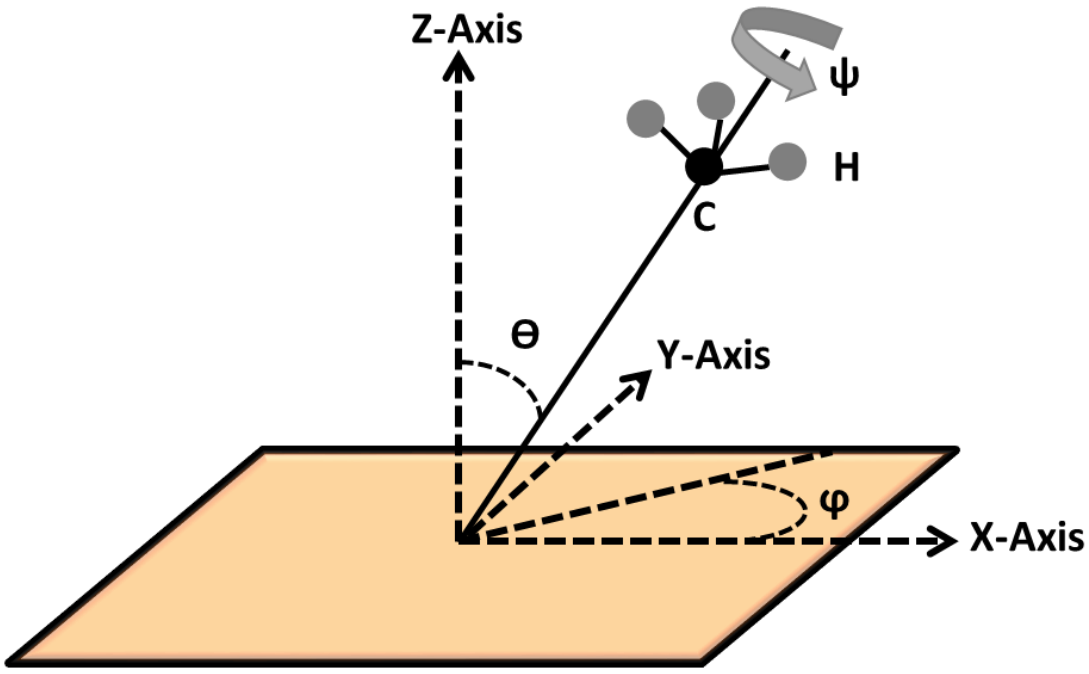

Figure 2-3. Definition of the tilt angle (θ), azimuth angle (φ), and rotation angle (ψ) of molecular adsorbed on the surface.

Here N_s is the surface density of molecular. The rotation ensemble average $\left\langle R_{ii'} R_{jj'} R_{kk'} \right\rangle$ in Equation 2-13 is defined with the matrix elements of the Euler transformation of the three rotational Euler angles to transform $\beta_{i'j'k'}^{(2)}$ in molecular frame coordinate system to $\chi_{ijk}^{(2)}$ in the laboratory coordinate system.[30,31] $R_{\lambda\lambda'}$ was an element of the Euler transformation matrix connecting the molecular coordinate system with the laboratory frame coordinate system. All the mathematical relationships between the 27

tensor elements of $\chi_{ijk}^{(2)}$ with the 27 tensor elements of $\beta_{i'j'k'}^{(2)}$ have been deduced by Hirose et al.[32] All the three angles including tilt angle (θ), azimuth angle (φ), and rotation angle (ψ) in Euler transformation were defined in Figure 2-3.

2.2. Optical instrumentation for SFG imaging experiment

Figure 2-4. Picture of EKSPLA PL2250 picosecond laser.

In this experiment, a picosecond laser is employed for SFG imaging experiment. A part of its 1064 nm beam output is used as a fundamental beam for SFG signal generation and another part of 1064 nm is used to pump an optical parametric generator/amplifier system (OPG/OPA), to generate a tunable mid-IR beam (2000-4000 cm^{-1}). The 1064 nm beam and tunable IR beam overlap on the surface at the same time to generate the SFG beam. The reason for employing the 1064 nm beam as pump beam instead of 532 nm beam is that the CCD camera has a much higher sensitivity in 532 nm region compared with 1064 nm region.[33] Employment of the 1064 nm beam is good to minimize the background noise of CCD camera from the 532 nm beam which was more common choice in previous SFG studies.[17,34,35] The SFG beam profile is magnified, refocused by a microscope system,

and collected by a CCD camera. Each of these optical components and associated optical process will be explained in detail in the following sections.

2.2.1. Picosecond PL2250 Laser

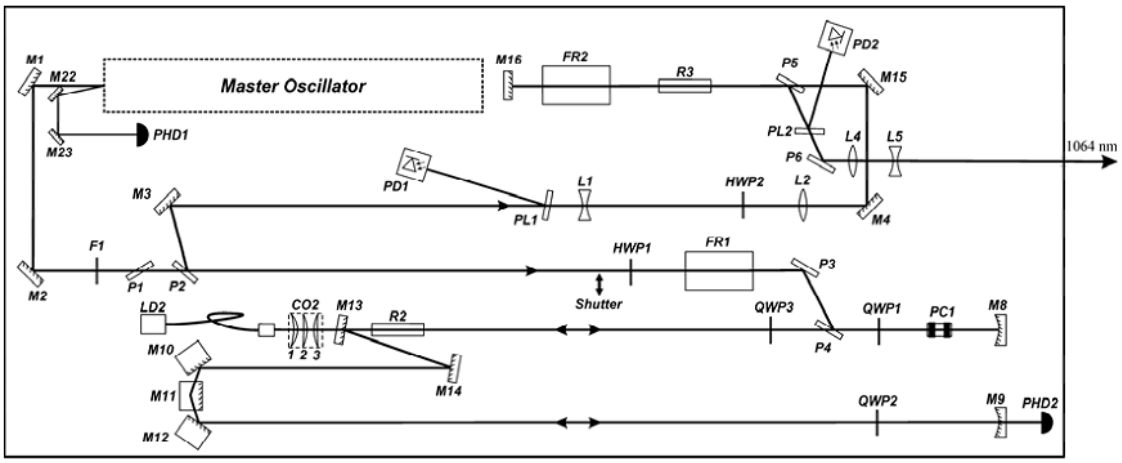

Figure 2-5. Optical layout of laser head of EKSPLA picosecond laser. Note: this figure is obtained from EKSPLA.

The pulsed laser is the most critical component to SFG experiment for its single wavelength and high peak power density. An mode-locked Q-switched Nd:YAG picosecond-pulsed laser (Ekspla, PL 2250) with a fundamental output of 1064nm, generating pulses of 20-30 picoseconds, is employed for the SFG imaging experiment. The Nd:YAG is the acronym for neodymium-doped yttrium aluminum garnet ($Nd:Y_3Al_5O_{12}$). The repetition rate of this laser is 20 Hz and maximum output energy is around 40 mJ. This laser consists of a laser head, a power supply and a cooling unit. The external picture and sketch of the laser head are shown in Figure 2-4 and Figure 2-5, respectively. There includes three main parts in laser head which are master oscillator, regenerative amplifier, and power amplifier, respectively.

The master oscillator is a diode pumped passively mode-locked where the Nd:YVO_4 material is employed. The oscillator was pumped by a temperature controlled 2.5 W laser diode coupled to the optical fiber. A saturable absorber was employed to achieve mode-locking mode. There had two output beams in the master oscillator. One was used as the seed beam for regenerative amplifier which passes polarizers P1 and P2, retardation plate HWP2, Faraday rotator FR1 and being directed to a regenerative amplifier by polarizers P3 and P4. Another one, which was reflected by M22 and M23, arrived the PHD1 to monitor the output energy of master oscillator.

The regenerative amplifier is based on a Nd:YAG rod R2 pumped by a diode laser LD2. The combination of M8 and M9 acts as the cavity mirrors of the regenerative amplifier, while the combination of M10, M11 and M12 serves as the retro reflector to improve the long-term stability of laser cavity. The polarizer P4 and Pockels cell PC1 introduce the seeding beam from master oscillator into regenerative amplifier cavity and the amplified laser pulse from the regenerative amplifier cavity into power amplifier, respectively. The voltage on PC1 is switched on to feed the laser cavity with the seeding beam. After 25-28 round trips in the laser cavity the laser pulse gets saturated. Then the voltage on the PC1 is switched off to dump the pulse out from the regenerative amplifier cavity. The Faraday rotator FR1, half wave plate HWP2 and polarizer P1 are used to prevent the amplified pulse beam proceeding from the regenerative amplifier to the master oscillator. Consequently, the amplified pulse is sent into the power amplifier.

After leaving the regenerative amplifier, the amplified pulse passes through M3, M4 and M15 into another amplifier contained Nd:YAG rod R3 pumped by a flash lamp.

The amplified laser pulse is vertical polarized and reflected by the polarizer P5 and P6 to outside. The amplification level of the laser is controlled by tuning the delay time between the regenerative amplifier with the amplifier flash lamps. The amplification level could be adjusted from 1 to 100 on the control pad. The amplification 100 corresponds to the optimum delay between amplifier lamp flashes and generator lamp flashes.

2.2.2. Optical Parametric Generator/Amplifier (OPG/OPA)

The main function of the OPG/OPA system (LaserVision Inc), is empolyed to generate a fixed 532 nm pulsed laser pulse and a tunable infrared laser pulse (2000-4000 cm^{-1}).[36] The detail sketch of the OPG/OPA is illustrated in Figure 2-6.[33]

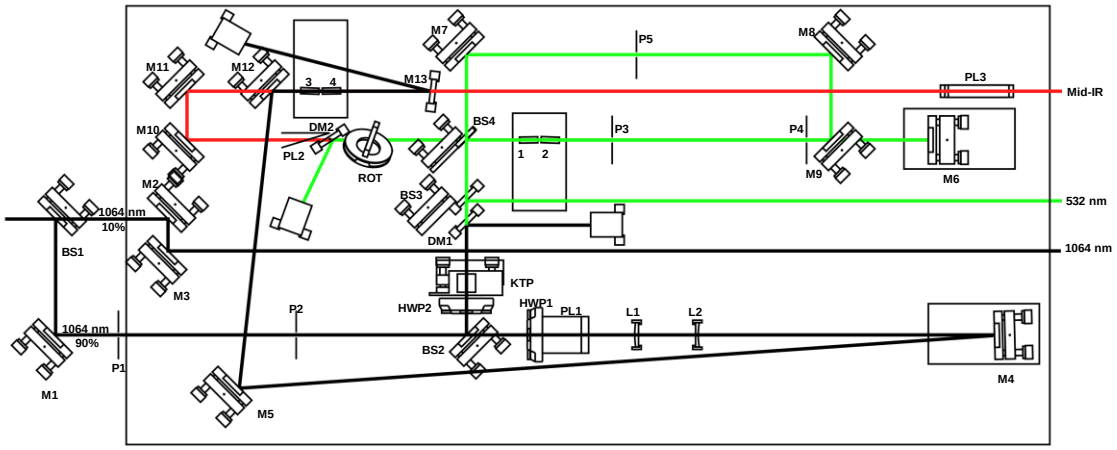

Figure 2-6. Optical layout of OPG/OPA system. Note: this figure is obtained from Dr. Katherine Cimatu's PhD thesis.[33]

The fundamental 1064 nm pulsed laser beam is directed towards a beam splitter (BS1) and split into two separate beams. One part of 1064 nm laser beam with 10% energy is directed to pass the M2 and M3 and dumped out from the OPG/OPA served as the pump beam for the SFG imaging system. Another part of 1064 nm laser beam with 90% energy

is reflected by BS1, M1 and split by the BS2. After BS2, one part of 1064 nm beam is sent to a delay stage (M4) for the Difference Frequency Generation (DFG) process in crystals 3 and 4. The combination of HWP1, polarizer, PL1 is used to adjust the power intensity and control the polarization of the 1064 nm beam. The M5 and M12 are used to direct the 1064 nm beam into the crystals 3 and 4. A telescope combination of plano-convex lens L1 and plano-concave lens L2 is applied to control the beam size.

Reflected 1064 nm beam from BS2 passes through a Potassium Titanyl Arsenate (KTA) crystal to generate the 532 nm beam. The polarization of the fundamental beam is controlled by the HWP2 to match the crystal orientation to optimize the second harmonic conversion. After going through the crystal 1 and 2, remained 1064 nm beam is cut by the dichroic mirror, DM1. BS3 is used to separate the 532 nm beam into two parts. The first part serves as a pump beam for another separate SFG vibrational spectroscopy set-up. The second part is projected onto BS4 and divided into two parts. The first part of beam is sent to a pair of Potassium Titanyl Phosphate crystals (KTP), while another part of beam is sent to M7, M8, and M9. This part is the second pass going through the crystals with more photons be generated. Such optical process is called optical parametric amplification (OPA) process. Once the 532 nm beam passes through the KTP crystals, two individual beam with different frequency known as signal beam and idler beam are generated.

The signal beam and idler beam are reflected by M6, which is placed on a delay line to adjust the delay time between signal and idler beams. Such fine adjustment makes sure that the signal and idler beam arrives M9 at the same time as the second pass of 532 nm beam. After arriving, those three beams are projected to the KTP crystals. The delayed

532 nm beam pumps the crystals, while the reflected signal and idler beams stimulate the crystals. This optical process that amplifies the signal and idler beams is known as the OPA process. The idler beam gets greatly enhanced and becomes more stable to serve as a seed beam for DFG process in the next crystal stage.

The left signal beam and 532 nm beam are filtered by DM2 and silicon polarizer, PL2. The magnesium fluoride rotator, ROT adjustes the polarization of the idler beam to parallel polarized. The idler beam and 1064 nm beam arrive the KTA crystal, 3 and 4 at the same time and perform the DFG process. The 1064 nm beam and idler beam serve as pump beam and stimulation beam in DFG process to generate another set of signal and idler beam, respectively. The remaining 1064 beam and idler beam are removed by M13 and PL3, respectively. The signal beam is projected out from the OPG/OPA system as the IR beam for SFG process. By rotating the first crystal and second crystal horizontally, the wavenumber of mid-IR is tunable from ~2000 to 4000 cm^{-1}. The output intensity and spectral bandwidth of IR beam are 0.5 mJ and 8 cm^{-1}.

2.2.3. Optical path of SFG imaging experiment

For the SFG imaging experiment, two beams including the 1064 beam and IR beam are employed to generate SFG beam. The layout of optical path of 1064 beam and IR beam for the SFG imaging measurements is illustrated in the Figure 2-7 and Figure 2-8. Detailed optical components and alignment procedure are described elsewhere.[37]

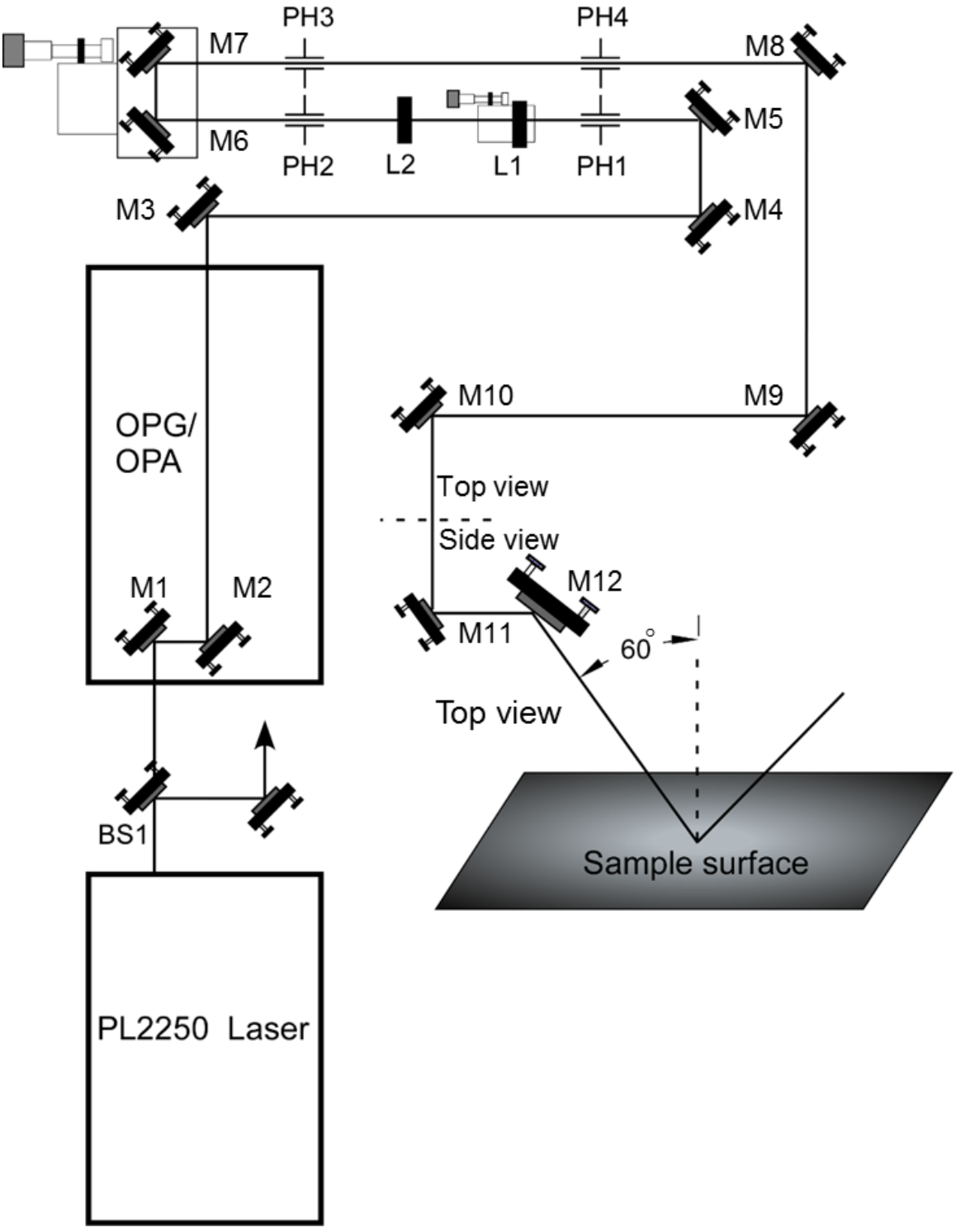

Figure 2-7. An outline of the 1064 nm beam before arriving the sample surface.

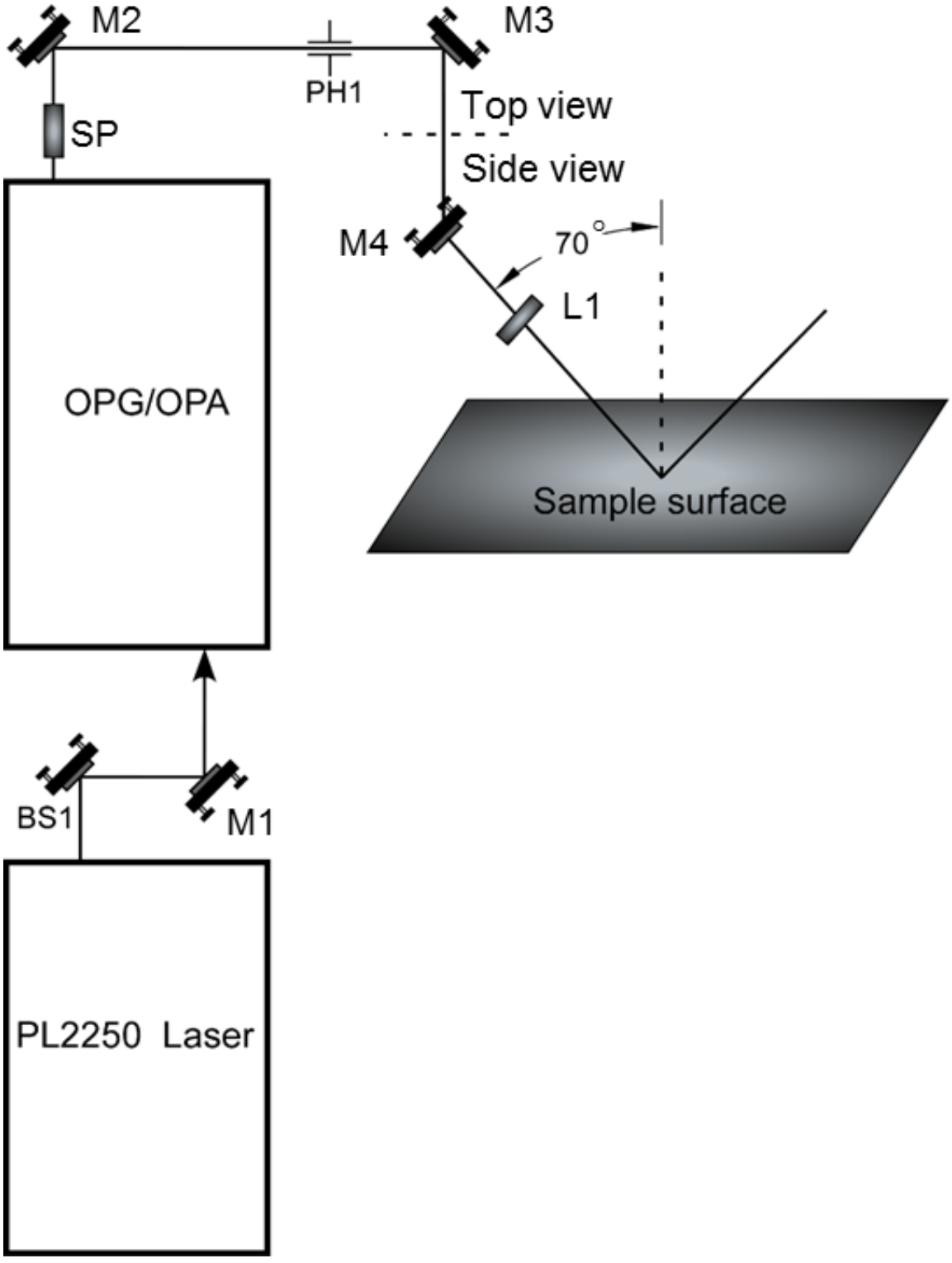

Figure 2-8. An outline of the IR beam until it arrives the sample surface.

The fundamental 1064 nm beam is generated by the picosecond laser, as shown in Figure 2-7. The beam energy is split into 90% and 10% by the beam splitter BS1. The 10% part is introduced into the SFG microscope by M1-M12 and impinges onto the sample surface with incident angle of 60°. A two lenses telescope system is placed between the pinholes PH1 and PH2 to adjust the 1064 nm beam size. The focal length of the lenses L1 and L2 are +200 mm and -100 mm, respectively.

Another 90% of 1064 nm beam is introduced into OPG/OPA to generated IR beam by M1 shown in Figure 2-8. After being generated from the OPG/OPA, mid IR beam is transferred to a germanium Brewster's angle polarizer to purify the polarization, then, impinges into SFG microscope by a series of silver mirrors, M2-M4. The mid IR beam arrives the sample surface at the same position with the 1064 nm beam. The incident angle of mid IR beam is set at 70°. A calcium fluoride plane-convex lens with a 200 mm focal is employed to shallowly focus the infrared beam onto the surface.

2.2.4. Description of new generation SFG microscope

The detail design and function of each optical components of last version SFG-imaging microscopy is described in detail elsewhere, and is only briefly outlined here.[37,38] Through several development of the SFG imaging set up, a new generation SFG microscope is built with higher spatial resolution and easier alignment strategy as shown in Figure 2-9.

The first adjustment is adding the 808 nm CW laser shown in Figure 2-10(A). As shown in Figure 2-11, the 808 nm CW laser beam is reflected by M1, M2, and M3, then,

arrives to the DM1 and get reflected by M4. The incident angle on the surface is fixed at 62.1° to match the emission angle of the SFG beam. Reflected laser beam is collected by the imaging-detection system which is composed of relay lens, diffraction grating, 10 X objective lens, and focus lens.

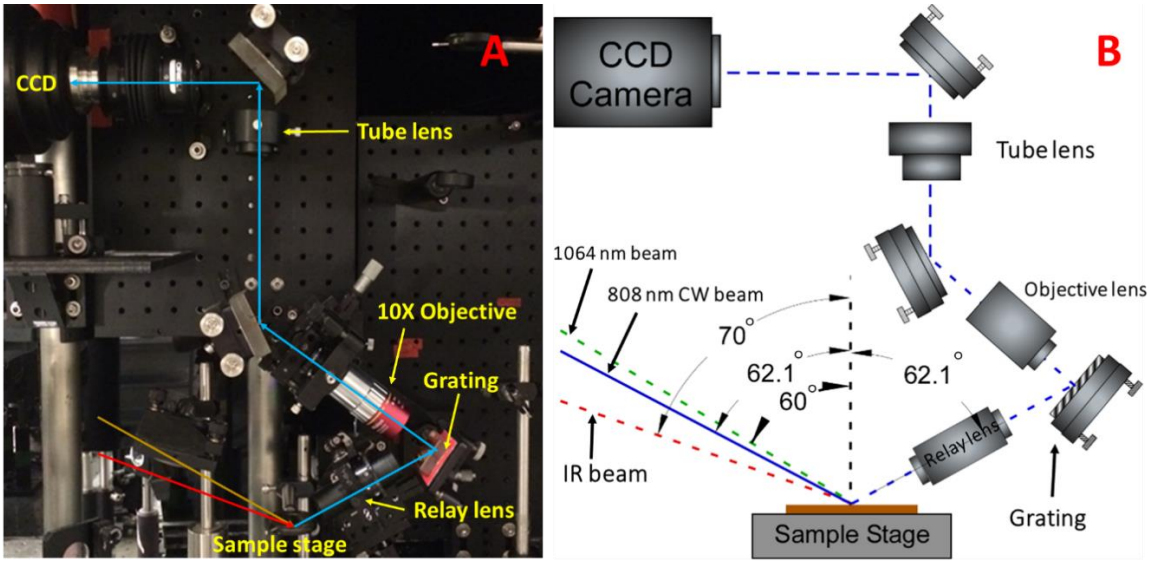

Figure 2-9: (A) The picture of the new generation SFG microscope; (B) The schematic diagram of the new generation SFG microscope.

Eventually, the magnified optical image is collected by the same CCD camera used to acquire the SFG image. Since the wavelength of SFG beam for C-H stretching mode (2700-3050 cm^{-1}) is from 803 to 826 nm, the optical image originated from the 808 nm CW laser has the approximately same focus, position, and view as the SFG image. Thus a synchronous optical microscope could be built by this 808 nm CW laser and used to align the SFG imaging system. The SFG signal is relatively weak. So the image acquisition time for single wavelength image is as long as 1 mins. With the guidance of such synchronous optical microscope, the alignment of the SFG imaging system is much easier. Additionally, such optical microscope shares the same sample position as the SFG microscope.

Consequently, it provides a very useful reference image of the interpretation of SFG image. Another optical adjustment is a 45mm Focal Length f/4, Relay Lens (Edmund optics) served as a 1:1 telescope shown in Figure 2-10(B).

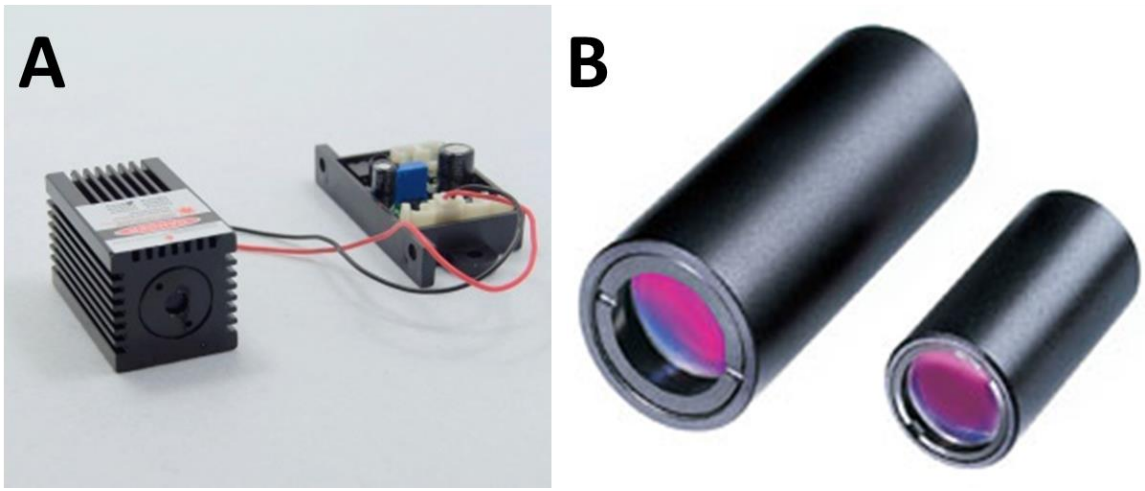

Figure 2-10: (A) The picture of 808 nm CW laser; (B) The picture of 45mm Focal Length f/4 Edmund relay lens (45-760)

Compared with a homemade 1:1 telescope including a pair of ACHR 200 and ACHR 60 lens used in previous SFG microscope, this relay lens has a higher numerical aperture (0.26). It helps to maintain a higher spatial resolution. Besides that, the optical design of this relay lens greatly diminish spherical and chromatic aberration.

The sketch of SFG imaging set up is illustrated in Figure 2-9(B). The incidence angle of the IR beam and 1064 nm beam are set at 70º and 60º, respectively. The SFG beam is generated at an angle of 62.1°. Since the SFG beam emission direction is tilted by 22.9° from the surface normal, a diffraction grating (Newport, 53004BK01-701R) is employed to project the intermediate focused image perpendicularly onto the focal plane of the objective lens.[39] As shown in Figure 2-12, the grating used for SFG imaging has 1000

grooves per mm, blaze angle of 26.9° and a blaze wavelength of 776 nm. The diffraction grating is tilted by 22.9° to align the incident beam at 55.8° from optical axis of the microscope objective lens. The surface of grating is set to be perpendicular to the optical axis of microscope system to match the direction of first order diffraction of the SFG beam. The SFG beam goes through the 45mm Focal Length f/4, Relay Lens (Edmund optics 45-760), then, impinges onto the diffraction grating at the first order diffraction angle. In this way, the SFG signal is diffracted perpendicular to the grating plane, which allows the entire field of view in focus. A short-pass filter with the cut off wavelength of 890 nm (900 AESP Omega Optical) is placed in the front of the relay lens to prevent the 1064 nm laser beam entering and damaging the telescope components and CCD camera.

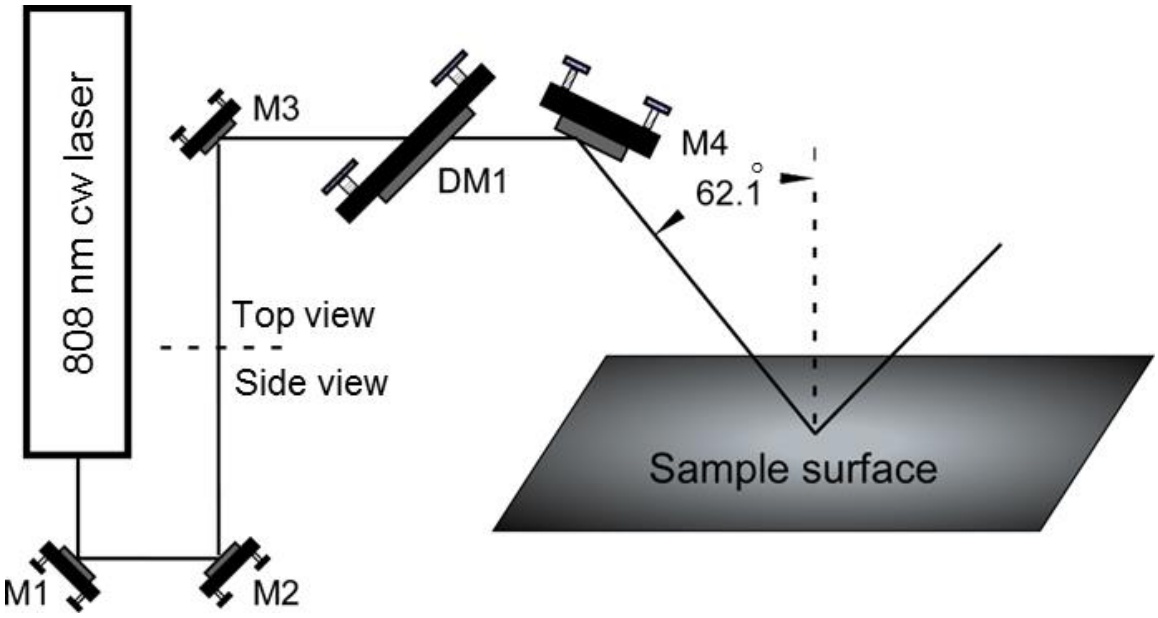

Figure 2-11: An outline of the 808 nm CW laser reference beam until it arrives the sample surface.

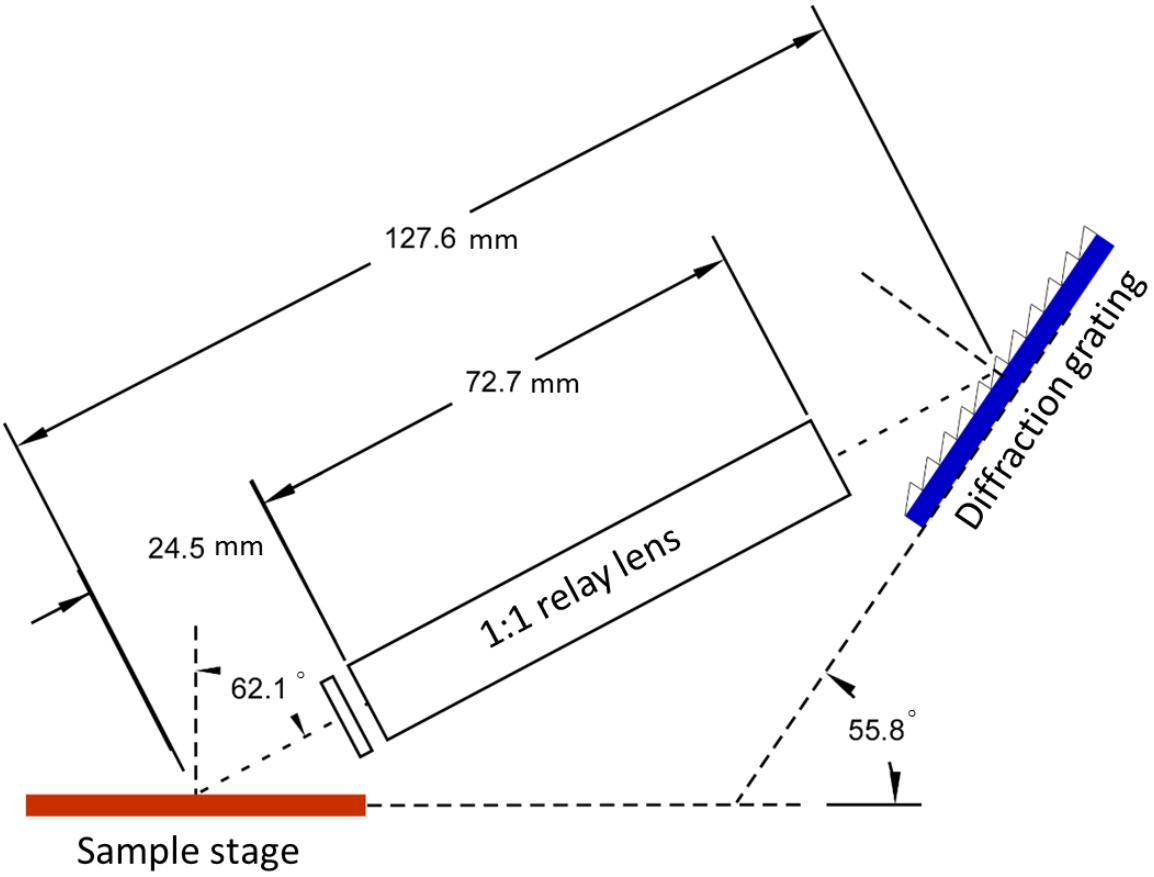

Figure 2-12: Sketch of sample state-relay lens-diffraction grating.

After the grating, the SFG image is acquired by microscope components and CCD camera. The microscope component consists of a 10X infinity-corrected long working distance of 30.5 mm objective lens (Mitutoyo 378-824-1), a pair of gold mirror (Newport, 20SD520-ER.4) and a tube lens (Edmund, NT56-073). The 10X objective lens with an infinity-corrected long working distance is positioned perpendicular to grating surface to magnify the beam 10 times its initial size. A pair of gold mirror is set to reflect the SFG signal in the direction parallel to CCD optical axis. The tube lens (200 mm focal length) is placed for collimating the intermediate image. A 1064 nm holographic notch filter (Kaiser, HNPF-1064.0-1.0) is positioned after the microscope to cut any remained 1064 beam.

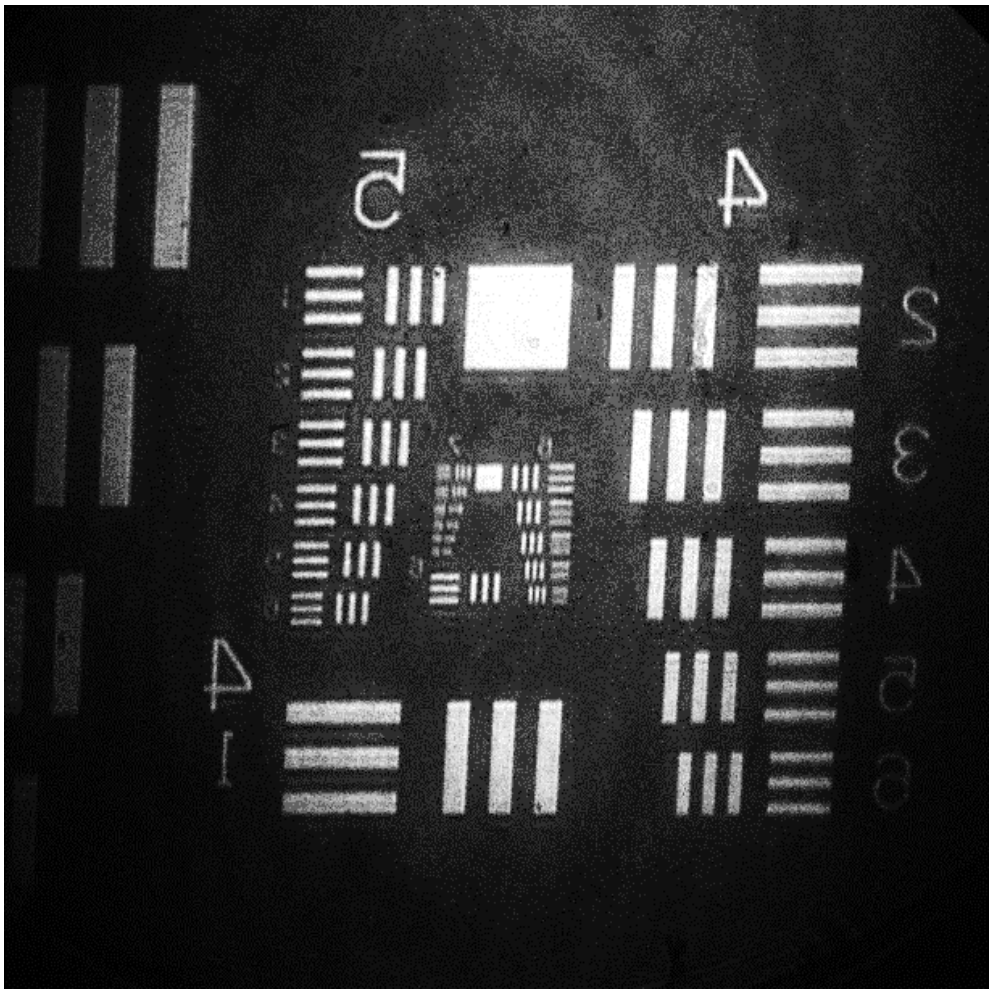

Figure 2-13: Optical image of USAF 1951 test pattern obtained through SFG imaging system with light source of 808 nm optical laser.

The 1024×1024 pixels charged coupled device (CCD) camera is mounted 200 mm away from the tube lens to collect the SFG image. The CCD is an intensified camera (ICCD) with a Gen III intensifier (Roper Scientific, USA). The ICCD camera has ability of gating to collect the signals in a specifically desired temporal window (100ns) to avoid integration over background light and noise. The temperature of ICCD camera is maintained at -20 °C to reduce the background noise. An area of the order of 1024×1024 pixels could be illuminated in a single SFG image and 1 pixel is corresponding with about 1 μm distance

on the surface. Figure 2-13 demonstrates the optical image of USAF 1951 test pattern which illustrates that the spatial resolution of SFG microscope is around 1 μm.

2.2.5. SFG imaging experimental procedure

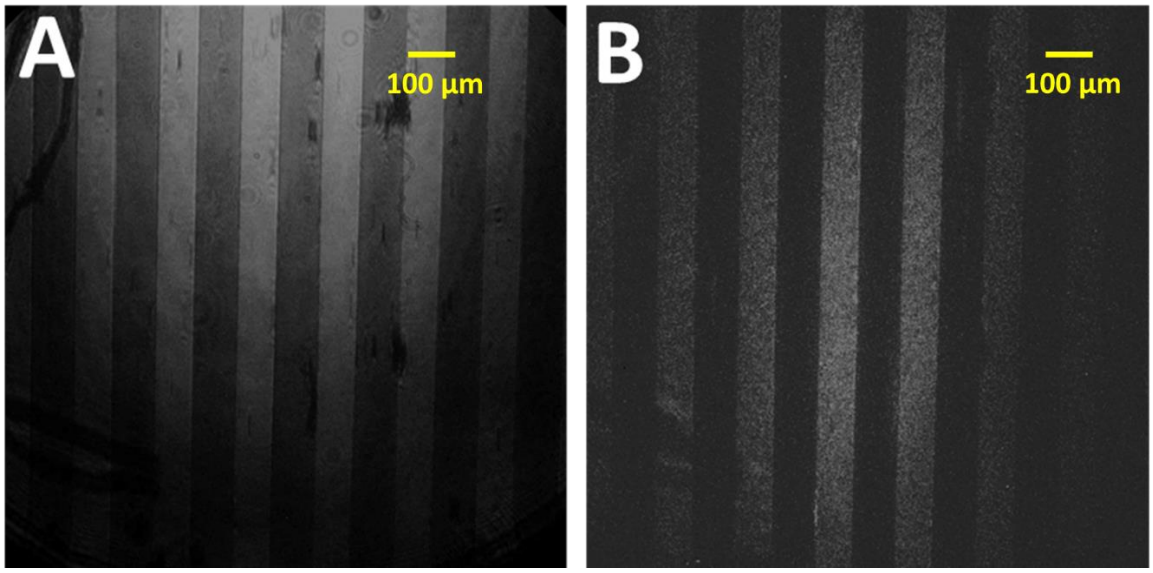

Figure 2-14: (A) Optical image (B) SFG image of gold strip pattern sample (showing features of 100 μm in length scale).

Accurate and precise alignment is of prime importance for obtaining a good SFG image with high signal, low noise, and minimal image distortion. The 1064nm and the tunable IR beam are aligned towards the sample stage using an iris diaphragm that is attached on a magnetic base plate screwed onto the laser table, which makes sure that two beams overlap on sample surface timely and spatially. The SFG beam is aligned using an 808 nm CW laser shown in Figure 2-10 with the same iris diaphragm. Three marks for three beams are to be found on the table as references for two-point adjustments.

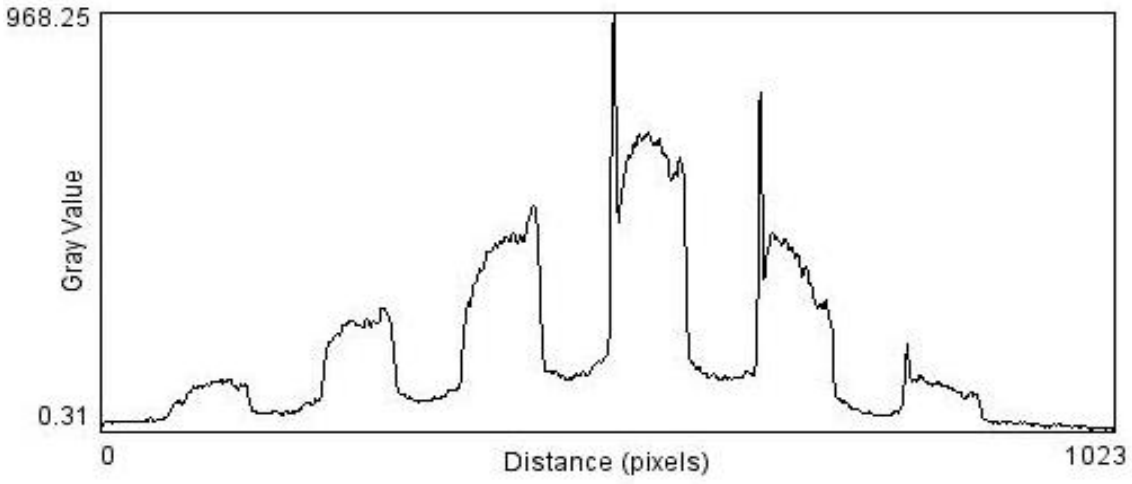

Figure 2-15: SFG line profile extracted from Figure 2-14(B).

After the alignment of the beams, the sample stage is placed back to replace the iris diaphragm. A clean stripped patterned (100 μm) sample of evaporated gold on silicon wafer will be used as the reference sample for finding the focus of SFG imaging setup (shown in Figure 2-14). With the guidance of 808 nm CW laser, the reference sample is aligned via the sample stage adjustments onto the two iris diaphragms after the diffraction grating. The diffraction grating is aligned towards a separate iris diaphragm with 808 CW laser. The CCD camera is turned on after the proper alignment of SFG imaging system. A Winspec program to controls all the functions of the CCD camera, is launched at same time. The mode of operation is always set at safe mode, and the controller temperature is set at -20 °C.

To maximize the SFG signal, the spectroscopy mode of the CCD camera is employed. The number of gates per exposure is set at 10. With employment of the spectroscopy mode for CCD camera, a SFG line profile (shown in Figure 2-15) is obtained to maximize the SFG signal.

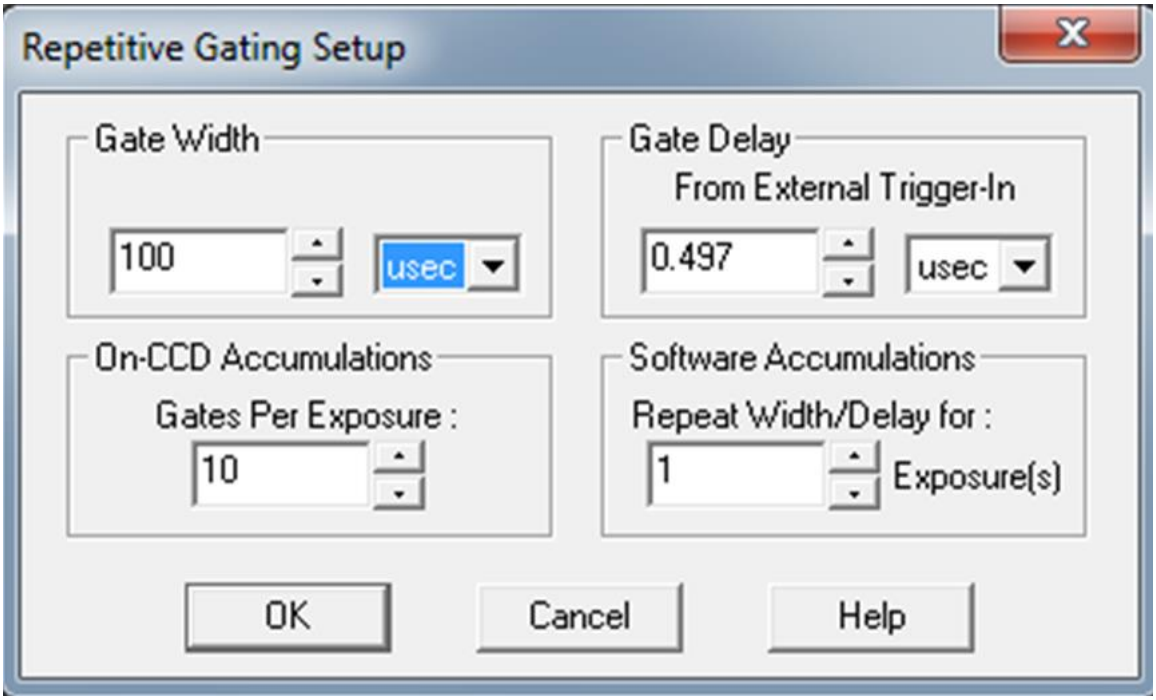

Figure 2-16: The gating setup window for the CCD camera.

From the setup pulser tab, the number of gates per exposure is set at 10, which means that that accumulation number for one image is 10. And the gate width is set at 100 ns. When running in image mode, the number of gates per exposure is typically set at 1000 or 3000, while the gate width keeps same. When the microscope is employed to acquire the optical image, the gate width is at 100 μs, and the number of gate per exposure is set at 10 (shown in Figure 2-16). The microscope is run using gate mode for all image acquisition including the optical image and SFG image.

2.2.6. SFG imaging data processing

A schematic diagram of the spectrum extraction and analysis of SFG image is illustrated in Figure 2-17. When the SFG imaging experiment is performed, the IR frequency is continuously tuned in a designed base speed by Laservision program and a

series of SFG images is collected in a sequence. The SFG images are transferred from ICCD camera to computer continuously at 5 cm^{-1} interval. Then all the SFG images are stacked according to increasing IR frequency using the ImageJ program. With a PlugIn called stack reverser, the order of the image stack is reversed. The brightness/contrast tab is used to control the brightness of the SFG image. The local SFG spectra are extracted from the SFG image stack by ImageJ software with the PlugIn called spectral spectroscopy. The macros program is employed to extract hundreds of spectra and save each spectral data into .txt files, which can be processed using a spectral fitting program written in Mathematica. Normally, an area of the order of 1024×1024 pixels is illuminated in a single SFG image. For ROIs with a size of 10×10 pixel each, a total of 100×100 SFG spectra are extracted and fitted using the same initial values and constraints for all spectral parameters. The fitted spectral parameters such as amplitudes, peak widths and phase are employed for surface contour mapping and histogram analysis.

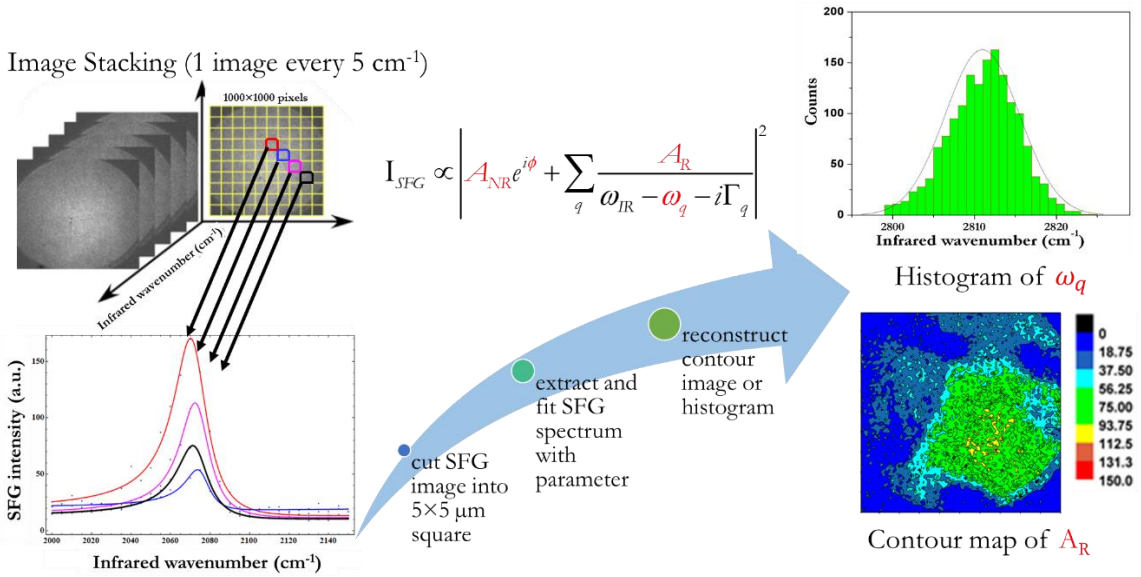

Figure 2-17: The analysis procedure of SFG image.

2.3. Ultra-high vacuum system (UHV)

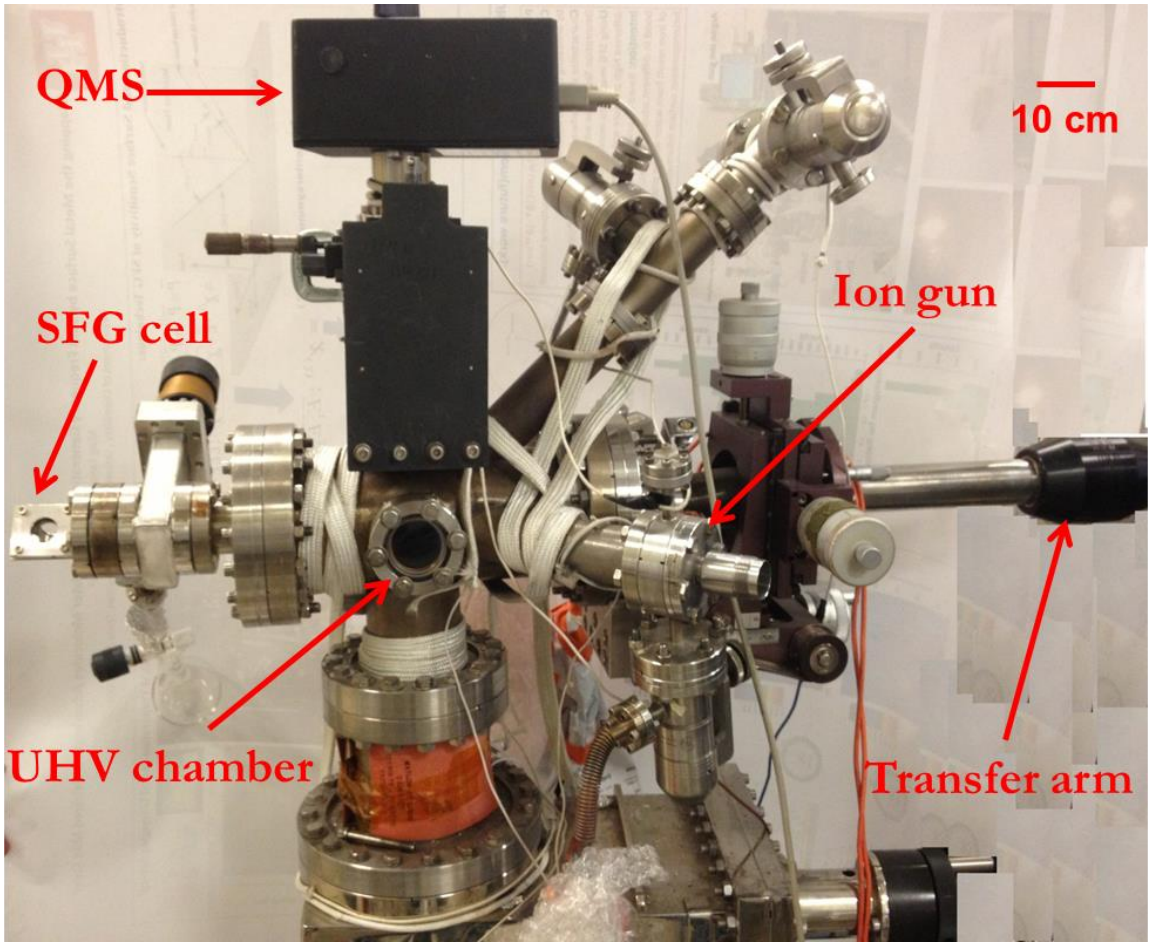

Figure 2-18: Picture of UHV setup used for the *in-situ* SFG microscopic studies of gas/metal interface.

For the metal/gas interface research, a fresh and atomic clean metal surfaces is crucial to acquire an accurate surface measurement. At 10^{-6} Torr, a metal surface could be covered by one monolayer of adsorbed species within 1 second assuming the sticking coefficient is 1. Besides that, some active metals such as zinc and magnesium are very easy to be oxidized in ambient environment, which causes surface component transformation.

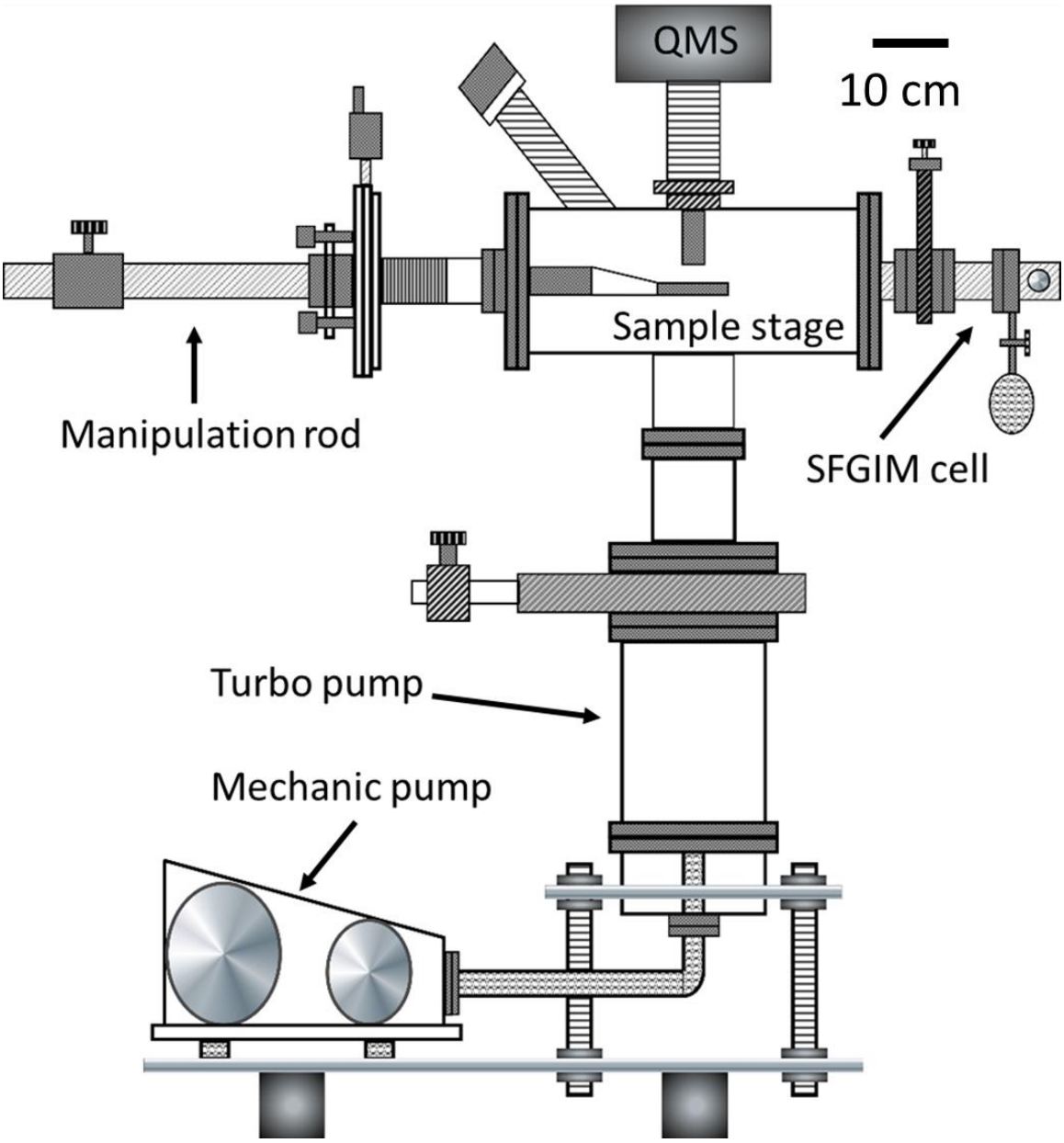

Figure 2-19: Schematic diagram of UHV setup used for the *in-situ* SFG microscopic studies of gas/metal interface.

To enable atomically clean surfaces to be prepared for study and such surface to be maintained in a contamination-free state for the duration of the experiment it is necessary to operate in ultra-high vacuum. Controlled exposure of the surface to adsorbates or other surface treatment could also be carried and maintained in ultra-high vacuum to obtain a

reliable measurement. Hence, in order to perform in-situ SFG microscope study on the metal surface especially on zinc, a UHV system which combines TPD with ion gun sputtering technique is built and schematically depicted in Figure 2-19. This UHV apparatus (shown in Figure 2-18) has three major functions including: (a) clean sample; (b) characterize sample cleanness; (c) transfer fresh clean metal sample to small SFG imaging cell to perform in-situ SFG imaging experiment.

The UHV system consisted of a two-stage pumping system with a base pressure of 10^{-9} Torr. A mechanical pump (Duoseal Vacuum Pump) pumps the main chamber pressure down to 1×10^{-3} Torr, and a turbo molecular pump (Leybold TMP) pumps the pressure down to the 4×10^{-9} Torr. The pressure is measured by three vacuum gauges including a thermocouple gauge (10-10^{-4} Torr), ionization gauges (10^{-4}-10^{-10} Torr), and a Quadrupole mass spectrometer (QMS) (10^{-4}-10^{-10} Torr). The sample stage is mounted on a sample holder, which is connected to the magnetic transfer arm. Hence the sample stage is able to be transferred linearly from the main chamber to the SFG cell for 12 inches distance and rotated 360° around transfer arm. The magnetic transfer arm is attached to a 5-axis XYZ manipulator. This manipulator is able to rotate, tilt and translate with more flexibility to move the sample stage.

2.3.1. Sample clean via annealing and argon ion sputtering

The sample is mounted on the sample stage in the UHV chamber. Homemade sample stage is shown in Figure 2-20. Metallic sample such as platinum is spot-welded on a tantalum foil and a UHV ceramic glue fastens the tantalum foil on the sample stage. An AC power supply provides about 10 A current to heat the tungsten wire to 800 K via

thermal radiation. In addition, low pressure (1×10^{-7} Torr) oxygen gas is dosed into the UHV chamber through leak valves as shown in Figure 2-18 to remove surface impurity while the surface temperature is maintained at 800 K. A K type thermocouple is spot-welded at the edge of sample surface to measure the surface temperature. Besides that, a 3000 ev ion gun (RBD) is employed to produce high speed argon ion beam. The ion beam bombards the sample surface to remove the impurity from the metal surface. A clean surface with well-defined defect concentration is typically achieved in this method.[40]

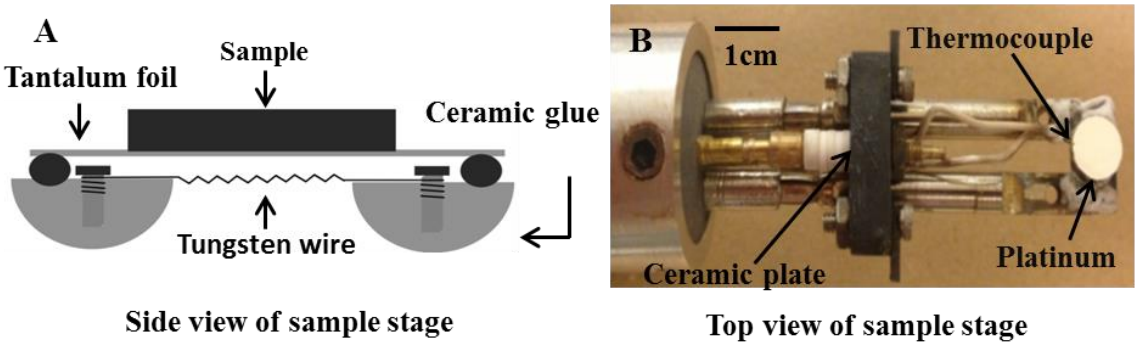

Side view of sample stage

Top view of sample stage

Figure 2-20: (A) Schematic diagram of sample stage (side view), (B) Picture of sample stage (top view)

2.3.2. Surface cleaning characterization

Temperature programmed desorption (TPD) is one of the most commonly used techniques in the studies of desorption kinetics of chemisorbed gases from solid surface.[41,42] In general, the metal surface is rigorously cleaned in UHV, following by a known gas being dosed into the UHV chamber at a defined input rate. The gas adsorbs on the sample surface spontaneously at room temperature in vacuum, then, desorbs by heating the sample in constant rate. As soon as the tungsten wire underneath the sample starts to heat the sample, the real time temperature data is recorded by the proportional integral derivative (PID) temperature controller (Barnert company) by employing a K-

thermocouple spot weld at the edge of sample surface. At the same time, the partial pressure of adsorbate is recorded by the QMS. The relationship between partial pressures with temperature named as TPD spectrum is achieved.

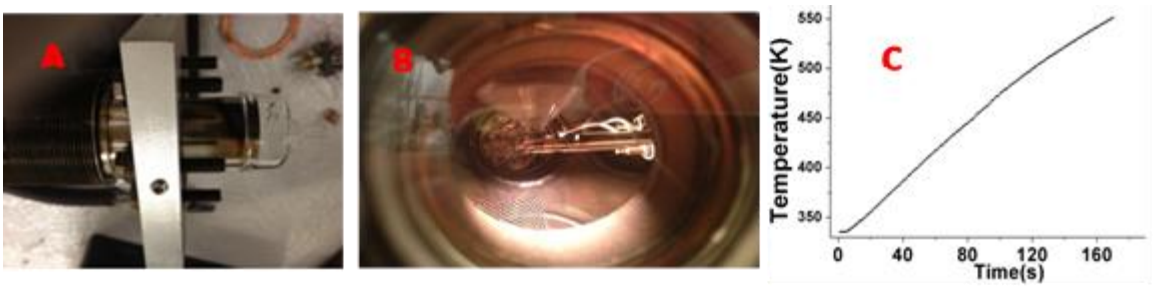

Figure 2-21: (A) QMS covered by glass shield. (B) Sample heating in UHV (QMS end 5 mm above the surface). (C) Linear sample heating plot (temperature vs time).

In this UHV system, the sample temperature is controlled by PID temperature controller. The PID temperature controller is able to increase the surface temperature in a linear rate through varing the on/off time ratio of AC-power supply based on the PID method. The pump speed of turbo pump (500 L/s) is relatively high compared to the volume of UHV chamber (30 L). Hence, the re-absorption of adsorbed gas could be neglected in this case.[41] The end of QMS probe is covered by a glass shield shown in Figure 2-21(A). The small hole of glass shield is about 0.5 cm^2 and placed 5 mm above the sample surface as shown in Figure 2-21(B) to make sure that the measured QMS signal is barely from surface. A sample linear temperature vs time relationship from CO adsorption on platinum surface is shown in Figure 2-21(C). A TPD spectrum (pressure vs. temperature) is obtained by combining the pressure-time plot with pressure-temperature plot.

2.3.3 Transfer sample to SFG cell and separate SFG cell from UHV system

Figure 2-22: (A) SFG cell mounted on optical sample stage which is ready for SFG-imaging experiment. (B) SFG cell with polished platinum sample inside.

The separation of sample stage from UHV system is of critical importance for such three points: 1) it prevents the laser and associated optical system from pump oil contamination of UHV system; 2) it helps SFG imaging system to keep it spatial resolution by ruling out of perturbation from pump system vibration; 3) The optical alignment for SFG cell is much easier compared with rotating and tilting a 20 inch long transfer arm. The general separation mechanism is based on a banana plug connection between heating rod with sample holder and a spring connection between thermos-couple rod with sample holder shown in Figure 2-21A. As soon as a clean surface is obtained, the sample stage is transferred from UHV chamber to SFG cell by manipulating the transfer arm. Two knobs at the two sides of the sample stage catch home-build lock-in SFG cell by rotating the transfer arm. Then the sample stage is separated from sample holder following pulling the transfer arm back to the UHV chamber. The sample stage gets locked in the SFG cell, and the sample holder is pulled back to the UHV chamber. The gate valve between UHV chamber and SFG cell is closed and ambient pressure gas is dosed into the SFG cell to adsorb on the metal surface. The SFG cell is directly mounted on a homemade optical sample stage shown in Figure 2-22(B) for SFG imaging measurement. This SFG cell is

equipped with 1 inch CaF_2 and quartz windows which serve as the entrance and exit port for the laser beam and SFG signal shown in Figure 2-22(B).

2.4. Annealing oven with hydrogen flow

It has been proved that the copper surface contains many structures, namely, polycrystalline facets, grain boundaries, and annealing twins after high temperature processing.[43] To investigate the surface chemistry heterogeneities on such copper surface induced by the grain structure, a tube furnace (Lindberg) with combination flow of hydrogen with argon is built and presented in Figure 2-23.

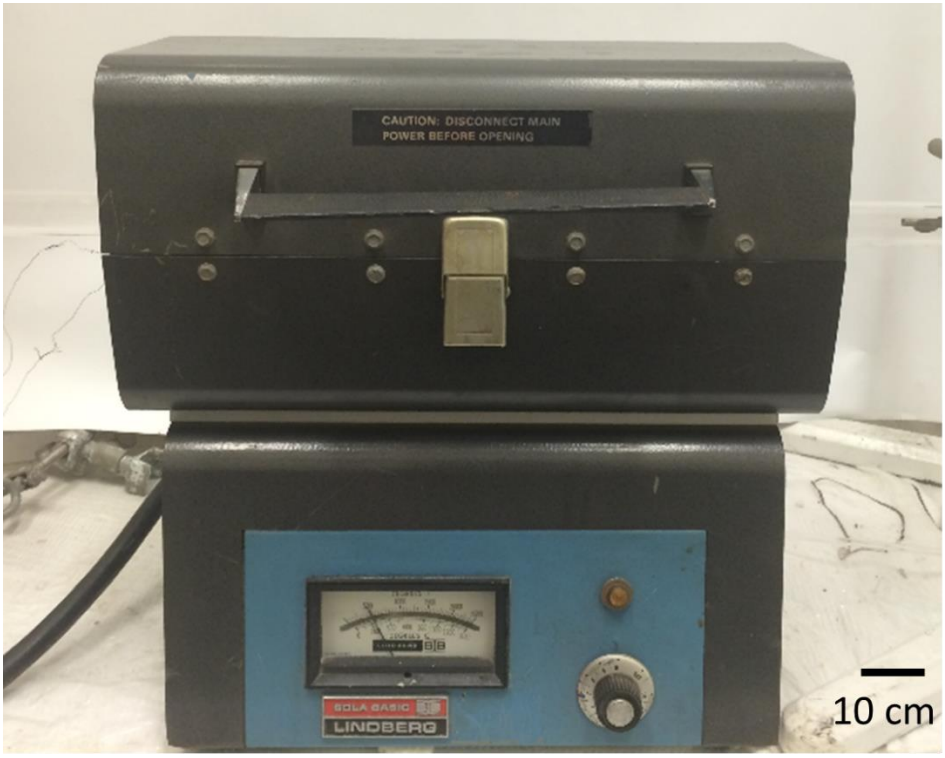

Figure 2-23: The picture of tube furnace (Lindberg).

The schematic sketch of tube furnace set-up is demonstrated in Figure 2-24. The temperature of tube furnace is measured and controlled by the Barnert temperature controller. The maximum temperature is around 1500 °C. Normally, the micrometer size

grain structure on copper grows at 1050 °C. The common flow rate is controlled by the flowmeter (shown in Figure 2-23) at 270 sccm for argon gas and 30 sccm for hydrogen gas, respectively.

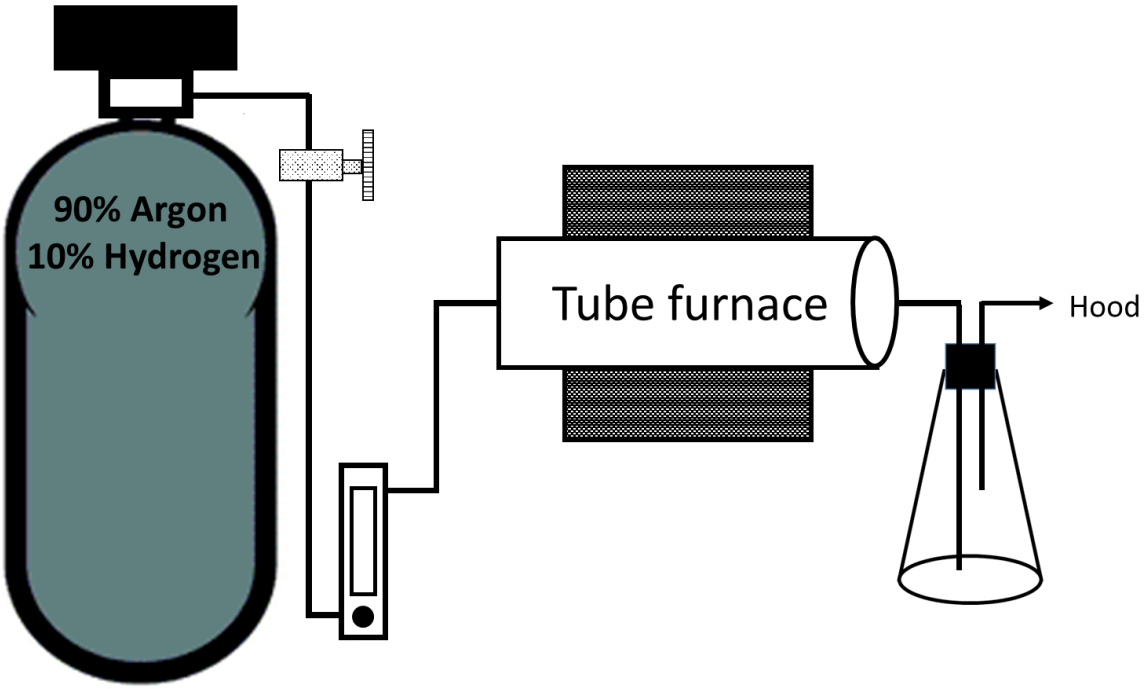

Figure 2-24: Schematic sketch of tube furnace set-up

2.5. References

(1) Shen, Y. R. *Nature* **1989**, *337*, 519.

(2) Zhu, X. D.; Suhr, H.; Shen, Y. R. *Phys. Rev. B* **1987**, *35*, 3047.

(3) Hirose, C.; Yamamoto, H.; Akamatsu, N.; Domen, K. *J. Phys. Chem.* **1993**, *97*, 10064.

(4) Bain, C. D. *J. Chem. Soc. Faraday Trans.* **1995**, *91*, 1281.

(5) Miranda, P. B.; Shen, Y. R. *J. Phys. Chem. B* **1999**, *103*, 3292.

(6) Wang, J.; Clarke, M. L.; Chen, Z. *Anal. Chem.* **2004**, *76*, 2159.

(7) Stiopkin, I. V.; Jayathilake, H. D.; Bordenyuk, A. N.; Benderskii, A. V. *J. Am. Chem. Soc.* **2008**, *130*, 2271.

(8) Cimatu, K.; Baldelli, S. *J. Phys. Chem. B* **2006**, *110*, 1807.

(9) Santos, C. S.; Baldelli, S. *J. Phys. Chem. B* **2007**, *111*, 4715.

(10) Buck, M.; Himmelhaus, M. *J. Vac. Sci. Technol. A* **2001**, *19*, 2717.

(11) Lambert, A. *J. App. Spec. Rev* **2005**, *40*, 103.

(12) Shen, Y. R. Principles of nonlinear optics. Wiley: **1984**.

(13) Zhu, X.; Suhr, H.; Shen, Y. *Phys. Rev. B* **1987**, *35*, 3047.

(14) Shen, Y. *J. Phys. Chem. C* **2012**, *116*, 15505.

(15) Eisenthal, K. B. *Acc. Chem. Res.* **1993**, *26*, 636.

(16) Huang, J. Y.; Shen, Y. R. In *Laser Spectroscopy and Photochemistry on Metal Surfaces*; Dai, H. L., Ho, W., Eds.; World Scientific, 1995; Vol. 5.

(17) Lambert, A. G.; Davies, P. B.; Neivandt, D. J. *Appl. Spectrosc. Rev.* **2005**, *40*, 103.

(18) Boyd, R. W. *Nonlinear optics*; Elsevier, **2008**.

(19) Zhuang, X.; Miranda, P.; Kim, D.; Shen, Y. *Phys. Rev. B* **1999**, *59*, 12632.

(20) Guyot-Sionnest, P.; Chen, W.; Shen, Y. R. *Phys. Rev. B* **1986**, *33*, 8254.

(21) Ye, P.; Shen, Y. R. *Phys. Rev. B* **1983**, *28*, 4288.

(22) Bagchi, A.; Barrera, R. G.; Dasgupta, B. B. *Phys. Rev. Lett.* **1980**, *44*, 1475.

(23) Bagchi, A.; Barrera, R. G.; Fuchs, R. *Phys. Rev. B* **1982**, *25*, 7086.

(24) Shen, Y. R. *Annu. Rev. Phys. Chem.* **1989**, *40*, 327.

(25) Wang, H. F.; Velarde, L.; Gan, W.; Fu, L. *Annu. Rev. Phys. Chem.* **2015**, *66*, 189.

(26) Lu, R.; Gan, W.; Wu, B. H.; Chen, H.; Wang, H. F. *J. Phys. Chem. B* **2004**, *108*, 7297.

(27) Superfine, R.; Guyot-Sionnest, P.; Hunt, J.; Kao, C.; Shen, Y. R. *Surf. Sci.* **1988**, *200*, L445.

(28) Harris, A.; Chidsey, C.; Levinos, N.; Loiacono, D. *Chem. Phys. Lett.* **1987**, *141*, 350.

(29) Potterton, E.; Bain, C. *J. Electroanal. Chem.* **1996**, *409*, 109.

(30) Wang, H. F.; Gan, W.; Lu, R.; Rao, Y.; Wu, B. H. *Int. Rev. Phys. Chem.* **2005**, *24*, 191.

(31) Moad, A. J.; Simpson, G. J. *J. Phys. Chem. B* **2004**, *108*, 3548.

(32) Hirose, C.; Akamatsu, N.; Domen, K. *Appl. Spectrosc.* **1992**, *46*, 1051.

(33) Cimatu, K. L. A., *Sum frequency generation imaging microscopy*. University of Houston, 2008.

(34) Buck, M.; Himmelhaus, M. *J. Vac. Sci. Technol. A-Vac. Surf. Films* **2001**, *19*, 2717.

(35) Shen, Y. R. *Nature* **1989**, *337*, 519.

(36) Zhang, J. Y.; Huang, J. Y.; Shen, Y. R. *Optical parametric generation and amplification*; CRC Press, 1995; Vol. 19.

(37) Cimatu, K. Ph.D., University of Houston, 2008.

(38) Cimatu, K.; Baldelli, S. *J. Phys. Chem. B* **2006**, *110*, 1807.

(39) Chastang, J. C. In *1983 International Techincal Conference/Europe*; International Society for Optics and Photonics: 1983, p 239.

(40) Verheij, L. K.; Hugenschmidt, M. B.; Cölln, L.; Poelsema, B.; Comsa, G. *Chem. Phys. Lett.* **1990**, *166*, 523.

(41) Redhead, P. *Vacuum* **1962**, *12*, 203.

(42) Holbert, V. P.; Garrett, S. J.; Bruns, J. C.; Stair, P. C.; Weitz, E. *Surf. Sci.* **1994**, *314*, 107.

(43) Wood, J. D.; Schmucker, S. W.; Lyons, A. S.; Pop, E.; Lyding, J. W. *Nano Lett.* **2011**, *11*, 4547.

CHAPTER 3. Roles of Oxygen for Methanol Adsorption on Polycrystalline Copper Surface Revealed by Sum Frequency Generation Imaging Microscopy*

3.1. Introduction

The adsorption of methanol on metal surfaces has been widely studied as a model system in both fundamental surface science and industry due to a number of relevant heterogeneous catalytic reactions such as hydrogenation of CO to methanol and syntheses of formaldehyde.[1-5] The methoxy fragment is always produced following methanol adsorption as a stable and abundant species at room temperature and it has been proved to be an important intermediate during industrial methanol and formaldehyde production with well-documented use of metal and metal oxide catalysts.[2,6] The generation of methoxy group requires copper atoms to induce metal activated O-H bond scission on the adsorbed methanol atom. In many cases, such process can be promoted with the assistance of the adsorbed oxygen.[2,6-9] However, in some conditions the formate group is identified on copper surface as a less abundant but more stable intermediate following methanol adsorption.[4,10]

A variety of surface science techniques have been performed to detect methanol adsorption on the copper surface, such as Electron Energy Loss Spectroscopy (EELS), Low Energy Electron Diffraction (LEED), Auger Electron Spectroscopy(AES), X-ray Photoelectron Spectroscopy (XPS) and Temperature Programmed Desorption (TPD).[6-8,11-

*Reproduced in part with permission from *Surf. Sci.* **2015**, 648, 35, ©2015 Elsevier

[13] While these traditional surface science techniques could only be operated in ultra-high vacuum (UHV) conditions, with a large enough free mean path for the ion or electron to reach the sample or be collected by detectors, many interesting surface phenomena including the adsorption of methanol were uncovered.[14,15] However, realistic heterogeneous catalytic reactions are mostly carried out in a high pressure environment, which are essential in understanding the mechanism of methanol adsorption under atmospheric pressure. Vibrational spectroscopy is generally a very powerful tool to deduce the chemical identity and structure of adsorbates on the surface. Nevertheless spectroscopic studies are typically based on an assumption that metal surface is homogeneous within the involved field-of-view on the sample. By analyzing an average response over the probe area without any spatial resolution, local heterogeneities (i.e., surface defects, molecular coverage, chemical composition, etc.) would be overlooked. Even though scanning probe microscope (SPM) studies (i.e., atomic force microscope and scanning tunnel microscope) have investigated the copper surface with atomic resolution, these techniques could only provide a limited range of chemical information.[16,17] Thus modeling of methanol adsorption on the heterogeneous metal surface, emphasizes the importance of in-situ molecular level spectroscopic studies of adsorbed species with spatial resolution under practical catalytic conditions.

Sum frequency generation (SFG), as a vibrational spectroscopic technique, provides chemical information through a more specific identification of chemical functionalities and conformational order of molecular layer within a broad temperature and pressure range. Comparing with other linear vibrational spectroscopy techniques such as IRAS, and EELS, SFG is intrinsically surface sensitive based on the fact that this second-

order nonlinear optical process is forbidden in isotropic medium. Various catalytic reactions such as CO oxidation[18] and hydrocarbon conversion[19] on transition metals has been successfully investigated by SFG, which demonstrates its applicability for studying gas interaction with metal surface. Lin, *et al.* employed the SFG to in-situ probe the polycrystalline copper surface during methanol synthesis and identified the formation of formate intermediate on copper surface.[10] Shultz *et al.* applied SFG to identify the methanol and methoxy species on anatase TiO_2 nanoparticle film.[20] A very recent study, using SFG vibrational spectroscopy to study the dissociation and photo-oxidation reaction of CH_3OH on the TiO_2 thin film, demonstrates that O_2 promotes CH_3OH dissociation and produces more methoxy adsorbed on the TiO_2 thin film.[21] Considering the presence of local features and heterogeneities of metal surfaces, SFG imaging, shows unique advantages for investigating chemical processes on metal surface with spatial and chemical resolution.[22,23] In this paper, SFG imaging has been employed to study the methanol adsorption on polycrystalline copper at atmospheric condition. The aim of this paper is to present the two-dimensional distribution of conformational information of the methoxy monolayer heterogeneity and clarify the role of oxygen in affecting the heterogeneity of the methoxy monolayer and copper surface. From the TPD and SFG imaging results, the major surface product, methoxy, is chemically identified and the conformation order of methoxy monolayer is characterized. The oxygen exposure promotes the formation of the methoxy monolayer and, hence, increases the surface density of monolayer with homogeneous arrangement on the copper surface.

3.2. Experimental section

3.2.1 Sum frequency generation process

In previous works, SFG theory has been described in detail.[24-27] To minimize the background noise, the 1064 nm beam is selected to as the pump beam for SFG imaging experiments, instead of 532 nm which is a more common choice in previous SFG studies.[28-30] Equation 3-1 demonstrates the tensor $\chi_{eff}^{(2)}$ consists of two terms, which is the non-resonant term $\chi_{NR}^{(2)}$ from the substrate contribution and the resonant term $\chi_{R}^{(2)}$ from the contribution of interfacial monolayer. The $\chi_{eff}^{(2)}$ is related to molecular hyperpolarizability $\beta^{(2)}$ through ensemble average over all possible molecular orientations including tilt angle (Θ), azimuth angle (φ), and rotation angle (ψ) as sketched in Figure 3-1. Equation 2-12 is the basis equation for the nonlinear curve fitting of the experimental SFG spectra. N, A_q, ω_{IR}, ω_q, and Γ_q denote the surface molecular density, resonant amplitude, IR beam frequency, resonant frequency and the damping factor of the q^{th} mode, respectively. When the frequency of the infrared beam ω_{IR} approaches the resonant frequency of q^{th} vibrational mode, the $\chi_{R}^{(2)}$ drastically changes in magnitude, as well as the SFG intensity, which is presented as a peak or dip in SFG spectra.

$$\chi_{eff}^{(2)} = \chi_{R}^{(2)} + \chi_{NR}^{(2)} = \sum_{q} \frac{N\left\langle \beta^{(2)} \right\rangle}{\omega_q - \omega_{IR} - i\Gamma_q} + \chi_{NR}^{(2)} \qquad \textbf{Equation 3-1}$$

Metal or semiconductor surfaces usually contribute to a strong non-resonant background $\chi_{NR}^{(2)}$ due to the nearly free electrons in the surface region. As shown in

Equation 3-1, SFG spectra are complicated by the convolution of $\chi_{\mathrm{R}}^{(2)}$ and $\chi_{NR}^{(2)}$, which are both complex number quantities and wavelength dependent ($\chi_{NR}^{(2)}$ is relatively constant within a narrow frequency range).[24,31] The ε and δ denote phase of $\chi_{\mathrm{R}}^{(2)}$ and $\chi_{NR}^{(2)}$, respectively.

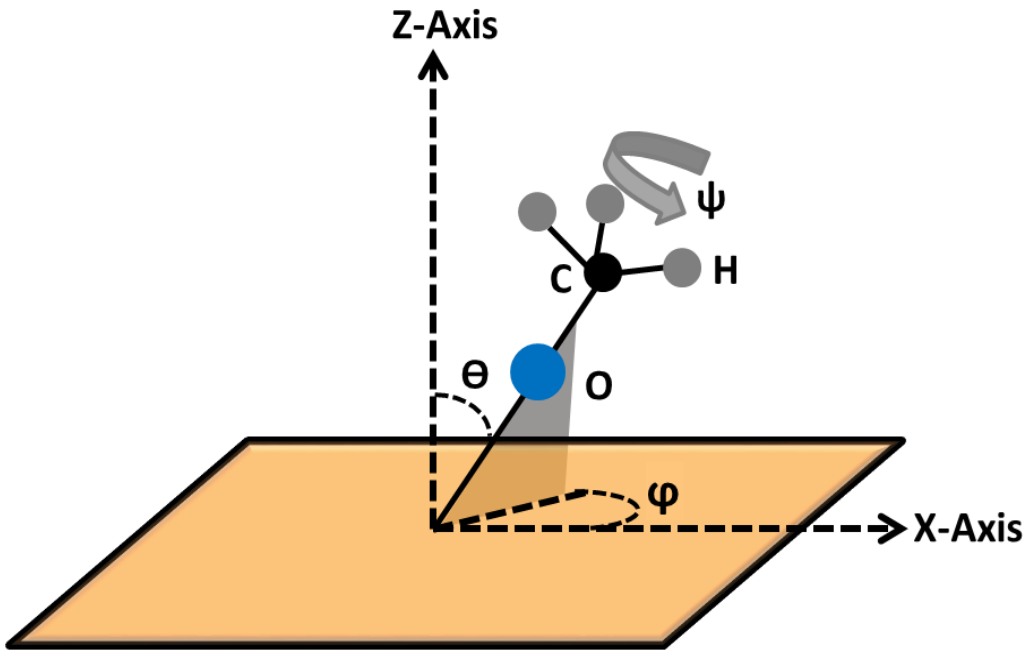

Figure 3-1. Definition of the tilt angle (Θ), azimuth angle (φ), and rotation angle (ψ) of the methoxy adsorbed on the copper surface.

The phase difference between $\chi_{\mathrm{R}}^{(2)}$ and $\chi_{NR}^{(2)}$ is named as relative non-resonant phase ϕ in Equation 2-12. Normally each vibration mode has the same relative phase ϕ. The SFG spectral line-shape transformation at different relative non-resonant phase (ϕ) are simulated in Figure A-1. The non-resonant phase and intensity vary dramatically on different metal surface, even with their corresponding metal oxides.[24,32] The sensitivity of SFG to substrate characteristic is highly advantageous for studying distinct molecular information as an effect of the metal surface properties.[32]

$$I_{SF} \propto \left|\chi_{eff}^{(2)}\right|^2 = \left|\chi_{NR}^{(2)}\right|^2 + \left|\chi_{R}^{(2)}\right|^2 + 2\left|\chi_{NR}^{(2)}\right|\left|\chi_{R}^{(2)}\right|\cos[\varepsilon - \delta] \qquad \textbf{Equation 3-2}$$

3.2.2. Sample preparation in the UHV chamber

Polycrystalline copper (Goodfellow, 99.99%) is used as the substrate material. These samples are rectangular with an area of 1 cm^2 and a thickness of 3 mm. The samples are polished down to 0.1 μm using diamond compound. The copper substrates are then mounted on a sample stage supported an x-y-z rotational manipulator housed in a stainless steel UHV chamber. The schematic diagram of the UHV system is shown in Figure 2-14. This UHV chamber is equipped with a turbo-molecular pump with a base pressure 1×10^{-9} Torr. A resistive tungsten filament situated at about 2 mm at rear of copper surface enables the control of surface temperature from 300 K to 800 K. Sample temperature measurement is carried out by a K-type thermocouple spot welded on the edge of the copper surface. The surface of the copper substrates are cleaned with several cycles of heating to 800 K and argon ion sputtering with beam energy of 3000 eV. Cleanliness of the metal surface is evaluated by a combination of TPD analysis of the methanol (CD_3OD) adsorption and the experimental SFG spectra obtained in CH stretching region (2750-3000 cm^{-1}). The efficiency of the cleaning procedure is assessed by the extinction of the methylene ($-CH_2-$) vibrational peaks at 2850 cm^{-1} in the SFG spectra (an example shown in Figure A-2) that arise from hydrocarbon contaminations. The UHV chamber is coupled to a quadruple mass spectrometer (QMS) (Extorr XT 200) to check the total chamber pressure and partial pressure of molecular fragments. The TPD experiments are carried out by heating the sample at a constant ramp rate (1K/s). Dosing is carried out by backfilling the chamber via a leak valve.

3.2.3. SFG imaging cell

The SFG imaging cell is connected to the vacuum chamber through a mechanical gate valve. The cell is equipped with CaF_2 and quartz windows for the corresponding beam input and output ports, respectively. The IR beam and 1064 nm pump beam go through the CaF_2 window on one side, while the SFG beam emits through the quartz window from opposite side. The sample stage is transferred from the main vacuum chamber into the SFG imaging cell using the manipulator. After detaching the sample stage from the manipulator, the gate valve is closed to keep the SFG cell isolated from the main chamber. The methanol (CD_3OD) vapor (1 Torr) is introduced into the SFG cell by opening of the needle valve between a glass vessel with SFG imaging cell. While being maintained in the glass vessel connected to the SFG imaging cell, CH_3OD (Cambridge Isotopes, 99.8%D) or CD_3OD (Cambridge Isotopes, 99%D) are purified through three cycles of: 1) distilling, 2) freezing, 3) thawing and 4) pumping.

3.2.4. SFG imaging setup description

SFG imaging setup was described in detail elsewhere.[22,33] The 1064 nm beam, serves as the pump beam for the SFG imaging, is generated by a picosecond pulsed Nd:YAG laser (EKSPLA PL2250) with a 20 Hz repetition rate. This picosecond laser also pumps the optical parametric generator/amplifier (OPG/OPA) to generate the IR beam, which is tunable within the 2000-4000 cm^{-1} frequency range. The 1064 nm beam and IR beam overlap temporally and spatially at incidence angles of 60° and 70°, respectively. Since the χ_{ZZZ} component dominates the SFG process on metal surfaces,[34] the

polarization combination named as PPP (the polarization of two incident beams is set to be parallel with the incidence plane, as well as the polarization of SFG beam) is chosen in this work. A reflection configuration is set up with an emission angle of SFG signal at about 62.1° with respect to the surface normal to collect the intermediated SFG beam profile. A Roper Scientific CCD camera with 1024×1024 pixel array is used for collecting the magnified SFG beam profile from the sample surface. Each SFG image is composed of 1024×1024 pixels and each pixel corresponds to about 1 μm distance on surface. The approximated spatial resolution for the SFG imaging is 2 μm.

3.3. Results and discussions

After dosing with 60 Langmuir of methanol (CH_3OD) at 300 K, the TPD results of the methanol (CH_3OD) desorption from the polycrystalline copper surface is evaluated at temperatures from 320 to 440 K. Figure 3-2 shows a TPD profile of the methanol (CH_3OD) desorption subjected to a heating rate of 1K/s. The chemical species observed in this study are identified by comparing the acquired fragment with those tabulated in the literature.[4,6,13,35] The broad CH_3OH peak (mass 31 and mass 32) occurs at 340 K. The missing peak of mass 33 indicates the methanol (CH_3OD) is desorbed as CH_3OH instead of CH_3OD. The formaldehyde peak (mass 29 and mass 30) at 350 K is much higher than the CH_3OH peak. That suggests that most methanol (CH_3OD) species dissociate on copper surface initially and the methoxy fragment is the most abundant and stable intermediate.

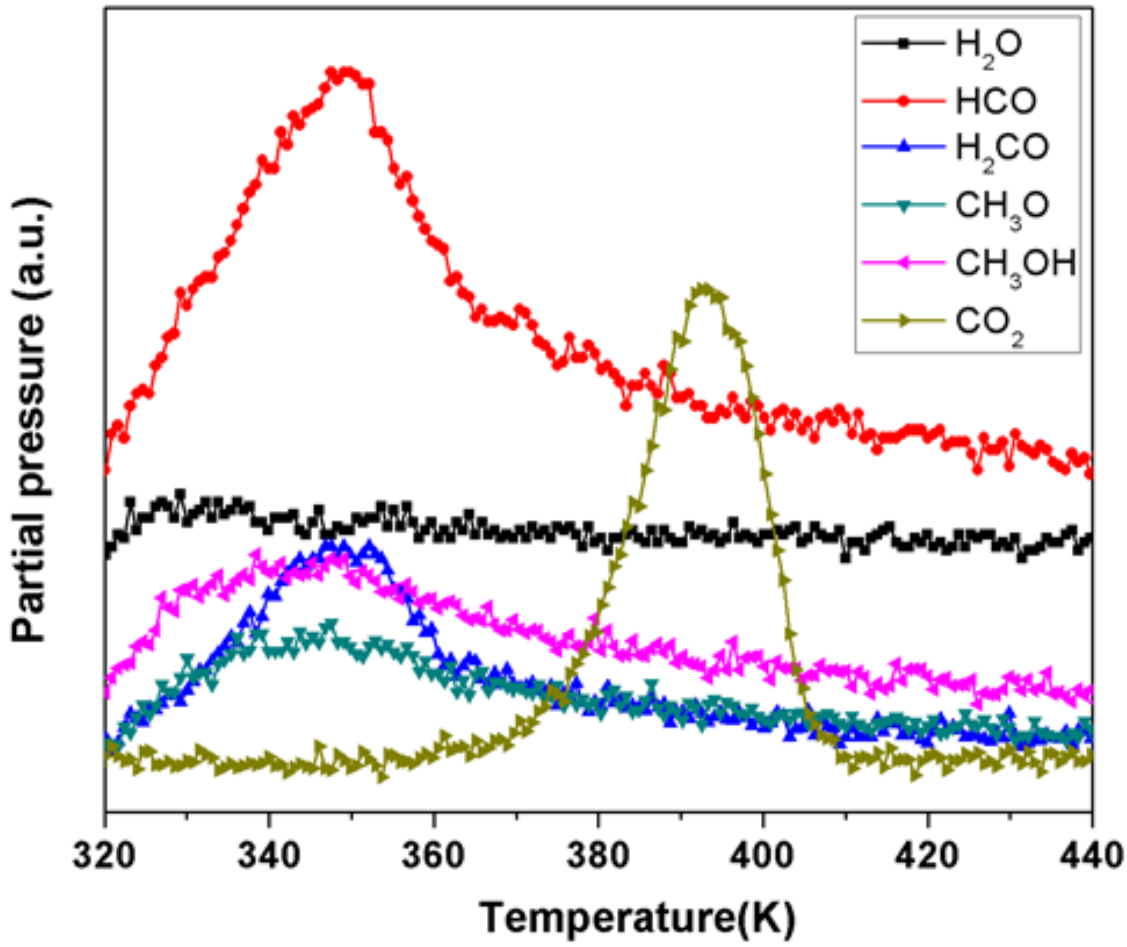

Figure 3-2. TPD profile from polycrystalline copper surface following 60 Langmuir methanol (CH_3OD) gas adsorption at 300 K. The masses correspond to the following desorption products: H_2O (mass 18), H_2CO (mass 28 and mass 29), CH_3OH (mass 31 and mass 32), CO_2 (mass 44). Heating rate was set at 1 K/s.

Formaldehyde is produced by the decomposition of the methoxy species when increasing the surface temperature of the copper surface.[13] The CO_2 peak (mass 44) evolves at 395 K. Wachs and Madix[6] concluded that the CO_2 peak on their TPD spectra is from a very stable formate intermediate. While Bowker and Madix[13] inferred that the earlier report[6] of the formate intermediate is due to formaldehyde contamination in the methanol. More recent works[4,35] clearly prove that the formate is produced during the methanol adsorption with

the presence of oxygen on the copper surface. These recent studies indeed suggest that the CO_2 peak originates from the formate intermediates.

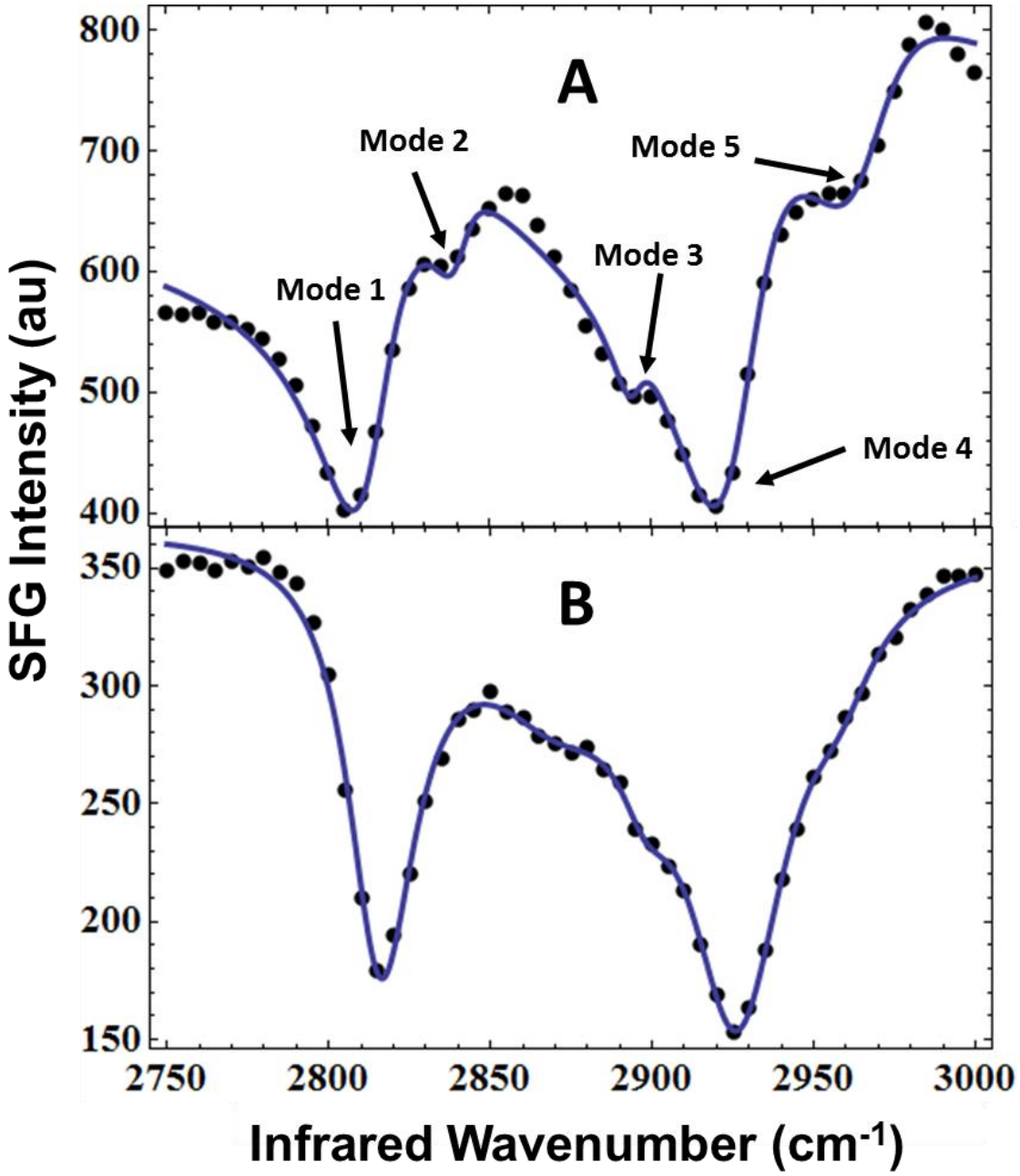

Figure 3-3. (A) The PPP-SFG spectrum of 1 Torr methanol (CH_3OD) adsorption on copper surface from 2750 cm^{-1} to 3000 cm^{-1}. (B) The PPP-SFG spectrum of 1 Torr methanol (CH_3OD) and 800 Torr oxygen adsorption on copper from 2750 cm^{-1} to 3000 cm^{-1}.

3.3.1. SFG spectroscopy and peak assignment

In situ SFG spectra (2750-3050 cm^{-1}) of methanol (CH_3OD) adsorption on copper surface are displayed in Figure 3-3. Two spectra in different gas exposure conditions are shown. The SFG spectrum in Figure 3-3A is obtained at room temperature from the copper substrate exposed to 1 Torr methanol (CH_3OD) vapor until equilibrium. The SFG spectrum in Figure 3-3B is recorded from the copper substrate exposed to 1 Torr methanol (CH_3OD) vapor and 800 Torr oxygen gas. There are five peaks (modes 1-5) which are located at 2812 cm^{-1}, 2860 cm^{-1}, 2890 cm^{-1}, 2925 cm^{-1}, and 2960 cm^{-1}, respectively.

Table 3-1: Fitting results of the SFG spectra sketched in Figure 3-3.

	copper surface with CH_3OD adsorption			copper oxide surface with CH_3OD adsorption		
	$\omega_q(cm^{-1})$	A_q(a.u.)	Γ_q (cm^{-1})	$\omega_q(cm^{-1})$	A_q(a.u.)	Γ_q (cm^{-1})
peak mode 1	2812	39	14	2813	73	12
peak mode 2	2853	34	42	2862	54	29
peak mode 3	2887	4	11	2894	12	11
peak mode 4	2926	69	21	2923	103	18
peak mode 5	2963	34	24	2956	17	16

Based on previous studies[2,6] and the TPD results in this work, methoxy is the most abundant species on the copper surface following methanol (CH_3OD) adsorption. Therefore, combined with previous assignments for SFG, HREELS, and IRAS results of methoxy on the copper surface,[3,7,9,36] the strong peak at 2810 cm^{-1} is unambiguously assigned to the methyl symmetric stretching mode of methoxy group. An early IRAS study[36] of methanol adsorbed on Cu(100) attributed the observation of three modes (2787, 2861, and 2901 cm^{-1}) in the IRAS spectra to methyl symmetric stretching mode and two

degenerate methyl asymmetric stretching modes, respectively. However, Chesters and McCash proposed that the two vibrational mode, in higher wavenumber range of C-H stretching region, were due to overtone and/or combination bands of the methyl deformation modes.[37] More recently, the studies performed by IRAS about methanol adsorption on a wide variety of copper surfaces listed in Table 3-2 make a good agreement with Chesters and McCash's work. According to IR selection rules, only the vibrational modes with component positioned along the surface normal could be observed by the IRAS. When the C-O axis is aligned along the surface normal, the asymmetric stretching mode is perpendicular to the surface normal and, therefore, expected not to appear in the IRAS spectra. Studies performed on Cu(110)[38] and Cu(111)[39] with X-ray absorption and backscattering photoelectron diffraction measurements demonstrated that the C-O axis is nearly perpendicular to the copper surface. The peak around 2887 cm^{-1} and 2925 cm^{-1} are the Fermi resonance of the symmetric stretching mode with the overtone ($2\delta_s$ and $2\delta_{as}$) of deformation mode of the methyl group, respectively. In this case, the mode 5 is assigned as the methyl asymmetric stretching mode (ν_{as}).

In Figure 3-3, there is a small peak located around 2853 cm^{-1}. Previous IRAS studies[2,4] demonstrate the existence of small amounts of formate species bound to the surface at room temperature with excess surface oxygen. The TPD results in Figure 3-2 support the existence of formate in this system. Thus that the mode 2 is assigned to ν(CH) of formate.[10]

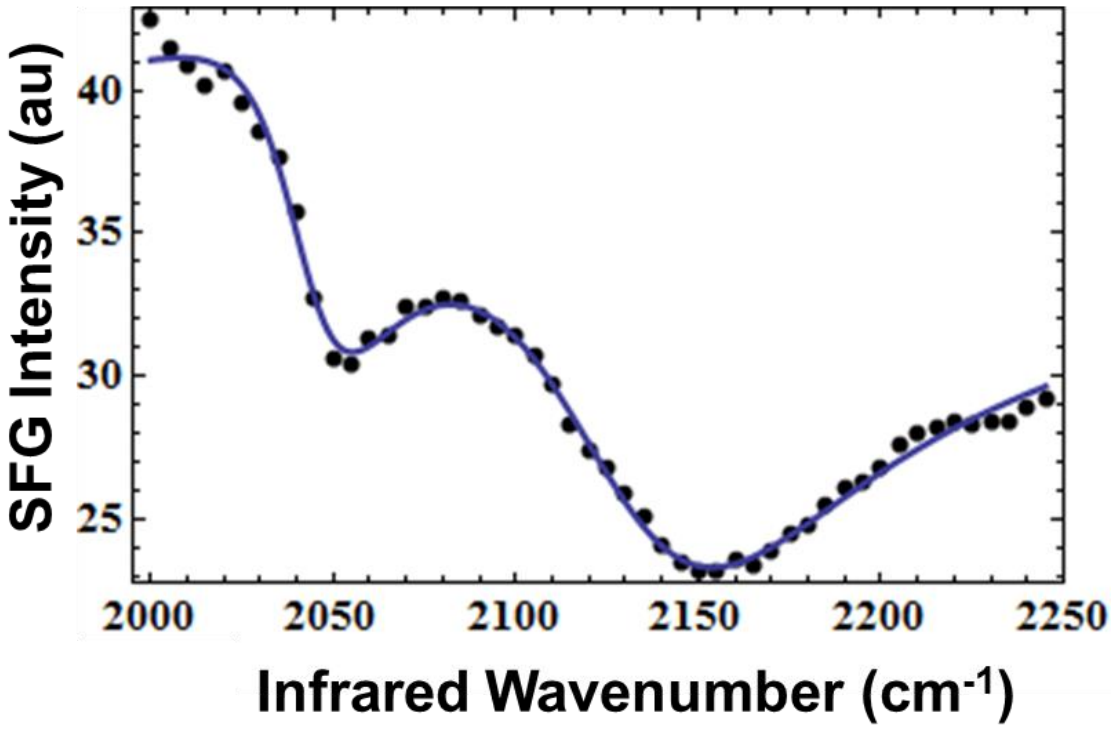

Figure 3-4. The PPP-SFG spectrum of 1 Torr methanol (CD_3OD) adsorption on copper surface from 2000 cm^{-1} to 2250 cm^{-1}.

Figure 3-4 shows the SFG spectrum (2000-2250 cm^{-1}) of methanol (CD_3OD) adsorption on copper surface which is obtained at room temperature with 1 Torr methanol (CD_3OD) vapor. The sharp peak located around 2044 cm^{-1} is assigned to the methyl symmetric stretching mode and the broad peak located at 2130 cm^{-1} is assigned as the Fermi resonance mode based on previous assignment listed in Table 3-4.[40] The SFG spectrum (2550-2700 cm^{-1}) are featureless and shown in Figure A-3. No OD stretching mode is observed which is consistent with previous IRAS studies.[36]

Table 3-2: Infrared vibrational mode assignments for methoxy on metal surface.

	Vibrational peak assignments				
	Cu(100)[36]	Cu(100)[40]	Cu(100)[41]	Cu(111)[42]	This work
Fermi-[$2\delta_{as}(CH_3)$]		2911	2917	2918	2926
Fermi-[$2\delta_{s}(CH_3)$]		2875	2879	2882	2887
$\nu_s(CH_3)$	2787	2798	2805	2818	2812
$\nu_{as}(CH_3)$	2861&2901				
$\delta s(CH_3)$			1426		
Fermi-[$2\delta_{as}(CD_3)$]		2171		2183	2130
Fermi-[$2\delta_{s}(CD_3)$]		2171		2183	2130
$\nu_s(CD_3)$	2054	2054		2050	2044
$\nu_{as}(CD_3)$	2127&2178				
$\delta_s(CD_3)$				1130	

Table 3-3: Fitting results of the SFG spectrum sketched in Figure 3-4.

	Pure copper with CD_3OD adsorption		
	$\omega_q(cm^{-1})$	A_q(a.u.)	Γ_q (cm^{-1})
Mode1	2044	16	19
Mode2	2130	67	52

3.3.2. Orientation calculation

The orientation and conformation of the terminal methyl group on copper surface is very important to understand the molecular packing properties of the adsorbed monolayer. Thus an orientation analysis based on SFG spectra is performed in this work based on the amplitude ratio of $CH_{3\text{-sym}}/CH_{3\text{-asym}}$ of SFG spectrum under the PPP polarization combination.[43-47] In this study, the methoxy group is approximately treated as C_{3v} symmetry. A δ function distribution is assumed for the tilt angle of methyl group. Isotropic distribution is assumed for the rotation angle and azimuthal angle of methyl

group, respectively. The C-H bond polarizability model and formulas from Hirose et al.[48] and Wang et al.[49] are used and shown in Equation 3-3 and Equation 3-4. Fresnel factors are calculated based on the model (shown in Equation 2-10) presented by Zhuang et al. to related the electrical field in local surface.[50,51] For methanol molecular, the R and β_{aca}/β_{ccc} are 1.67 and 1.0, respectively.[49,52,53]

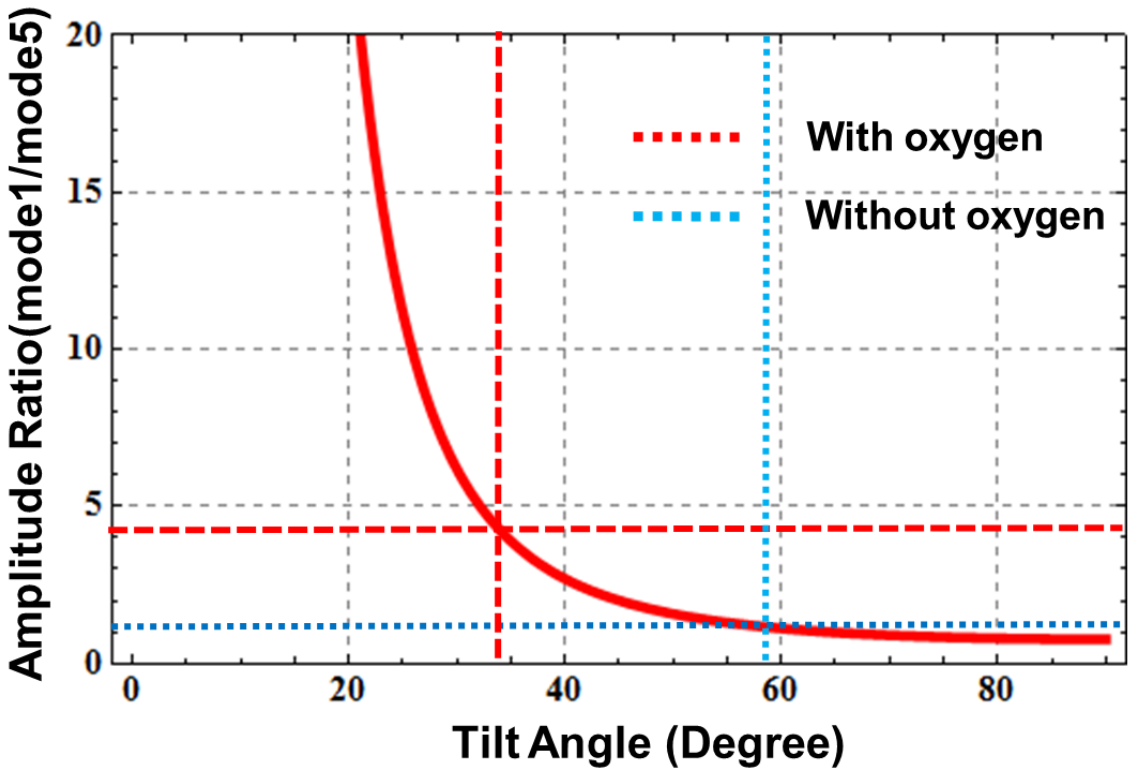

Figure 3-5. Orientation curve calculated by using the delta-function distribution approximation.

For C_{3v} symmetric stretching mode,

$$\chi^{(2)}_{xxz} = \chi^{(2)}_{yyz} = \frac{1}{2} N_s \beta_{ccc} [(1+R)\langle \cos\theta \rangle - (1-R)\langle \cos^3\theta \rangle]$$

$$\chi^{(2)}_{xzx} = \chi^{(2)}_{zxx} = \chi^{(2)}_{yzy} = \chi^{(2)}_{zyy} = \frac{1}{2} N_s \beta_{ccc} (1-R)[\langle \cos\theta \rangle - \langle \cos^3\theta \rangle] \qquad \textbf{Equation 3-3}$$

$$\chi^{(2)}_{zzz} = N_s \beta_{ccc} [R\langle \cos\theta \rangle + (1-R)\langle \cos^3\theta \rangle]$$

For C_{3v} asymmetric stretching mode,

$$\chi^{(2)}_{xxz} = \chi^{(2)}_{yyz} = -N_s\beta_{aca}[\langle\cos\theta\rangle - \langle\cos^3\theta\rangle]$$
$$\chi^{(2)}_{xzx} = \chi^{(2)}_{zxx} = \chi^{(2)}_{yzy} = \chi^{(2)}_{zyy} = N_s\beta_{aca}\langle\cos^3\theta\rangle \qquad \textbf{Equation 3-4}$$
$$\chi^{(2)}_{zzz} = 2N_s\beta_{aca}[\langle\cos\theta\rangle - \langle\cos^3\theta\rangle]$$

The tilt angle, azimuth angle and rotation angle reference to surface normal and C_3 axis, are demonstrated in Figure 3-1. Based on the assumption that the tilt angle distribution of methoxy follows a δ function and the rotation angle together with azimuth angle are randomly distributed, a theoretical curve simulating the amplitude ratio of $CH_{3\text{-}sym}/CH_{3\text{-}asym}$ as a function of the tilt angle of methyl groups is presented in the Figure 3-5. In terms of fitting results and theoretical simulation curves, the tilt angle (Θ) of methyl group is around 59±7° for copper without oxygen exposure, and 34±3° for copper with oxygen exposure.

The tilt angle of methoxy group on copper oxide surface is smaller than on pure copper surface might suggest that the methoxy group is more densely packed on oxidized copper. Previous studies demonstrated that oxygen promotes the methanol dissociation and increases the surface density of the methoxy monolayer on copper surface.[2,6-8] Thus, higher density and smaller tilt angle of methoxy increase the cross section of methyl symmetric stretching mode on copper oxide surface relative to the pure copper surface.

3.3.3. Spatial mapping and orientation distribution analysis

By fitting the SFG spectra in Figure 3-3 based on the Equation 3-3, the non-resonant background and non-resonant relative phase results are listed in Table 3-4. The intensity of

non-resonant background of copper oxide is lower than the pure copper. The relative phase also changes after the introduction of oxygen. Previous studies indicate that the non-resonant background has a direct relationship with surface electronic properties of the metal substrate.[10,31,34,54]

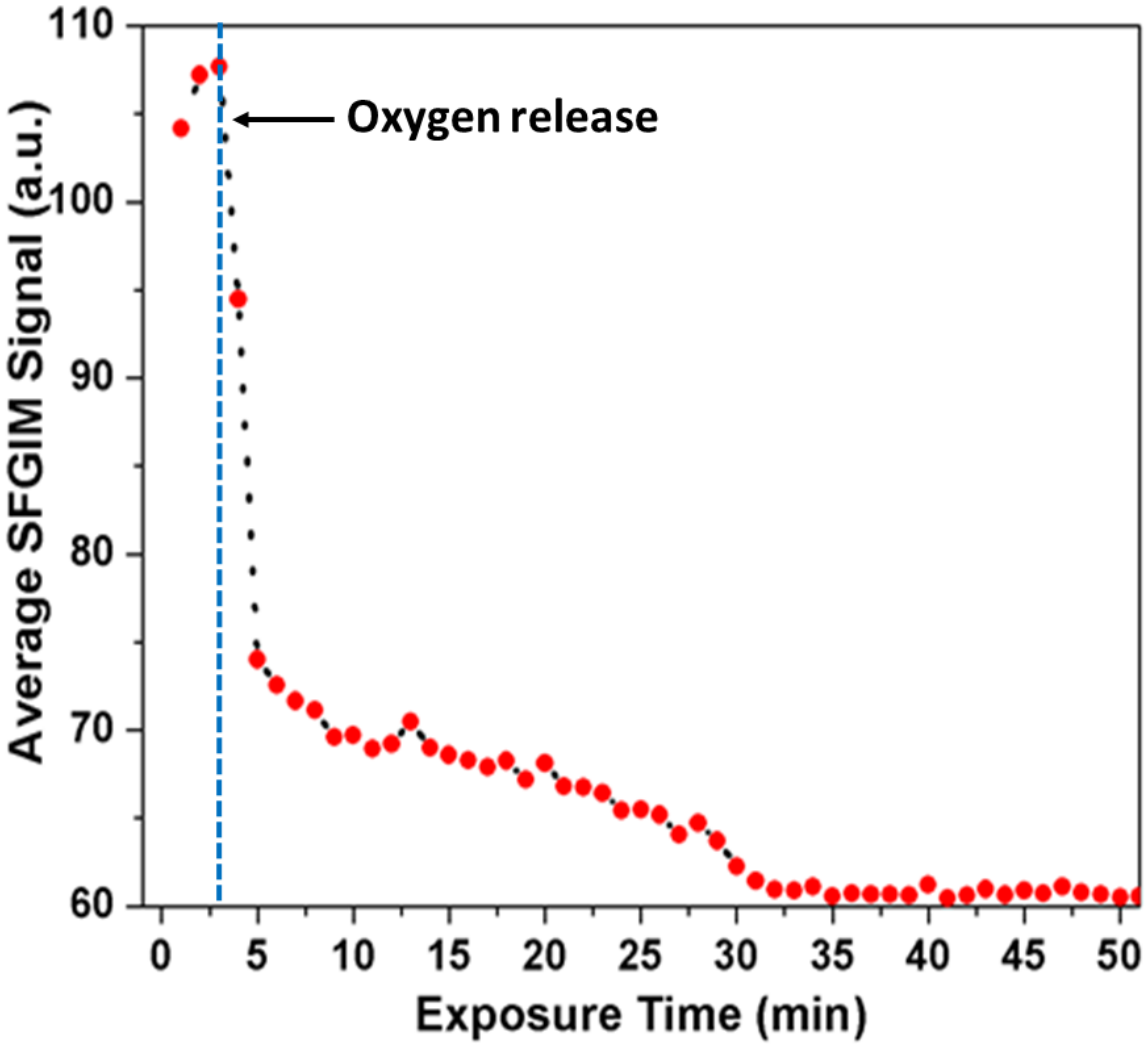

Figure 3-6. SFG non-resonant background intensity (3000 cm^{-1}) changed as oxygen exposure time (800 Torr oxygen is released at the third minute)

Table 3-4. Non-resonant background and phase of copper and copper oxide.

	Non-resonant intensity(a.u.)	Non-resonant phase-ϕ (rad)
Pure copper	26.7	-2.75
Copper oxide	19.6	-1.56

The exposure of oxygen gas to pure copper would introduce the formation of copper oxide on surface,[55] which changes the surface electronic properties and non-resonant response.[54,56] The SFG signal (IR wavenumber: 3000 cm^{-1}) correlates with oxygen introduction time. This effect is demonstrated more clearly in Figure 3-6. Since 3000 cm^{-1} is far from vibrational resonant region of methyl group, the SFG signal can be regarded as the contribution of non-resonant response from the substrate. Upon exposure with 800 Torr oxygen gas, the SFG intensity (3000 cm^{-1}) quickly drops in the first 5 mins, then gradually decreases to a signal level which is half of the initial intensity. After half an hour, the SFG intensity remains stable. This observation is comparable with previous SHG studies of oxidation of Cu(111).[54]

From Equation 2-12, the relative phase ϕ results from interaction between the substrate and top methoxy monolayer, as evidenced by constructive or destructive interference between adjacent peaks as well as with the non-resonant background, causes spectral lineshape shifts as the relative phase changes. Recently, Hosseinpour et al.'s work reported that oxidation of the copper substrate significantly changes the SFG spectral line shape of alkanethiol SAMs on copper.[32] Santos et al. showed two-dimensional line-shape transformation of alkanethiol SAMs on copper surface using SFG imaging.[57] Comparison of SFG spectra in Figure 3-3 indicates an alteration of the spectral line-shape with oxygen exposure. The phase parameters shown in Table 3-5 also denote the non-resonant phase

shift from -2.75 rad to -1.56 rad. These transformations of spectral features including the relative phase, non-resonant background, and spectral line-shape reveal the high sensitivity of SFG signal to chemical changes on the metal surface.

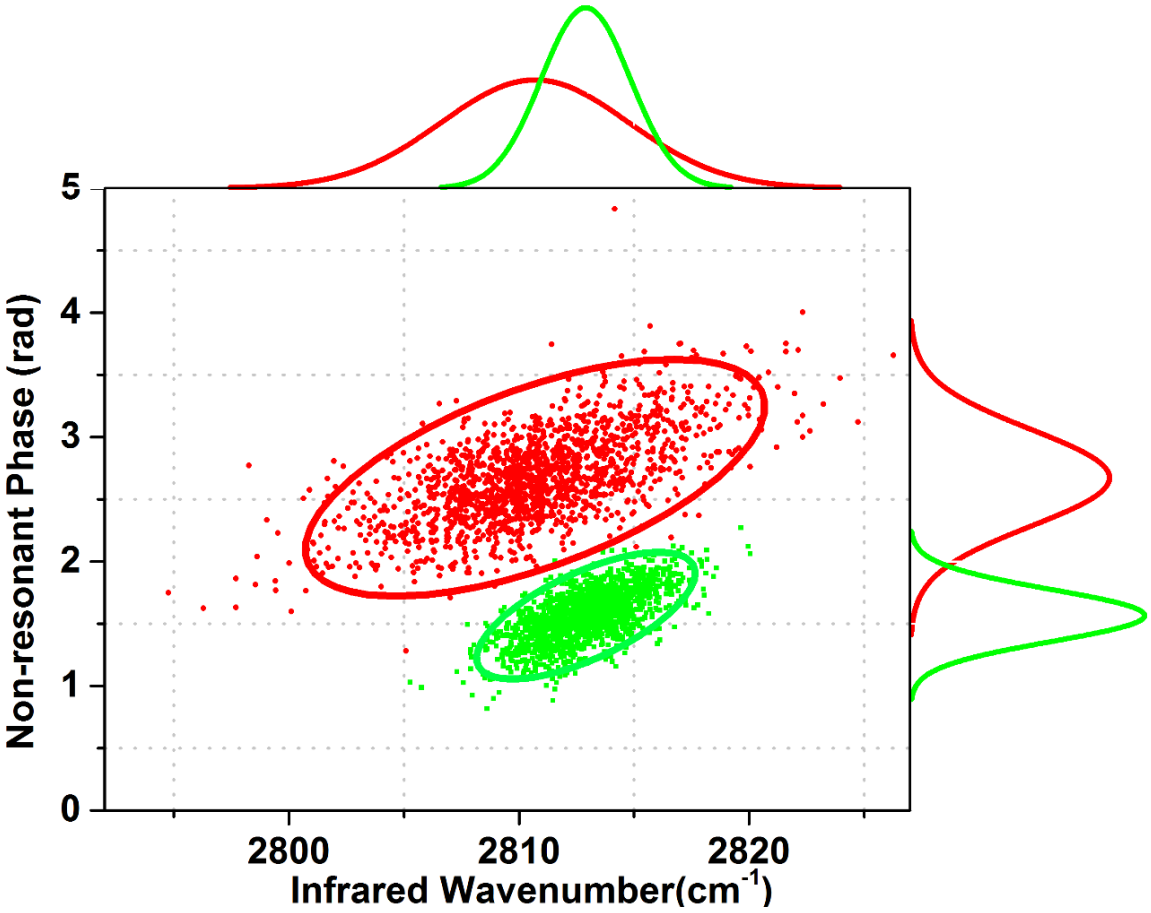

Figure 3-7. Scatter/marginal histogram plot of non-resonant phase vs $CH_{3\text{-sym}}$ resonant frequency (red data scatter points in red ellipse, as well as the red histogram line are for copper without oxygen; green data scatter points in green ellipse, as well as green histogram line are for copper with oxygen).

The stack of SFG images is divided into 40 × 40 regions of interest (ROI) which is a 15 μm × 15 μm square. The SFG spectra are extracted and fitted by Equation 3-2. The fitting parameters including amplitude, non-resonant phase, resonant frequency and ratios of methyl symmetric stretching mode and methyl asymmetric stretching mode in each ROI

are obtained and then used in the following statistics analysis. A δ function distribution is employed to analyze each ROI.

In Figure 3-7, a scatter plot, as well as a marginal histogram, is constructed to correlate two spectral features: non-resonant phase vs $CH_{3\text{-sym}}$ resonant frequency. The x-axis value and y-axis value of each date point correspond to $CH_{3\text{-sym}}$ resonant frequency and non-resonant phase of a special ROI, respectively. The decrease in the distribution width of non-resonant phase and $CH_{3\text{-sym}}$ resonant frequency after introduction of oxygen suggests that heterogeneity of copper surface and methoxy monolayer decreases with the formation of copper oxide. Such a change could be related to the existence of various size of crystal domain with different surface atom structure on polycrystalline copper surface.[58-64] The formation of copper oxide generates a more homogenous surface atom structure arrangement, which narrows heterogeneity between different ROI.

In addition, there is a blue shift for the resonant wavenumber of $CH_{3\text{-sym}}$ concurrent with an overall increase in the non-resonant phase. The resonant frequency of $CH_{3\text{-sym}}$ stretching mode in the ROI with a higher non-resonant phase is higher than the ROI with a lower non-resonant phase. Known to be affected by the local surface structure of copper, the non-resonant phase could be spatially correlated with local bonding strength of methoxy. Such a relationship can be linked to the effects of various index crystal facets with the different binding energy of methoxy group. Similar phenomena were reported by Ertl *et al.* where different CO oxidation behavior are observed on the individual grains of the polycrystalline platinum surface.[65,66] More recently, Salmeron *et al.* reported that the reaction rate difference of CO with chemisorbed oxygen on three low-index faces of copper

resulted from different binding energy of oxygen.[67] Such mechanism of this phenomenon in this work need to be further explored to build an intrinsic correlation between copper surface structures with binding energy of methoxy group. However, this addresses the unique advantage of SFG imaging in elucidating the relationship between the monolayer properties with local copper surface structure.

3.3.4. Spatial maps of conformation and orientation of methoxy on copper surface

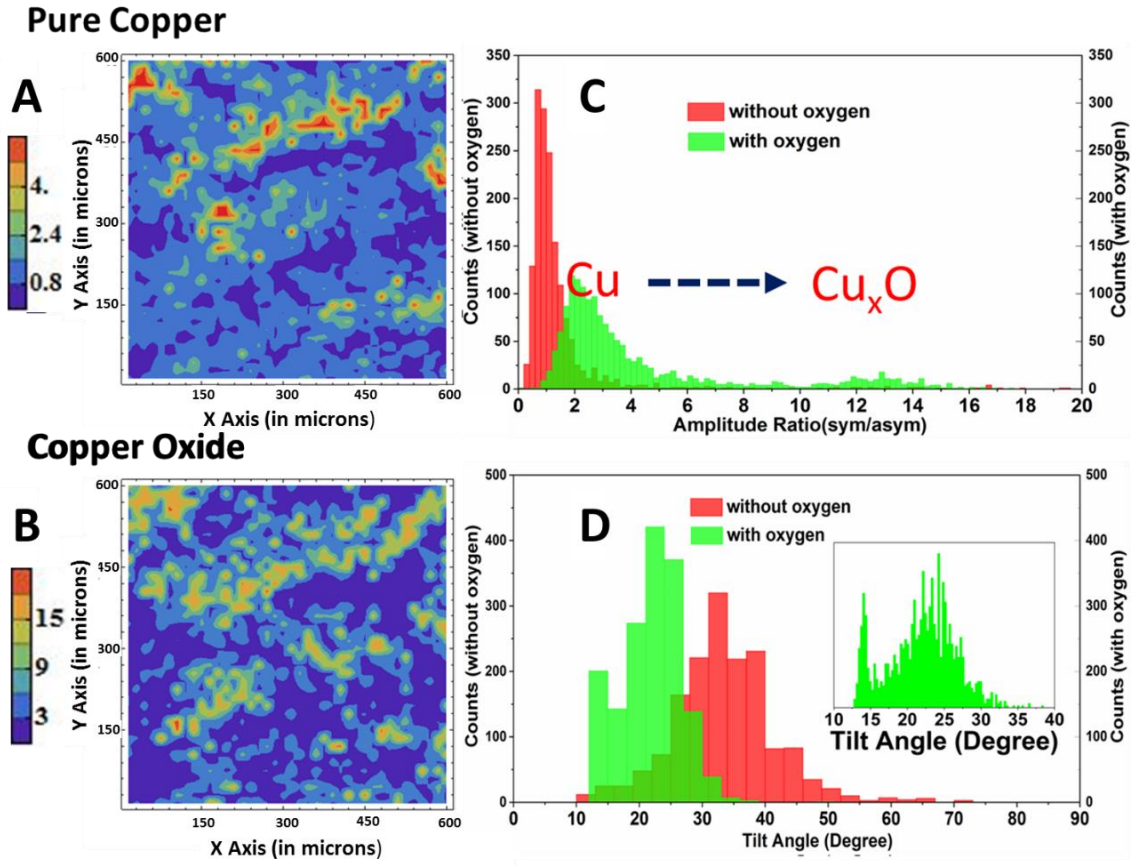

Figure 3-8. Contour maps of amplitude ratios of methoxy ($CH_{3\text{-}sym}/CH_{3\text{-}asym}$) on copper (A) without and (B) with oxygen, respectively. Histogram of (C) amplitude ratios ($CH_{3\text{-}sym}/CH_{3\text{-}asym}$) and (D) calculated tilt angle of methoxy on copper with (green) and without (red) oxygen, respectively.

To elucidate the role of oxygen in methoxy heterogeneity, the evaluation of SFG imaging data from methanol (CD_3OD) adsorption on copper with and without oxygen exposure is carried out by employing statistical methods represented in the form of spatial (contour maps) and histogram distributions. In Figure 3-8A and Figure 3-8B, the fitted results of the amplitude ratio ($CH_{3\text{-}sym}/CH_{3\text{-}asym}$) is mapped onto the surface coordinates to visualize differences in spatial distribution for the copper surface with and without oxygen exposure. Inspection of the histogram of amplitude ratio in Figure 3-8C, the initial ratio ($CH_{3\text{-}sym}/CH_{3\text{-}asym}$) is narrowly distributed in the 0-4 range. After the introduction of oxygen, the ratio distribution range increased up to 20 resulting to a wider bimodal distribution.

It is suggested that the metal surface contains defects such as grain boundaries and/or phase inclusions which dramatically influence localized metal activity and, also, molecules adsorption at or near these sites.[57,68-70] In considering defects, the oxidation process is not simultaneous and homogenous between different ROIs. Table 3-5 shows that the average ratio ($CH_{3\text{-}sym}/CH_{3\text{-}asym}$) is lower for pure copper surface compared to copper oxide. The ratio ($CH_{3\text{-}sym}/CH_{3\text{-}asym}$) is higher in the ROIs which are heavily oxidized compared to the lightly oxidized ROIs. Thus, in Figure 3-8C, the extra broad peak of the histogram at higher ratio values corresponds to the ROIs that copper surface that are oxidized. While the main histogram peak centered at ~ 3 is attributed from ROIs in which the copper surface still remains metallic, the middle range of amplitude ratios between two peaks are linked to ROIs where the copper surface is partially oxidized.

The histogram of tilt angles in Figure 3-8D clearly demonstrates that methoxy group on copper oxide surface statistically lies more upright. The width of tilt angle

distribution, a measure of the degree of monolayer order, suggests a more densely packed methoxy film with less monolayer defect following of oxidation. Since oxygen promotes the methanol dissociation and increases the surface density of the methoxy monolayer on copper surface,[2,6-8] it could be inferred that higher surface density of molecules induces a compact monolayer with less monolayer defect, as well as a narrow distribution of tilt angle.

It is interesting to note that the distribution width of the ratio ($CH_{3\text{-}sym}/CH_{3\text{-}asym}$) sketched in Figure 3-8 and Table 3-5 increases after the oxygen exposure. Intuitively, oxygen exposure narrows the tilt angle distribution of the methoxy group, and then also narrows the distribution of ratio ($CH_{3\text{-}sym}/CH_{3\text{-}asym}$). However, it has to be noted that at higher values of the methyl (sym/asym) amplitude ratio, the range of possible angles is narrower based on simulation curve shown in Figure 3-5. Therefore evaluating the orientation distribution based on the simple comparison of the distribution width of the ratio ($CH_{3\text{-}sym}/CH_{3\text{-}asym}$) is not accurate. These statistical analysis address that SFG imaging improves the understanding of role of oxygen in methanol adsorption on copper surface by analyzing each ROI separately.

Table 3-5. Statistical parameters of distributions of the methyl (sym/asym) ratio and terminal methyl group tilt angle (degree)

	Methyl (sym/asym) Ratio		Methyl group tilt angle (degree)	
	Mean	Distribution width(σ)	Mean	Distribution width(σ)
Pure Copper	1.8	3.0	65	21
Copper Oxide	6.6	4.5	34	12

3.4. Conclusions

This work demonstrates the high sensitivity of SFG imaging in evaluating the quality and structure of monolayer film, as well as spatially correlating the local substrate with the top monolayer performance. At first, the spontaneous methanol dissociation and methoxy monolayer formation at room temperature is observed on copper surface. Comparison of SFG spectra elucidates oxygen exposure decrease the tilt angle of methoxy monolayer which is closer to the surface normal. Statistical analysis of SFG images suggests a well ordered methoxy monolayer with less defects following the oxygen exposure. Spatial correlation between non-resonant phases with resonant frequency of methoxy symmetric stretching mode demonstrate the potential of SFG imaging to correlate the local substrate to molecular behavior of top methoxy monolayer. This study provides a new clue for the future research of heterogeneous catalysis system as well as understanding metal surface in the molecular level.

3.5. References:

(1) Satterfield, C. N. *Heterogeneous catalysis in practice*; McGraw-Hill Companies, **1980**.

(2) Sim, W.; Gardner, P.; King, D. *J. Phys. Chem.* **1995**, *99*, 16002.

(3) Camplin, J.; McCash, E. *Surf. Sci.* **1996**, *360*, 229.

(4) Mudalige, K.; Trenary, M. *Surf. Sci.* **2002**, *504*, 208.

(5) Yoshihara, J.; Parker, S.; Schafer, A.; Campbell, C. T. *Catal. Lett.* **1995**, *31*, 313.

(6) Wachs, I. E.; Madix, R. J. *J. Catal.* **1978**, *53*, 208.

(7) Sexton, B. A. *Surf. Sci.* **1979**, *88*, 299.

(8) Russell Jr, J.; Gates, S. M.; Yates Jr, J. *Surf. Sci.* **1985**, *163*, 516.

(9) Mudalige, K.; Trenary, M. *J. Phys. Chem. B* **2001**, *105*, 3823.

(10) Lin, S.; Oldfield, A.; Klenerman, D. *Surf. Sci.* **2000**, *464*, 1.

(11) Jiang, X.; Parmeter, J. E.; Estrada, C. A.; Goodman, D. W. *Surf. Sci.* **1991**, *249*, 44.

(12) Fu, S. S.; Somorjai, G. A. *J. Phys. Chem.* **1992**, *96*, 4542.

(13) Bowker, M.; Madix, R. J. *Surf. Sci.* **1980**, *95*, 190.

(14) Härle, H.; Lehnert, A.; Metka, U.; Volpp, H.-R.; Willms, L.; Wolfrum, J. *Chem. Phys. Lett.* **1998**, *293*, 26.

(15) Somorjai, G. A.; Rupprechter, G. *J. Phys. Chem. B* **1999**, *103*, 1623.

(16) Pérez León, C.; Sürgers, C.; v. Löhneysen, H. *Phys. Rev. B* **2012**, *85*, 035434.

(17) Kim, Y. G.; Baricuatro, J. H.; Javier, A.; Gregoire, J. M.; Soriaga, M. P. *Langmuir* **2014**, *30*, 15053.

(18) Su, X. C.; Cremer, P. S.; Shen, Y. R.; Somorjai, G. A. *J. Am. Chem. Soc.* **1997**, *119*, 3994.

(19) Cremer, P. S.; Su, X. C.; Shen, Y. R.; Somorjai, G. A. *J. Am. Chem. Soc.* **1996**, *118*, 2942.

(20) Wang, C. Y.; Groenzin, H.; Shultz, M. J. *Langmuir* **2003**, *19*, 7330.

(21) Feng, R.-r.; Liu, A.-a.; Liu, S.; Shi, J.; Zhang, R.; Ren, Z. *J. Phys. Chem. C* **2015**, *119*, 9798.

(22) Cimatu, K.; Baldelli, S. *J. Phys. Chem. B* **2006**, *110*, 1807.

(23) Jang, J. H.; Jacob, J.; Santos, G.; Lee, T. R.; Baldelli, S. *J. Phys. Chem. C* **2013**, *117*, 15192.

(24) Bain, C. D. *J. Chem. Soc. Faraday Trans.* **1995**, *91*, 1281.

(25) Shen, Y. R. *Nature* **1989**, *337*, 519.

(26) Buck, M.; Himmelhaus, M. *J. Vac. Sci. Technol. A* **2001**, *19*, 2717.

(27) Santos, G.; Baldelli, S. *J. Phys. Chem. C* **2012**, *116*, 25874.

(28) Lambert, A. G.; Davies, P. B.; Neivandt, D. J. *Appl. Spectrosc. Rev.* **2005**, *40*, 103.

(29) Buck, M.; Himmelhaus, M. *J. Vac. Sci. Technol. A-Vac. Surf. Films* **2001**, *19*, 2717.

(30) Shen, Y. R. *Nature* **1989**, *337*, 519.

(31) Harris, A. L.; Chidsey, C. E. D.; Levinos, N. J.; Loiacono, D. N. *Chem. Phys. Lett.* **1987**, *141*, 350.

(32) Hosseinpour, S.; Hedberg, J.; Baldelli, S.; Leygraf, C.; Johnson, M. *J. Phys. Chem. C* **2011**, *115*, 23871.

(33) Fang, M.; Baldelli, S. *J. Phys. Chem. Lett.* **2015**, *6*, 1454.

(34) Superfine, R.; Guyotsionnest, P.; Hunt, J. H.; Kao, C. T.; Shen, Y. R. *Surf. Sci.* **1988**, *200*, L445.

(35) Davies, P. R.; Mariotti, G. G. *J. Phys. Chem.* **1996**, *100*, 19975.

(36) Ryberg, R. *Phys. Rev. B* **1985**, *31*, 2545.

(37) Chesters, M. A.; McCash, E. M. *Spectrochim. Acta A* **1987**, *43*, 1625.

(38) Lindner, T.; Somers, J.; Bradshaw, A.; Kilcoyne, A.; Woodruff, D. *Surf. Sci.* **1988**, *203*, 333.

(39) Witko, M.; Hermann, K.; Ricken, D.; Stenzel, W.; Conrad, H.; Bradshaw, A. *Chem. Phys.* **1993**, *177*, 363.

(40) Mudalige, K.; Warren, S.; Trenary, M. *J. Phys. Chem. B* **2000**, *104*, 2448.

(41) Asmundsson, R.; Uvdal, P. *J. Chem. Phys.* **2000**, *112*, 366.

(42) Chesters, M. A.; McCash, E. M. *Spectrochim. Acta Mol. Biomol. Spectrosc.* **1987**, *43*, 1625.

(43) Hirose, C.; Yamamoto, H.; Akamatsu, N.; Domen, K. *J. Phys. Chem.* **1993**, *97*, 10064.

(44) Wang, H. F.; Gan, W.; Lu, R.; Rao, Y.; Wu, B. H. *Int. Rev. Phys. Chem.* **2005**, *24*, 191.

(45) Guo, Z.; Zheng, W.; Hamoudi, H.; Dablemont, C.; Esaulov, V. A.; Bourguignon, B. *Surf. Sci.* **2008**, *602*, 3551.

(46) Cecchet, F.; Lis, D.; Guthmuller, J.; Champagne, B.; Caudano, Y.; Silien, C.; Mani, A. A.; Thiry, P. A.; Peremans, A. *Chemphyschem* **2010**, *11*, 607.

(47) Zhang, H. P.; Romero, C.; Baldelli, S. *J. Phys. Chem. B* **2005**, *109*, 15520.

(48) Hirose, C.; Yamamoto, H.; Akamatsu, N.; Domen, K. *J. Phys. Chem* **1993**, *97*, 10064.

(49) Wang, H. F.; Gan, W.; Lu, R.; Rao, Y.; Wu, B. H. *Int. Rev. Phys. Chem.* **2005**, *24*, 191.

(50) Zhuang, X.; Miranda, P.; Kim, D.; Shen, Y. *Phys. Rev. B* **1999**, *59*, 12632.

(51) Lambert, A. G.; Davies, P. B.; Neivandt, D. J. *Appl. Spectrosc. Rev.* **2005**, *40*, 103.

(52) Ishiyama, T.; Sokolov, V. V.; Morita, A. *J. Chem. Phys.* **2011**, *134*, 024509.

(53) Ishiyama, T.; Sokolov, V. V.; Morita, A. *J. Chem. Phys.* **2011**, *134*, 024510.

(54) Bloch, J.; Bottomley, D. J.; Janz, S.; Vandriel, H. M. *Surf. Sci.* **1991**, *257*, 328.

(55) Aastrup, T.; Wadsak, M.; Schreiner, M.; Leygraf, C. *Corros. Sci.* **2000**, *42*, 957.

(56) Tom, H. W. K.; Mate, C. M.; Zhu, X. D.; Crowell, J. E.; Heinz, T. F.; Somorjai, G. A.; Shen, Y. R. *Phys. Rev. Lett.* **1984**, *52*, 348.

(57) Santos, G. M.; Baldelli, S. *J. Phys. Chem. C* **2013**, *117*, 17591.

(58) Martinez-Lombardia, E.; Maurice, V.; Lapeire, L.; De Graeve, I.; Verbeken, K.; Kestens, L.; Marcus, P.; Terryn, H. *J. Phys. Chem. C* **2014**, *118*, 25421.

(59) Lapeire, L.; Martinez Lombardia, E.; Verbeken, K.; De Graeve, I.; Kestens, L. A. I.; Terryn, H. *Corros. Sci.* **2013**, *67*, 179.

(60) Park, C. J.; Lohrengel, M. M.; Hamelmann, T.; Pilaski, M.; Kwon, H. S. *Electrochim. Acta* **2002**, *47*, 3395.

(61) Martinez-Lombardia, E.; Lapeire, L.; Maurice, V.; De Graeve, I.; Verbeken, K.; Klein, L. H.; Kestens, L. A. I.; Marcus, P.; Terryn, H. *Electrochem. Commun.* **2014**, *41*, 1.

(62) Martinez-Lombardia, E.; Gonzalez-Garcia, Y.; Lapeire, L.; De Graeve, I.; Verbeken, K.; Kestens, L.; Mol, J. M. C.; Terryn, H. *Electrochim. Acta* **2014**, *116*, 89.

(63) Schreiber, A.; Schultze, J. W.; Lohrengel, M. M.; Karman, F.; Kalman, E. *Electrochim. Acta* **2006**, *51*, 2625.

(64) Lill, K. A.; Hassel, A. W.; Frommeyer, G.; Stratmann, M. *Electrochim. Acta* **2005**, *51*, 978.

(65) Ertl, G. *Science* **1991**, *254*, 1750.

(66) Lauterbach, J.; Haas, G.; Rotermund, H.; Ertl, G. *Surf. Sci.* **1993**, *294*, 116.

(67) Eren, B.; Lichtenstein, L.; Wu, C. H.; Bluhm, H.; Somorjai, G. A.; Salmeron, M. *J. Phys. Chem. C* **2015**, *119*, 14669.

(68) Jones, D. A. *Principles and prevention of corrosion*; Macmillan, **1992**.

(69) Roberge, P. R. *Corrosion engineering: principles and practice*; McGraw-Hill New York, **2008**.

(70) Cimatu, K.; Baldelli, S. *J. Phys. Chem. C* **2007**, *111*, 7137.

CHAPTER 4. Grain Structures and Boundaries on Microcrystalline Copper Covered with an Octadecanethiol Monolayer Revealed by Sum Frequency Generation Microscopy*

4.1. Introduction

The mechanism of metallic corrosion and inhibition has been the subject of a vast amount of research due to its significance to the modern world.[1] Previous corrosion studies have often been performed on the macroscopic scale, but corrosion behavior also strongly depends on microscopic features i.e., crystal grains with different crystallographic orientations, which exist on most polycrystalline metallic surfaces.[2,3] Recent studies demonstrated that the pattern differences across microscopic crystal grains and grain boundaries (GBs) induce the localized corrosion on the copper surface.[4-6] Features, such as surface current difference across grains,[7,8] extensive mis-orientation between grains[9], and grain sizes[10,11] contribute to heterogeneous corrosion occurring on the surfaces. Due to the existence of heterogeneous corrosion at the micrometer scale, understanding the role of crystallographic orientation to local corrosion process is worthwhile goal. Therefore, high-resolution imaging techniques are necessary. There have been numerous studies reported to investigate the role of crystallographic orientation and GBs on metal corrosion occurring in the initial stages, including studies performed using Electron Backscattering Diffraction (EBSD)[3], Atomic Force Microscopy (AFM)[3] and Scanning Tunneling Microscopy (STM)[5], which are able to provide highly accurate topographic information of surface and structure

*Reproduced in part with permission from *J. Phys. Chem. Lett.* **2015**, 6, 1454, ©2015 American Chemical Society

of the corrosion site. Under some circumstance, scanning probe microscopy such as AFM and STM could deduce the surface molecular functional group and packing geometry with atomic resolution.[12-17] However, local chemical information obtained from vibrational spectroscopy of molecular functionality on the surface, which is important to interpret and understand local copper corrosion and inhibition behaviors, is still lacking.

Alkanethiol self-assembled monolayers (SAMs) on metal surfaces have been extensively studied due to their identical surface chemical functionality, excellent stability, and wide application such as improving corrosion resistance for copper surfaces.[18-22] One popular technique for studying the alkanethiol monolayer on the surface at a molecular level is Sum Frequency Generation Vibrational Spectroscopy (SFG-VS), which has excellent chemical selectivity and interfacial sensitivity. Previous SFG-VS studies have been applied to characterize the ordered monolayer of alkanethiols formed on copper surfaces.[23] Recently, Hosseinpour *et. al.* employed SFG-VS to monitor the oxidation of ODT-covered copper in dry air and observed the formation of a thin layer of copper (I) oxide beneath the ODT monolayer based on the phase change of SFG spectra.[19] In addition, they also applied SFG-VS to study the chain length effect of alkanethiols by analyzing corrosion behaviors induced by formic acid on copper and found the inhibition ability increasing continuously with chain length. However, these SFG studies focused on average spectral analysis without providing any local information about the surface. In recent studies, the SFG imaging technique which combines SFG-VS with a microscope probe, demonstrated high spatial resolution combined with SFG local spectra to study monolayers on a heterogeneous metal surface.[24-26] Santos *et. al*. performed SFG imaging to study localized corrosion processes occurring on copper surfaces in an oxygenated environment

by monitoring Cu_2O formation.[24] However, the important metallic features including the crystal grains and GBs have not been observed and interpreted by the SFG imaging technique.

It has been proven that micrometer-sized crystal grains and GB structures form on copper surfaces when annealed at high temperature in a hydrogen atmosphere.[27] In this study, SFG imaging was used to investigate ODT monolayers on this type of copper surface. Micrometer-sized copper grains and GBs were clearly observed in the SFG image. Compared to traditional diffraction tools used for the crystallographic research, the SFG technique that offers several unique features, including non-invasivity and versus bulk surface selectivity, has already been developed for probing various crystal surfaces.[28] Characteristic anisotropy of the SFG signal response in each grain suggests SFG performed in microscopy mode shows high promise for imaging the local metal surface symmetry with high spatial resolution. In addition, the corresponding local spectra demonstrate the advantage of SFG imaging in providing sufficient molecular information on heterogeneous metal surfaces. As a result, it shows the promising application for the research of corrosion behavior on microcrystalline metal surfaces.

4.2. Theory background

A relevant equations of SFG spectroscopy is hereby briefly presented here. SFG is a second-order nonlinear optical process.[29] And its intensity is directly proportional to the square of the two incident light fields (1064 nm and IR) shown in Equation 4-1. Here, E_{1064nm} and E_{IR} are the electric fields of 1064 nm beam and IR incident light, respectively.

$\chi_{eff}^{(2)}$ is a third-rank tensor, which contains tensorial Fresnel factors at the interface and macroscopic second-order nonlinear susceptibility, $\chi_{ijk}^{(2)}$. SFG is a highly surface sensitive technique because the $\chi_{eff}^{(2)}$ is equal to zero in a bulk medium with inversion symmetry under the electric dipole approximation.[30]

$$I_{SFG} \propto \left|\chi_{eff}^{(2)} E_{1064nm} E_{IR}\right|^2 \qquad \textbf{Equation 4-1}$$

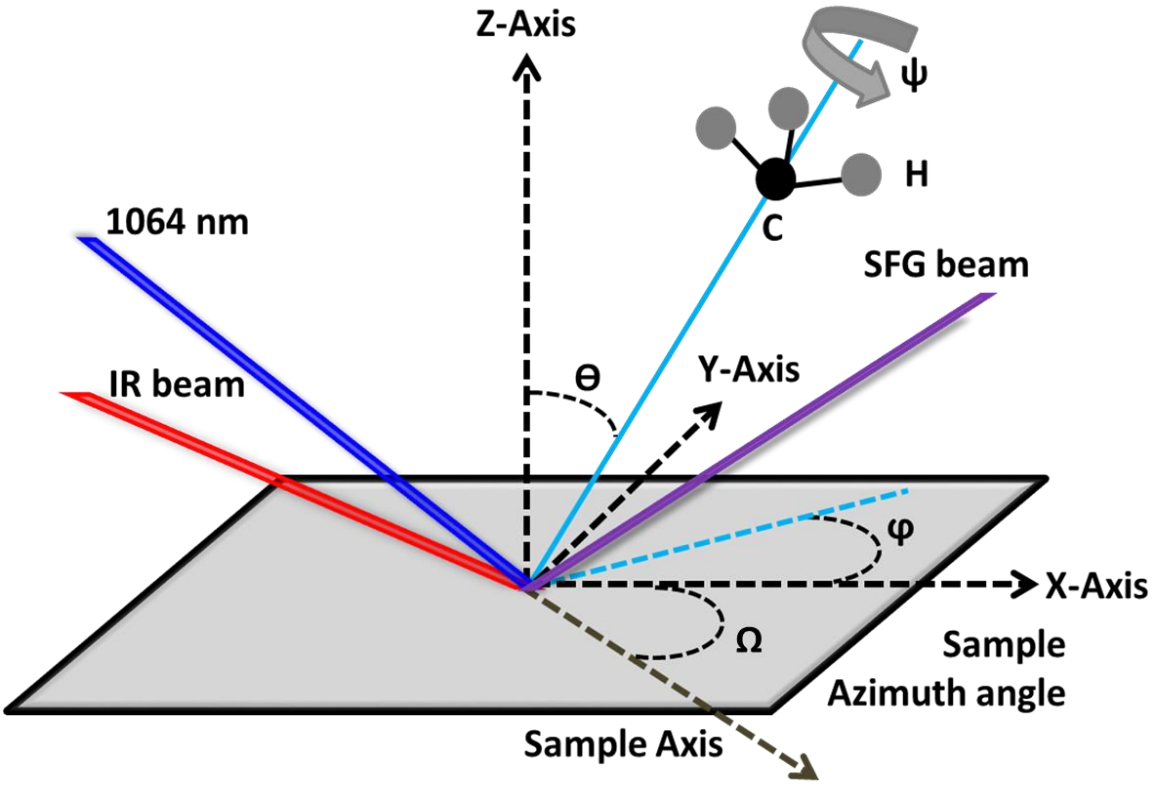

Figure 4-1. Definition of the tilt angle (θ), azimuth angle (φ), and rotation angle (ψ) of molecular adsorbed on the surface and sample azimuth angle Ω.

The $\chi_{ijk}^{(2)}$ is related to molecular hyperpolarizability $\beta_{i'j'k'}^{(2)}$ through ensemble average over all possible molecular orientations shown in Equation 2-13. The molecular

orientation including tilt angle (θ), azimuth angle (in surface coordinate system) (φ), and rotation angle (ψ) are redefined in Figure 4-1.

The sample azimuth angle Ω (in the laboratory coordinate system) which is important in this study is also demonstrated in Figure 4-1. Equation 2-12 is the basis equation for the nonlinear model fitting of SFG spectra used for orientation analysis and mapping results. Both $\chi_{\mathrm{R}}^{(2)}$ and $\chi_{\mathrm{NR}}^{(2)}$ are complex quantities, so the SFG spectra are complicated, especially for the metal which contributes strong non-resonant background due to the nearly free electrons in surface region, resulting in complex line shapes.[31,32]

4.3. Experimental section

4.3.1. Sample preparation

The material used in this work is a polycrystalline rectangular copper sheet (Goodfellow, 99.99%) with an area of 1cm^2 and the thickness of 3 mm. One side of copper surface is polished down to 0.1 μm size using diamond paste. The copper is annealed in furnace with argon (300 sccm) and hydrogen (30 sccm) at temperature of 1050 °C for 3 h. Then, the copper sample is cooled down to room temperature in argon and hydrogen flow atmosphere and is immediately immersed into 5 mM ODT/ethanol solution. After 2 h, the copper sample is taken out from the ODT solution, rinsed with ethanol, and dried under nitrogen flow in the glove box to prevent the oxidation of copper. The copper is then mounted in the SFG cell filled with nitrogen gas. The SFG cell is mounted on an x-y-z plus tip/tilt 5 axis stage for the SFG imaging experiment.

4.3.2. SFG imaging experiment

SFG imaging microscopy was described in detail elsewhere.[25] A picosecond pulsed Nd:YAG laser(EKSPLA) with a 20 Hz repetition rate provides the 1064 nm beam which pumps the optical parametric generator/amplifier(OPG/OPA) to yield the IR beam that is tunable from 2000-4000 cm^{-1}. The incidence angles of the IR and 1064 pump beams are 70° and 60° from the surface normal, respectively. The emitted angle of SFG beams is 62.1° from surface normal. The polarization of the two incident beams are both p-polarized (parallel to the incidence plane) set by polarizer and the polarization of SFG signal is considered to be p-polarized (p-polarized SFG signal dominates the SFG signal), which this polarization combination is designed as PPP. A Roper Scientific CCD camera with 1024×1024 pixel array was used for SFG beam profile collection. Each SFG image is 1024×1024 pixels and 1 pixel is corresponding to 1 μm distance on surface. The spatial resolution is approximately 2 μm. The SFG beam wavelength (IR wavenumber range 2750 cm^{-1}-3050cm^{-1}) is around 808 nm. An 808 nm unpolarized CW laser with a wavelength that is close to the SFG wavelength at an incidence angle of 62.1° is used to simulate the SFG beam path and generate a reference image which shares the same sample position with the SFG image.

4.4. Results and discussions

4.4.1. SFG image analysis

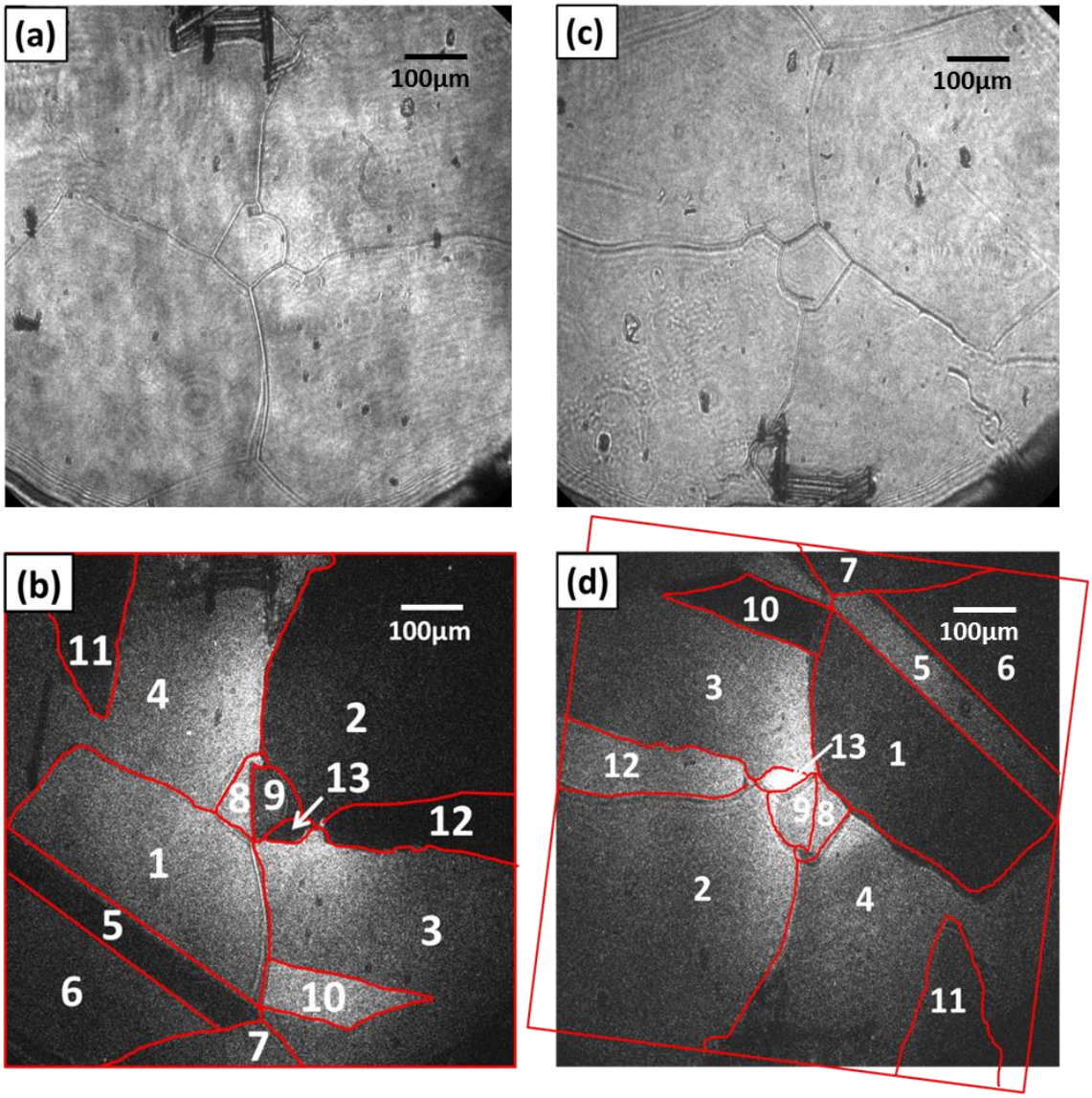

Figure 4-2. Left (a) and (b): Optical image (wavelength, 808 nm) and unprocessed SFG image (IR wavenumber: 3050 cm^{-1}) of the copper surface with the ODT monolayer at the azimuth angle of 0°. Right (c) and (d): Optical image (wavelength, 808 nm) and unprocessed SFG image (IR wavenumber: 3050 cm^{-1}) of the copper surface with the ODT monolayer at the azimuth angle of 180°. SFG images are taken with the PPP polarization. The red frame marked the GBs in (c) and was rotated to fit the GBs in (d).

Figure 4-2a and Figure 4-2c present the optical image using 808 nm optical microscope on the copper sample at two azimuth angles of 0° and 180°, respectively. Several domains and boundaries are displayed in the optical images. The domain sizes are

a few hundred micrometers. The whole copper surface is optically flat and different domains show no brightness contrast with each other. When the sample's azimuth angle changes, the contrast in the optical image is essentially unchanged.

Figure 4-2b and Figure 4-2d show the SFG image for the two azimuth angles at 3050 cm^{-1}. These images are slices from the 51 image stack acquisition from 2800 to 3050 cm^{-1}. Because the image was acquired in the non-resonant IR region (3050 cm^{-1}), the SFG intensity on Figure 4-2b and Figure 4-2d is associated with the nonlinear susceptibility of the copper substrate. Based on the observation, several domains with distinctive brightness contrast were identified in the SFG image with various sizes (10-300μm), suggesting difference of SFG signal response existing in each domain, which was not detected in the corresponding optical images. EBSD techniques have been applied to characterize copper surfaces which is obtained using the same sample preparation procedure, and the crystallographically diversified Cu surface was identified with various crystal facets such as Cu(111), Cu(310), and Cu(410).[2,27] Compared with the domains shown in the EBSD image, the domains of the SFG image were similar in size and shape. Thus, the domain structure in the SFG image could also be explained in terms of micrometer-sized crystal facets existing on the copper surface. As the SFG intensity is directly associated with the nonlinear susceptibility of the copper substrate, Thus the SFG intensity difference in different domains of the image is related to the nonlinear surface susceptibility varying on different crystal grains of the copper surface.

Next, the spatial correlation of the optical image with the SFG image was investigated. All the boundaries shown in optical image are observed in the SFG image.

However, some clearly observable boundaries in the SFG image were not obtained in the optical image, such as the boundary between domains 1 and 5 in Figure 4-2c. Previous studies showed that when the collision of the formed domains after the initiation of atom nucleation occurs on the copper surface, the extent of mis-orientation of the surface atom structures in two adjacent grain domains determines the formation of boundaries with clear geometrical boundaries.[9] The reflectivity difference resulting from the geometry makes the boundaries appear in the optical image. In other words, the boundaries between crystal grains without remarkable boundary grooves could not be distinguished in the optical image. Hence, the SFG microscope is able to reveal crystal grain structure of metal surface.

A comparison between Figure 4-2b with Figure 4-2d, the brightness contrast between each domain changes while the sample is rotated around the surface normal. For example, domain 1 is brighter than domain 2 in Figure 4-2b, while the domain 2 is brighter than domain 1 in Figure 4-2d. In addition, some GBs which are obvious in Figure 4-2b disappear in Figure 4-2d, such as that between region 11 and 4 in Figure 4-2a. In contrast, some domains such as 7, 12, and 13 which are obvious in Figure 4-2d are not perceivable in Figure 4-2c. A series of SFG images with four more azimuth angles presented in Figure B-2 confirm this phenomenon. These results imply there is azi muthal anisotropy of the SFG response in copper domains. Based on previous studies performed by nonlinear optical techniques including Second Harmonic Generation (SHG) and SFG-VS on gold[33], silver[34] and copper[35], these effects are correlated to the azimuthal anisotropy of the nonlinear susceptibility of metallic crystal facets. A phenomenological macroscopic explanation on the anisotropy of nonlinear optical signal response of single crystal facets such as (111), (110), and (100) was reported in Sipe and coworkers results.[36] Based on this

discussion, and the previous studies, the brightness contrast of the different domains results from various crystal facets that exists on the copper surface.

4.4.2. Local SFG spectrum comparison

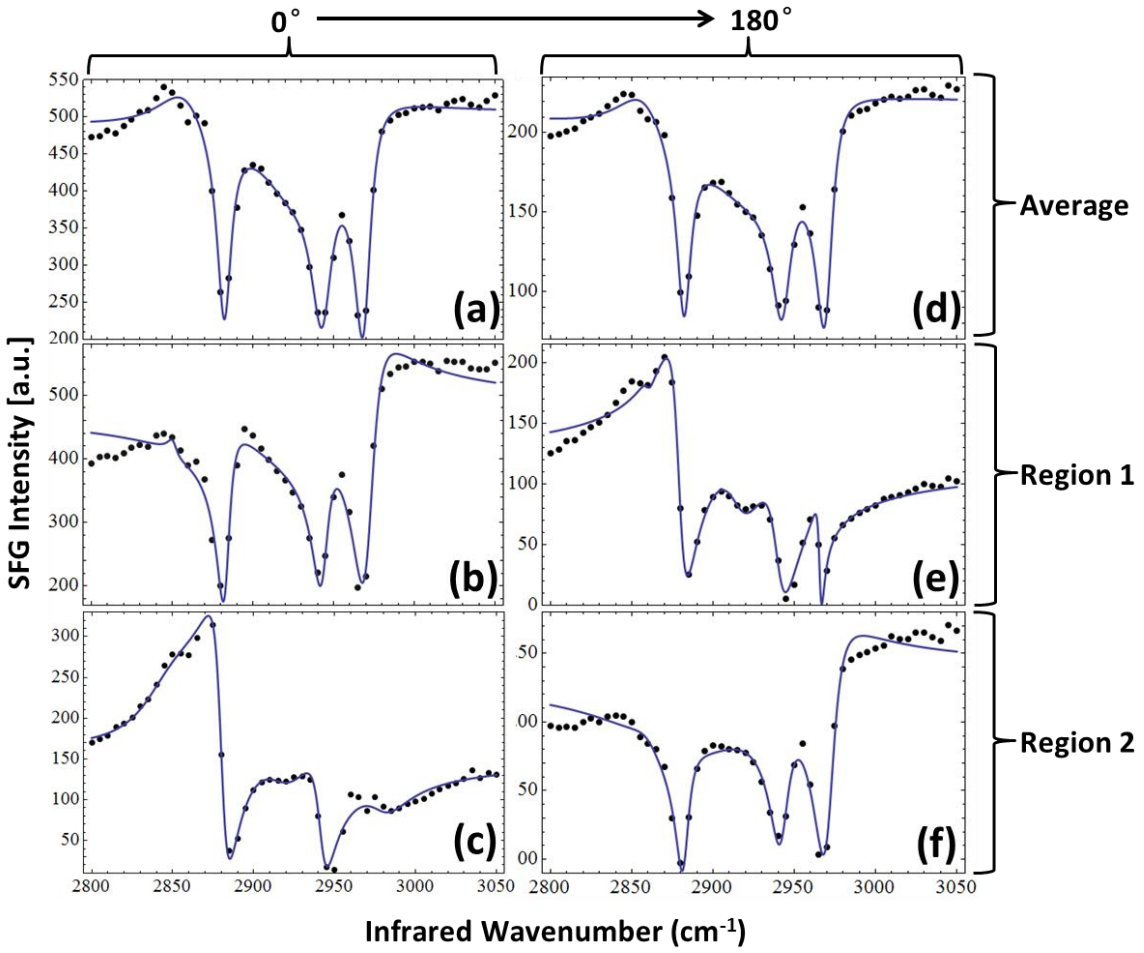

Figure 4-3. SFG spectra (2800 cm^{-1}-3050 cm^{-1}) of the copper surface with an ODT self-assembled monolayer. (a) and (d) represent the average SFG spectra of Figure 4-2b and Figure 4-2d, respectively. (b) and (c) represent the SFG spectra from domain 1 and domain 2 in Figure 4-2b, respectively. (e) and (f) represent the SFG spectra from domain 1 and domain 2 in Figure 4-2d, respectively. The solid blue lines are the fits using Equation 4-2. The fitting results are listed in Table B-1.

A series of SFG spectra of the ODT monolayer on the copper surface were extracted from the set of SFG images for azimuth angles from 0° and 180° and presented in Figure

4-3. The five peaks of the SFG spectra corresponding to the CH_2 symmetric stretch 2850 cm^{-1}, the CH_3 symmetric stretch 2880 cm^{-1}, the CH_2 Fermi resonance 2915 cm^{-1}, the CH_3 Fermi resonance 2940 cm^{-1}, and the CH_3 asymmetric stretch 2970 cm^{-1}, respectively, were observed.[37] Shown in Figure 4-3a and Figure 4-3d are the average SFG spectra of the sample at two different azimuth angles, revealing minor difference between each other. However, the line shapes of the local spectra in Figure 4-3b and Figure 4-3c show remarkable differences from each other, as well as the average spectrum in Figure 4-3a, respectively. The line shape of the SFG spectrum depends on the relative phase ϕ between $\chi_{R}^{(2)}$ and $\chi_{NR}^{(2)}$ as shown in Equation 4-2. The electronic structure of the metal substrates can cause the non-resonant background and relative phase change.[32] Thus, the spectral changes observed in Figure 4-3 could be explained in terms of electronic structure difference resulting from two aspects: different crystal facets on copper surface and same crystal facet with different orientations of ODT. This also implies that the SFG relative phase and non-resonant background are coupled to the underlying copper crystal structure.

Both of the SFG spectra in Figure 4-3b and Figure 4-3e are obtained from the same sample area which is the domain 1. Nevertheless, comparing the spectra, the spectral line shapes show remarkable difference. This is also applied to the comparison of spectra in the Figure 4-3c and Figure 4-3f. These results indicate SFG spectra exhibit an obvious anisotropy while the sample azimuth angle changes. From Table B-1, the non-resonant part such as relative phase and resonant part such as the amplitude of $CH_{3\text{-sym}}$ change values with respect to azimuthal rotation. The non-resonant SFG signal is generated from the copper substrate and its dependence on azimuth angle is interpreted in the following context. The non-resonant parameters such as the relative phase of SFG spectra result from

the anisotropy of the nonlinear susceptibility of crystalline substrate. This type of anisotropy of the nonlinear susceptibility was also observed in previous SFG studies on Au(111)[33] and Si(111)[38]. The resonant part of SFG signal is generated at the air/monolayer interface, and its dependence on azimuth angle is directly related to the monolayer orientation. Therefore, a qualitative analysis for our results denotes an orientation distribution for the ODT chains that exhibit narrow angular ranges in azimuth angles. Similar ordered monolayer systems on the polyvinyl alcohol surface[39] and the LB film surface of cadmium arachidate[40] also show anisotropy of SFG signals.

The remarkable difference between the local spectra with average spectra, as well as the spectral anisotropy shown in Figure 4-3 is of great importance because many SFG studies were performed on monolayers absorbed on various metallic surfaces. Without independent knowledge of various crystal grains existing on the metal surface, the ensemble average information of such surface is usually obtained by a wholesale integration of spectrum based on the assumption that surface crystal facet distribution is spatially homogenous. However, the local features on individual grains, and especially the GBs might be overlooked, which leads to an inaccurate interpretation of the system. Hence, analyzing the local spectrum with more details is indispensable. The ability to visualize the surface by SFG imaging provides new perspective for the understanding of surface chemistry on metals in the micrometer scale.

4.4.3. Statistical analysis of SFG image

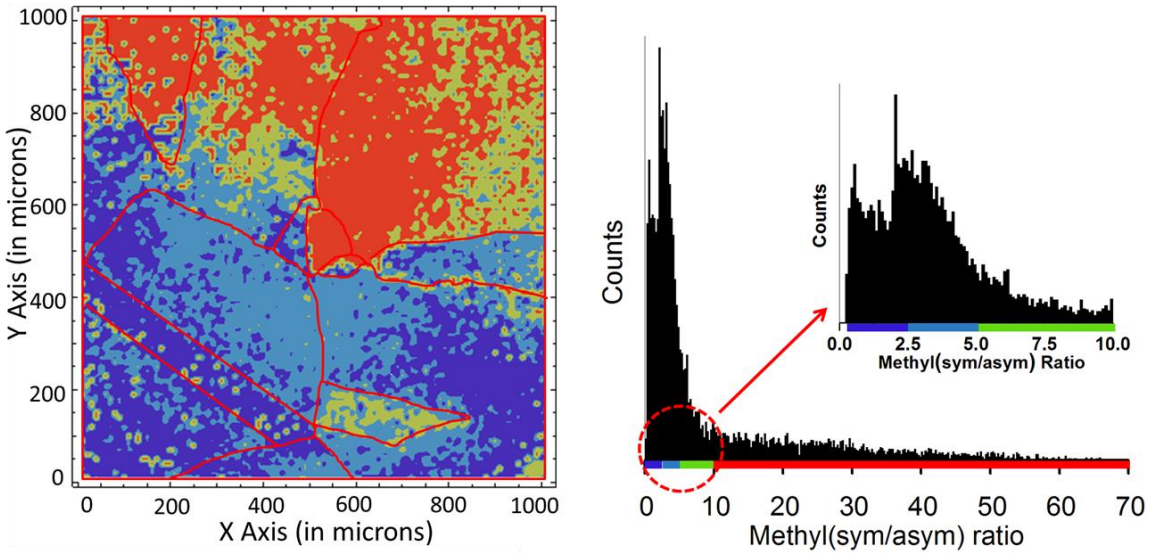

Figure 4-4. (a) Contour map of amplitude ratio of $CH_{3\text{-sym}}/CH_{3\text{-asym}}$; (b) Histogram of amplitude ratio of $CH_{3\text{-sym}}/CH_{3\text{-asym}}$; Corresponding colors (blue:0-2.5, light blue:2.5-5, green:5-10, red:10-70) in the contour map (a) represent specific amplitude ratio range selected in the histogram (b). The red color marks corresponding area in the selected ratio range.

The whole set of SFG image (azimuth angle 0° shown in Figure 4-2b) was divided into 10,000 regions of interest (ROI) which is a 10 μm × 10 μm square. The SFG spectra were extracted and fitted by Equation 4-2. The amplitude ratios of methyl symmetric stretching mode and methyl asymmetric stretching mode of each ROI were obtained and then used to reconstruct a chemical image and presented in Figure 4-4.

The methyl group of ODT has two fundamentals in the CH stretch region. Based on the surface IR selection rule on perfect conductor, only the fundamentals have a nonzero component of transition moment positioned along the surface normal are observed in the SFG spectrum. When the C_3 axis of the methyl group tilts farther away from the surface normal, the asymmetric mode become greater and the symmetric mode become smaller.[41,42] The SFG technique is able to analyze the orientation conformation of the

terminal methyl group of ODT (including the tilt angle, azimuth angle and rotation angle demonstrated in Figure 4-1) on copper surface based on the amplitude ratio of $CH_{3\text{-}sym}/CH_{3\text{-}asym}$ under PPP polarization combination.[40,43] To perform a comprehensive calculation of orientation, parameters such as the interfacial refractive indices, as well as the molecular hyperpolarizability elements and relative phase are required and this analysis is ongoing. In this study, the contour map of the amplitude ratio of $CH_{3\text{-}sym}/CH_{3\text{-}asym}$ shown in Figure 4-4(a) is spatially correlated to the local orientation angle of ODT molecules on the copper surface. The monolayer heterogeneity could be deduced from the amplitude ratio analysis. In Figure 4-4a, several domains and boundaries, of which the size and shape are similar to the domains in Figure 4-2b, are observed. The red frame of Figure 4-2b is applied on the Figure 4-4a which makes this effect more obvious. It illustrates that the packing of ODT molecules on copper surface is heterogeneous and the heterogeneity of molecular packing is resulting from copper substrates with various grain structures underneath the ODT monolayer.

Figure 4-4b shows the amplitude ratio distribution from 0 to 70.0. Most ROIs' ratios are located between 0 to 10, and this range in the histogram is magnified in Figure 4-4b. The domains which are marked with four different colors shown in Figure 4-4a correspond to the four ratio ranges which is selected to magnify the domain effect shown in Figure 4-4a (0-2.5, 2.5-5, 5-10 and 10-70), respectively. It suggests that each crystal grain contains its characteristic SAMs monolayer packing behavior which is different from other crystal grains. And this is well known from previous studies.[44,45] The reason why the underlying grain structure affects the top monolayer packing behavior could be that the copper surface atom density and electron density vary with different copper grains, which makes ODT

molecules more preferentially be adsorbed on the grain with special facet, thereby forming domains following the underlying copper grain structure. It further suggests that the surface becomes more heterogeneous with the existence of the copper grain structure.

Based on the assumption that the tilt angle distribution for the ODT molecules follows a δ function and the rotation angle together with azimuth angle are randomly distributed, a theoretical curve simulating the amplitude ratio of $CH_{3\text{-}sym}/CH_{3\text{-}asym}$ as a function of the tilt angle of methyl groups was plotted and is presented in the Figure B-4 (more detail about this theoretical curve is presented in the Appendix B). However, crystallographic domains of the copper substrate should give rise to various azimuthal ODT packing domains. Such domains have already been identified by STM in alkanethiol SAMs on Au (111).[46,47] It has to be pointed out that the assumption that the azimuth angles are random distribution introduces bias to calculation. More systematic research and discussion for azimuth angle distribution should be performed for accurate determination of the orientation of the ODT monolayer in such a system. Besides, Fresnel factors that relate the electric field in bulk media to the electric field at the interface are normally calculated using the equations given by Zhuang et al[48], based on the assumption that the substrates are homogenous. However, the atom density and crystal orientation with respect to incident light vary on crystal grains, which complicate Fresnel factors. Thus, for the SFG orientation analysis on similar systems, this effect should be discussed in more detail in the future.

4.5. Conclusion

In summary, micrometer-scale crystal grains and GBs were identified by the SFG imaging technique for the first time. It provides new clues for a broad range of interest such as localized corrosion processes on copper surfaces with crystal grain structures. Besides, the marked difference of SFG spectra across domains relates the localized molecular information to the overall performance of the whole surface area, which suggests the importance of considering the heterogeneity of ODT monolayers on polycrystalline copper surfaces. Consequently, spectroscopic visualization of the surface leads to an accurate understanding of surface chemistry. The anisotropy of SFG spectra observed in the present work will inspire the further SFG research on the metal substrates.

4.6. References

(1) Schweitzer, P. A. *Fundamentals of corrosion: mechanisms, causes, and preventative methods*; CRC Press, **2009**.

(2) Martinez-Lombardia, E.; Maurice, V.; Lapeire, L.; De Graeve, I.; Verbeken, K.; Kestens, L.; Marcus, P.; Terryn, H. *J. Phys. Chem. C* **2014**, *118*, 25421.

(3) Lapeire, L.; Martinez Lombardia, E.; Verbeken, K.; De Graeve, I.; Kestens, L. A. I.; Terryn, H. *Corros. Sci.* **2013**, *67*, 179.

(4) Park, C. J.; Lohrengel, M. M.; Hamelmann, T.; Pilaski, M.; Kwon, H. S. *Electrochim. Acta* **2002**, *47*, 3395.

(5) Martinez-Lombardia, E.; Lapeire, L.; Maurice, V.; De Graeve, I.; Verbeken, K.; Klein, L. H.; Kestens, L. A. I.; Marcus, P.; Terryn, H. *Electrochem. Commun.* **2014**, *41*, 1.

(6) Martinez-Lombardia, E.; Gonzalez-Garcia, Y.; Lapeire, L.; De Graeve, I.; Verbeken, K.; Kestens, L.; Mol, J. M. C.; Terryn, H. *Electrochim. Acta* **2014**, *116*, 89.

(7) Schreiber, A.; Schultze, J. W.; Lohrengel, M. M.; Karman, F.; Kalman, E. *Electrochim. Acta* **2006**, *51*, 2625.

(8) Lill, K. A.; Hassel, A. W.; Frommeyer, G.; Stratmann, M. *Electrochim. Acta* **2005**, *51*, 978.

(9) Miyamoto, H.; Yoshimura, K.; Mimaki, T.; Yamashita, M. *Corros. Sci.* **2002**, *44*, 1835.

(10) Luo, W.; Xu, Y.; Wang, Q.; Shi, P.; Yan, M. *Corros. Sci.* **2010**, *52*, 3509.

(11) Ralston, K. D.; Birbilis, N. *Corrosion* **2010**, *66*.

(12) Claypool, C. L.; Faglioni, F.; Goddard, W. A.; Gray, H. B.; Lewis, N. S.; Marcus, R. *J. Phys. Chem. B* **1997**, *101*, 5978.

(13) Claypool, C. L.; Faglioni, F.; Goddard, W. A.; Lewis, N. S. *J. Phys. Chem. B* **1999**, *103*, 7077.

(14) Claypool, C. L.; Faglioni, F.; Matzger, A. J.; Goddard, W. A.; Lewis, N. S. *J. Phys. Chem. B* **1999**, *103*, 9690.

(15) Yu, H.; Webb, L. J.; Ries, R. S.; Solares, S. D.; Goddard, W. A.; Heath, J. R.; Lewis, N. S. *J. Phys. Chem. B* **2005**, *109*, 671.

(16) Barrena, E.; Kopta, S.; Ogletree, D. F.; Charych, D. H.; Salmeron, M. *Phys. Rev. Lett.* **1999**, *82*, 2880.

(17) Barrena, E.; Ocal, C.; Salmeron, M. *J. Chem. Phys.* **2000**, *113*, 2413.

(18) Hosseinpour, S.; Johnson, C. M.; Leygraf, C. *J. Electrochem. Soc.* **2013**, *160*, C270.

(19) Hosseinpour, S.; Hedberg, J.; Baldelli, S.; Leygraf, C.; Johnson, M. *J. Phys. Chem. C* **2011**, *115*, 23871.

(20) Laibinis, P. E.; Whitesides, G. M. *J. Am. Chem. Soc.* **1992**, *114*, 9022.

(21) Nuzzo, R. G.; Allara, D. L. *J. Am. Chem. Soc.* **1983**, *105*, 4481.

(22) Laibinis, P. E.; Whitesides, G. M.; Allara, D. L.; Tao, Y. T.; Parikh, A. N.; Nuzzo, R. G. *J. Am. Chem. Soc.* **1991**, *113*, 7152.

(23) Fonder, G.; Cecchet, F.; Peremans, A.; Thiry, P. A.; Delhalle, J.; Mekhalif, Z. *Surf. Sci.* **2009**, *603*, 2276.

(24) Santos, G. M.; Baldelli, S. *J. Phys. Chem. C* **2013**, *117*, 17591.

(25) Cimatu, K. A.; Baldelli, S. *J. Phys. Chem. C* **2009**, *113*, 16575.

(26) Cimatu, K.; Baldelli, S. *J. Phys. Chem. B* **2006**, *110*, 1807.

(27) Wood, J. D.; Schmucker, S. W.; Lyons, A. S.; Pop, E.; Lyding, J. W. *Nano Lett.* **2011**, *11*, 4547.

(28) Torchinsky, D. H.; Chu, H.; Qi, T.; Cao, G.; Hsieh, D. *Rev. Sci. Instrum.* **2014**, *85*.

(29) Shen, Y. R. *Nature* **1989**, *337*, 519.

(30) Zhu, X.; Suhr, H.; Shen, Y. *Phys. Rev. B* **1987**, *35*, 3047.

(31) Harris, A. L.; Chidsey, C. E. D.; Levinos, N. J.; Loiacono, D. N. *Chem. Phys. Lett.* **1987**, *141*, 350.

(32) Bain, C. D. *J. Chem. Soc. Faraday T.* **1995**, *91*, 1281.

(33) Yeganeh, M. S.; Dougal, S. M.; Polizzotti, R. S.; Rabinowitz, P. *Phys. Rev. Lett.* **1995**, *74*, 1811.

(34) Harris, A.; Rothberg, L.; Dhar, L.; Levinos, N.; Dubois, L. *J. Chem. Phys.* **1991**, *94*, 2438.

(35) Tom, H.; Aumiller, G. *Phys. Rev. B* **1986**, *33*, 8818.

(36) Sipe, J.; Moss, D.; Van Driel, H. *Phys. Rev. B* **1987**, *35*, 1129.

(37) Jennings, G. K.; Munro, J. C.; Yong, T. H.; Laibinis, P. E. *Langmuir* **1998**, *14*, 6130.

(38) Malyk, S.; Shalhout, F. Y.; O'Leary, L. E.; Lewis, N. S.; Benderskii, A. V. *J. Phys. Chem. C* **2013**, *117*, 935.

(39) Wei, X.; Zhuang, X.; Hong, S. C.; Goto, T.; Shen, Y. R. *Phys. Rev. Lett.* **1999**, *82*, 4256.

(40) Hirose, C.; Yamamoto, H.; Akamatsu, N.; Domen, K. *J. Phys. Chem.* **1993**, *97*, 10064.

(41) Parikh, A. N.; Allara, D. L. *J. Chem. Phys.* **1992**, *96*, 927.

(42) Allara, D. L.; Swalen, J. D. *J. Phys. Chem.* **1982**, *86*, 2700.

(43) Wang, H. F.; Gan, W.; Lu, R.; Rao, Y.; Wu, B. H. *Int. Rev. Phys. Chem.* **2005**, *24*, 191.

(44) Camillone, N.; Chidsey, C. E. D.; Liu, G.; Scoles, G. *J. Chem. Phys.* **1993**, *98*, 4234.

(45) Love, J. C.; Estroff, L. A.; Kriebel, J. K.; Nuzzo, R. G.; Whitesides, G. M. *Chem. Rev.* **2005**, *105*, 1103.

(46) Poirier, G. E.; Tarlov, M. J. *Langmuir* **1994**, *10*, 2853.

(47) Smith, R. K.; Lewis, P. A.; Weiss, P. S. *Prog. Surf. Sci.* **2004**, *75*, 1.

(48) Zhuang, X.; Miranda, P. B.; Kim, D.; Shen, Y. R. *Phys. Rev. B* **1999**, *59*, 12632.

CHAPTER 5. Orientation and Conformation Analysis of a Molecular Monolayer on Microcrystalline Copper Surface: Mapping Molecular Heterogeneity at Grains and Grain Boundaries by Sum Frequency Generation Imaging Microscopy

5.1. Introduction

The studies of the thin organic film on metal surfaces are of critical importance not only for fundamental science but also for a wide variety of technological functionalities such as wettability, corrosion inhibition, biosensors, and nanotechnology.[1-8] Various techniques including IR spectroscopy,[9,10] X-ray photoelectron spectroscopy,[11,12] contact angle,[10,13] ultrafast spectroscopy,[14,15] and scanning tunneling microscopy[16,17] have been employed to investigate such systems. The most studied system is that of self-assembled monolayers on metal surfaces due to their simple chemical adsorption, well order structure, and monolayer thickness.[18] An important results from previous studies is that alkanethiols can form well-ordered monolayers on metal surfaces, which modifies the surface properties.[19,20] It may be more important, however, such order molecular structure including the conformation order, lateral order, and symmetry of monolayer are of critical importance in determining the physical and chemical properties of SAMs monolayer, which influence the surface functionalities such as wettability, corrosion, and other applications.[21,22]

Various sized crystal domains with different crystallographic orientations naturally exist on most metallic material surfaces.[23,24] A major area of interest is whether such feature

surface atom arrangements influence the local physical and chemical properties of a monolayer. A common strategy to investigate such correlation is to compare the properties of SAMs on different well-defined single-crystal surface.[25,26] Sum frequency generation vibrational spectroscopy (SFG-VS), as a vibrational spectroscopy technique, which has an excellent chemical selectivity and interfacial sensitivity, has been extensively applied to characterize the ordered organic monolayer formed on single crystal surfaces. Yeganeh *et al.* reported the three fold symmetry of the SFG signal from the surface of a SAM on an Au(111) and attributed the azimuthal anisotropy to the bonding sites.[27] Benderskii *et al.* reported a pronounced azimuthal anisotropy of the 3-fold symmetry with the SFG signal on methyl terminated Si (111) surfaces.[28] Uosaki applied SFG to investigate a C18 monolayer on a hydrogen-terminated Si (111) surface and confirmed that the monolayer was arranged epitaxial with C_{3v} anisotropy and the alkyl chains tilt towards the <211> direction.[21]

However, evaluating different single crystal surfaces requires multiple measurements with careful preparing, characterizing, and handling of each crystal surface in exactly the same experimental conditions, which can be both time-consuming and expensive. In addition to these experimental difficulties, the crystal boundaries between different crystallographic grains,[29] which play an important role in determining surface reactivity, are difficult to probe based on spectroscopy methods alone. Therefore, to study the molecular behavior of metal surfaces with various grains structure and to determine information about the grain boundaries, a simple and more direct measurement method is imperative. SFG imaging provides a promising and practical solution to these problems. SFG imaging microscopy as a vibrational spectroscopy technique applied in microscope

mode could directly probe the local molecular packing information, as well as the underneath metal structure of a polycrystalline metal.[30-32] Recently, it has been shown that SFG imaging studies of clear copper grains structures are possible, which allows a direct correlation between local molecule information and the underlying copper grain structure.[33] It was also proposed that the spectral fitting parameter obtained from the local SFG spectra can be used to reconstruct the corresponding chemical map of the monolayer and quantitatively determine the conformation order of the monolayer in each crystal domain with distinct crystallographic orientation; However, such a proposal requires further substantiation and addressing about whether phase variation in different azimuthal angles would influence the interpretation of the SFG spectra since the SFG spectra are strongly dependent of the azimuthal angle. Furthermore, the more important issue about the existence of the lateral order of the monolayer also needs to be further addressed.

In the present work, comprehensive SFG imaging studies about the ODT monolayer on a microcrystalline copper surface with a symmetric anisotropy comparison is presented, with the combination of SHG and EBSD techniques. Based on the quantitative measurements of SAMs on Cu (111) and theoretical derivations, we shows that all the spectral fitting parameters of molecular are fully independent from the azimuthal angle. The conformation order such as orientation angle distribution of metal group of thiol molecular on each individual crystal grains is quantitatively analyzed. In addition, correlations between the molecular behavior and the copper surface structure (in particular, the crystallographic orientation) is identified.

5.2 Theoretical basis

There are a number of reviews, which introduce the theoretical background of SFG and its applications.[34-36] Only relevant equations of SFG spectroscopy is briefly presented here. As shown in Equation 5-1, SFG is a second-order nonlinear optical process which involves two laser beams spatially and temporally overlapped on the surface, to induce a second order polarization, $P_{SF}^{(2)}$.[37] The second order nonlinear optical process is forbidden in a medium with inversion symmetry under the electric dipole approximation, but are active at the interface where the inversion symmetry is necessarily broken.[38] The second-order susceptibility $\boldsymbol{\chi}_{eff}^{(2)}$ shown in Equation 3-1 contains both a non-resonant contribution $\chi_{\mathrm{NR}}^{(2)}$ and a resonant contribution $\chi_{\mathrm{R}}^{(2)}$, which relates the induced second-order polarization response to the intensity of the incident beams. $\chi_{\mathrm{NR}}^{(2)}$ is the non-resonant contribution typically attributed to electronic excitations of the substrate and the adsorbate. $\chi_{\mathrm{R}}^{(2)}$ is associated with resonant vibrations of the adsorbate molecule layer and is significantly changed when the frequency of an incident infrared beam (ω_{IR}) is coincident with a specific molecular vibrational mode, q. As shown in Equation 2-13, the $\boldsymbol{\chi}_{eff}^{(2)}$, which is defined in the laboratory coordinates system λ (x,y,z), could correlate the molecular microscopic hyperpolarizability $\beta^{(2)}$ in the molecular coordinates system λ (a,b,c) through the ensemble average over all possible molecular orientations.[39] The molecular-fixed coordinates for the methyl group are defined as depicted in Figure 5-1A. The c–axis is taken to coincide with the C_{3v} symmetry axis of the methyl group, and the a-c plane is one of the C-C-H planes of the methyl group. The molecular orientation in the laboratory fixed axis system including tilt angle (θ), azimuth angle (in surface coordinate system) (φ), and rotation angle (ψ) are defined in Figure 5-1B. Equation 2-12 serves as the basis equation

for the nonlinear model fitting of SFG spectra used for orientation analysis and mapping results.

SFG spectra are complicated by THE convolution between $\chi_{\mathrm{R}}^{(2)}$ and $\chi_{\mathrm{NR}}^{(2)}$ shown in Equation 5-1. Due to the enormous nearly free electrons in the surface region, the non-resonant contribution from the metal and semiconductor is typically large, resulting in a complex SFG lineshape.[35,40] The ε and δ denote the phase of $\chi_{\mathrm{R}}^{(2)}$ and $\chi_{\mathrm{NR}}^{(2)}$ respectively, and the phase difference between $\chi_{\mathrm{R}}^{(2)}$ and $\chi_{\mathrm{NR}}^{(2)}$ is the relative non-resonant phase ϕ.

$$I_{SF} \propto \left|\chi_{NR}^{(2)}\right|^2 + \left|\chi_{R}^{(2)}\right|^2 + 2\left|\chi_{NR}^{(2)}\right|\left|\chi_{R}^{(2)}\right|\cos[\varepsilon - \delta] \qquad \textbf{Equation 5-1}$$

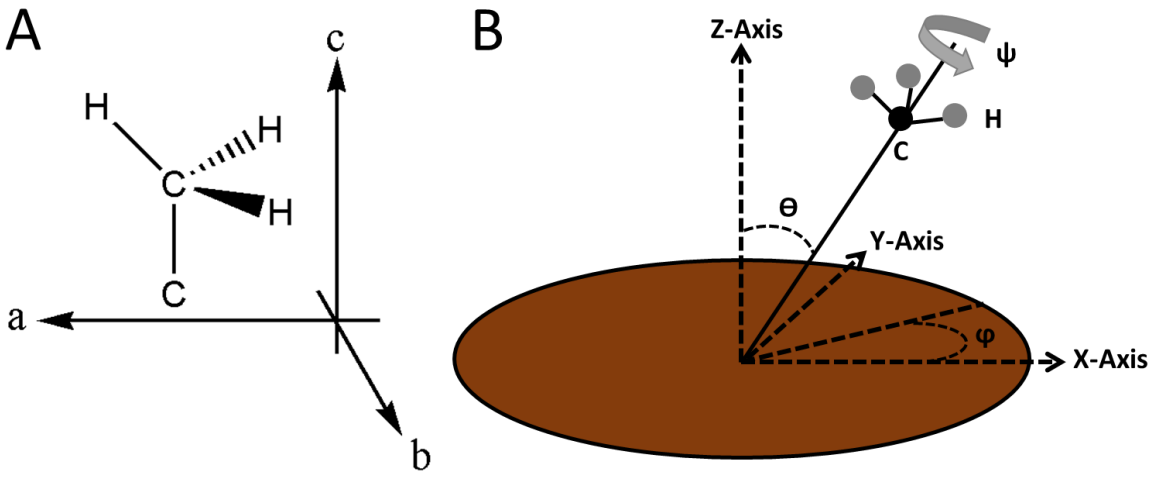

Figure 5-1: Schematic drawing of the definitions of the molecular fixed axis systems (A) and laboratory fixed axis system (B).

5.3. Experimental section

The sample preparation method was described elsewhere.[33] A 1 cm^2 polycrystalline rectangular copper sheet (Goodfellow, 99.99%) of 3 mm thickness is employed as the

sample in this work. One side of the copper surface is polished down to 0.1 μm by diamond paste with mirror like. The copper is transferred to a furnace and annealed with argon (300 sccm) and hydrogen (30 sccm) at a temperature of 1050 °C for 3 h. Then, the copper sample is cooled down to room temperature, under the same argon and hydrogen flow atmosphere, and is immediately immersed into a 5 mM ODT/ethanol solution. After 2 h, the copper sample is taken out from the ODT solution, rinsed with ethanol, and dried under nitrogen flow in the glove box to prevent the oxidation of copper. The copper is then mounted in the SFG cell filled with nitrogen gas. The SFG cell was mounted on an x-y-z plus tip/tilt 5 axis stage for the SFG imaging experiment.

SFG imaging setup was described in previous chapters.[41,42] A picosecond pulsed Nd:YAG laser(EKSPLA) with a 20 Hz repetition rate provides the 1064 nm beam serves as the pump beam of SFG, as well as the pump beam of the tunable IR beam from 2000-4000 cm^{-1} that is generated from the optical parametric generator/amplifier (OPG/OPA). The SFG imaging is set in a reflection configuration with the incidence angles of the IR and 1064 pump beams at 70° and 60° from the surface normal, respectively. The emission angle of the SFG beam is set at 62.1° from the surface normal. The polarization of the 1064 nm beam and the tunable IR beam are both p-polarized (parallel to the incidence plane) set by a polarizer, and the polarization of the SFG signal is considered to be p-polarized (p-polarized SFG signal dominates the SFG signal). This polarization combination is assigned as PPP. A Roper Scientific CCD camera with 1024×1024 pixel array is used for collecting the intermediated SFG image on a grating by using of a 10 X objective lens for magnification and a tube lens for collimation. Each SFG image is 1024×1024 pixels and 1 pixel is corresponding to 1 μm distance on the surface. The spatial resolution is

approximately 1 µm. The SFG beam wavelength (IR wavenumber range 2750-3050cm^{-1}) is around 808 nm. The sample azimuth angle (ϕ) is also demonstrated in Figure 5-2. The absolute number of the azimuth angle is arbitrary. An 808 nm unpolarized CW laser at an incidence angle of 62.1°, which is close to the incidence angle of the SFG beam is used to simulate the SFG beam path. The 808 nm optical image that is collected by the CCD camera shares the same sample position with the SFG image.

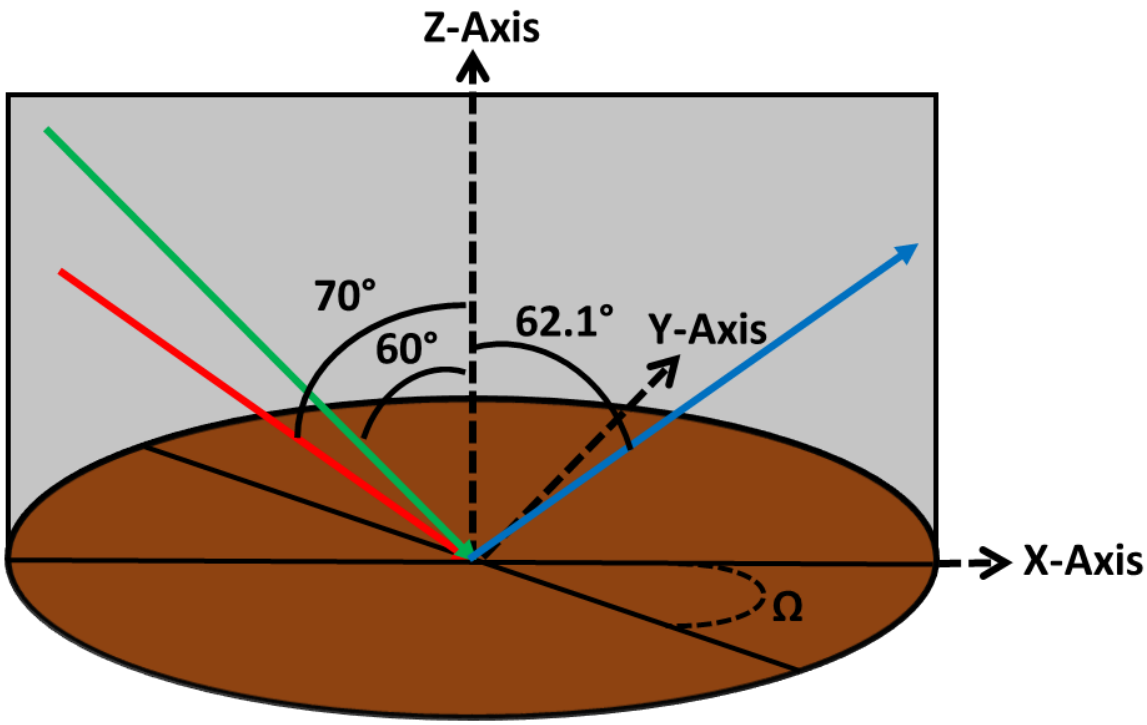

Figure 5-2: Schematic drawing of co-propagating SFG system.

5.4. Results and discussions

5.4.1. SFG imaging study on a microcrystalline copper surface

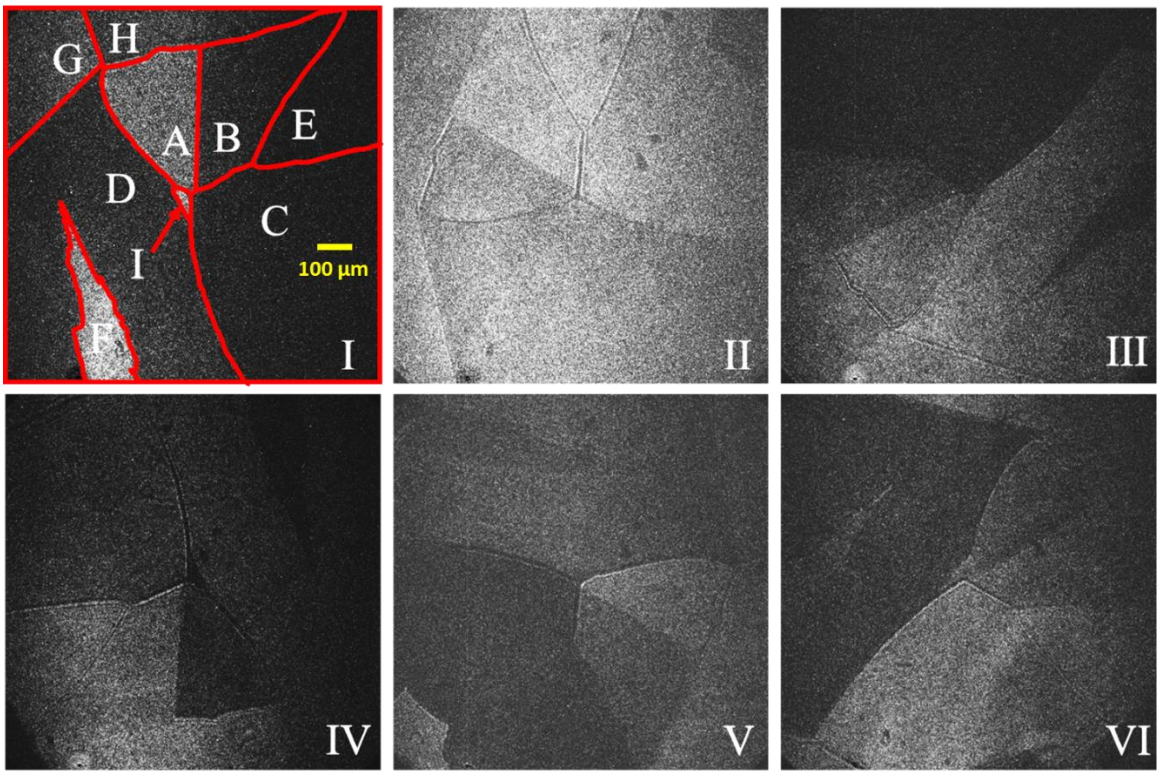

Figure 5-3. Unprocessed SFG image (IR wavenumber: 3050 cm^{-1}) of the copper surface with the ODT monolayer at the azimuth angle of 0° (I), 60° (II), 120° (III), 180° (IV), 240° (V), and 300° (VI), respectively. SFG images are taken with the PPP polarization. The red frame marks the GBs in I.

Figure 5-3(I-VI) show six SFG images at 3050 cm^{-1}, with azimuthal angles Ω varying from 0° to 300°. Since 3050 cm^{-1} is far from the resonant region of ODT molecular, the SFG intensity mainly comes from the copper substrate instead of the ODT molecule. Upon closer inspection, 9 domains with various sizes (50-300 µm), each with different SFG intensity, can be identified in the SFG image and are labeled in A-I. Based on previous studies,[33] such variation in the SFG intensity between different domains may be attributed to the variation of crystallographic orientation in each individual crystal domain on the copper surface. To confirm, EBSD measurement is performed to directly probe the local structure of such polycrystalline copper sample and is presented in Figure 5-4B. Comparing

the EBSD sand SFG image, it is evident that the brightness contrast of each domain area on SFG image correspond to different crystal grain structures as revealed by EBSD.

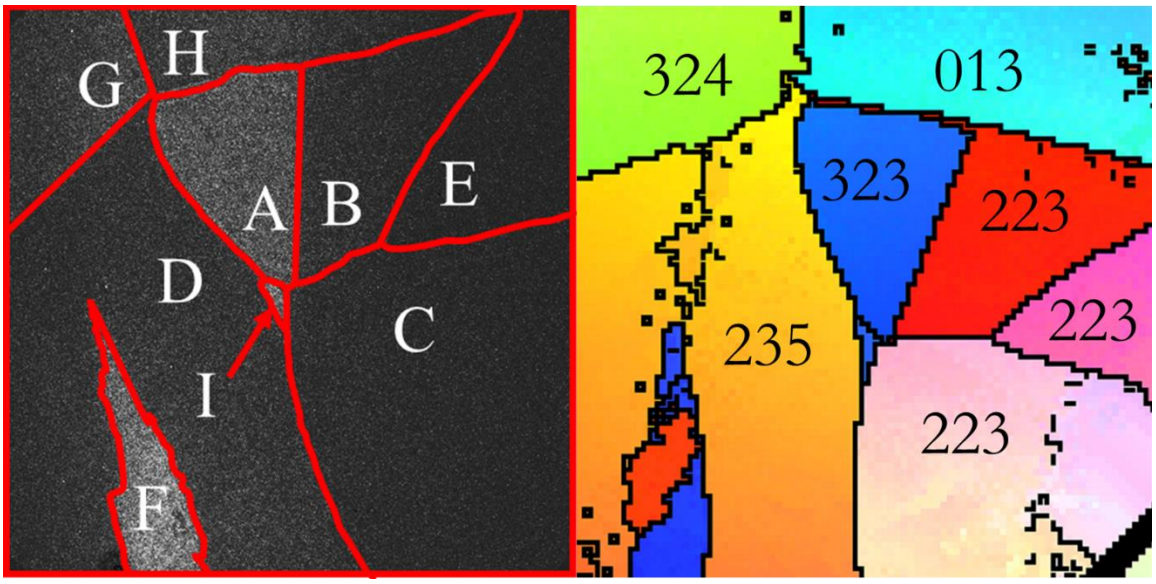

Figure 5-4: SFG image (left) and EBSD map (right) of copper surface with ODT self-assembled monolayer.

In addition, the SFG intensity of the crystalline domain areas contains azimuthal anisotropy with respect to the surface normal. Based on previous SFG studies, it is due to the anisotropy of SFG response on each individual crystal domain. To further analyze the intrinsic nature of such azimuthal anisotropy of SFG response in each individual crystal domain, a full range (0°-360°) of azimuthal angle measurements of SFG intensity of all 9 domains is performed with a step width of 20°. Figure 5-5 shows the azimuthal angle dependence on SFG intensity from domains 1 to 9. Each crystal domain contains a feature anisotropy pattern. These anisotropy patterns are observed at 3050 cm^{-1} where no peak corresponding to the ODT monolayer exists and only the non-resonant signal from the

copper substrate contributes to the SFG intensity. In principle, the anisotropy pattern is correlated only to the symmetry of the underneath local copper structure.

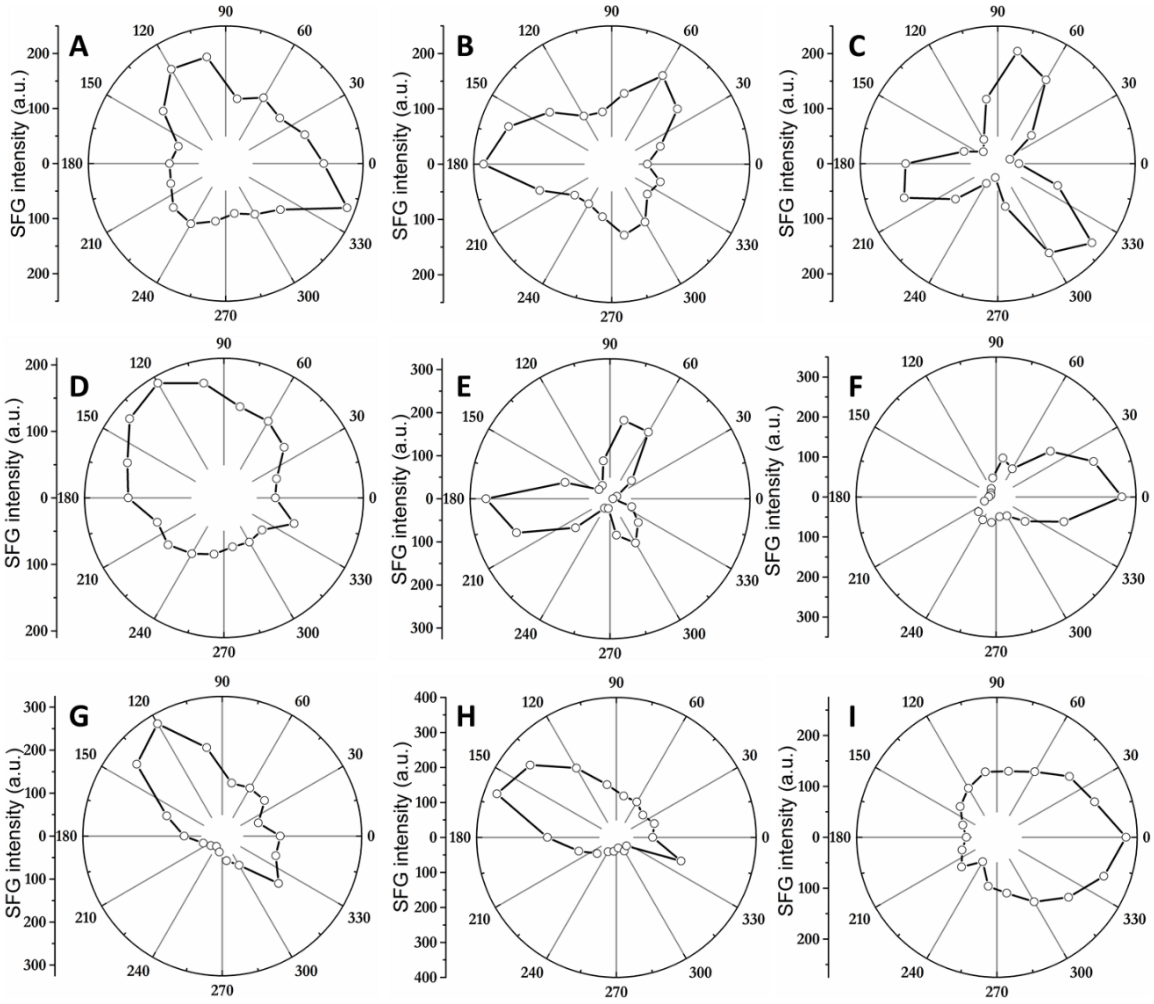

Figure 5-5: Non-resonant background radical map (3050 cm^{-1}) in 360 degree of azimuthal angle (step width: 20 degree) of the domains A-I as shown in Figure 5-3, respectively.

Figure 5-6 shows the local SFG spectra of domain C and domain D at two azimuthal angles, 80° and 140°, respectively. The three peaks observed around 2875, 2930, and 2960 cm^{-1} can be assigned to the symmetric stretching vibration, Fermi resonance, and the asymmetric stretching vibration of methyl group, respectively. Another two weak peaks locate around 2850 and 2910 cm^{-1} can be assigned to the symmetric stretching vibration

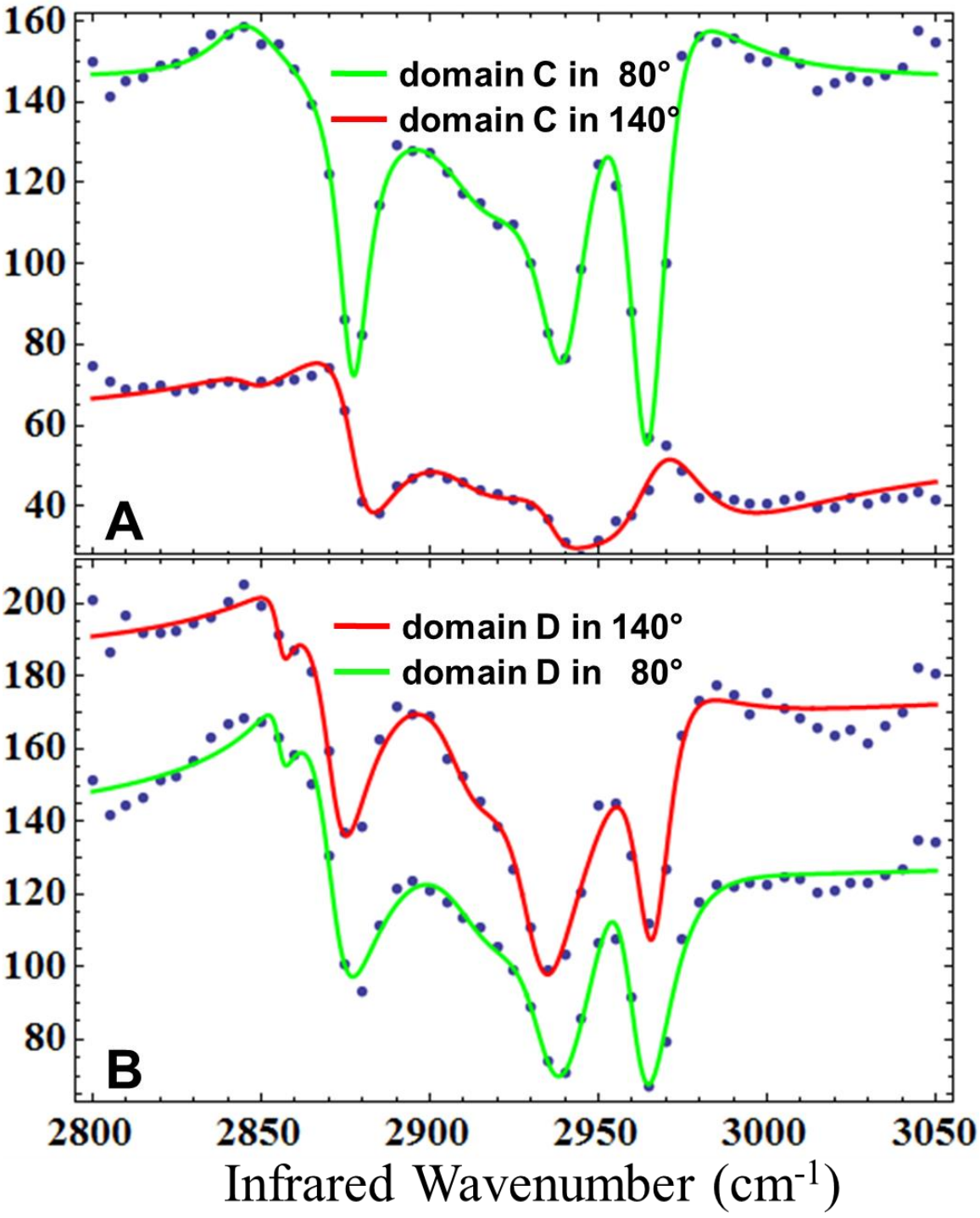

Figure 5-6. SFG spectra (2800-3050 cm^{-1}) of the copper surface with an ODT self-assembled monolayer at two azimuthal angles 80° and 140°. (A) and (B) represent the local SFG spectra of domain C and domain D from Figure 5-3, respectively. Solid lines are fitting line based on Equation 5-2.

and anti-symmetric stretching vibration of methylene groups, respectively. The spectral features, including the non-resonant background, peak intensity, and line-shape are dramatically different from these two crystal domains. This suggests that the interaction of the ODT monolayer with two individual crystal domains might be influenced by the Cu substrate. However, this effect is ambiguous, since the non-resonant contribution variation is significantly and strong enough to shift the SFG spectrum. Thus, the resonant contribution will be resolved by fitting the SFG spectrum.

Comparing Figure 5-6A with Figure 5-6B, the SFG spectrum varies from domain C to domain D, which reveals that the local heterogeneity varies on each crystal domains. Upon closer inspection, the SFG spectra also shows anisotropy. There are two possible causes for such SFG spectra anisotropy. The first reason could be attributed to the epitaxial arrangement of the monolayer induced by the underneath substrate structure. Such epitaxial arrangement includes bonding sites geometry,[27] methyl group symmetry,[28] and lateral structure.[21] Another possible cause would be that the anisotropy just exists on the substrate surface instead of adsorbed molecular. Rotation of the samples change the relative phase between the substrate and the monolayer contribution, which causes the cross term $2\left|\boldsymbol{\chi}_{NR}^{(2)}\right|\left|\boldsymbol{\chi}_{R}^{(2)}\right|\cos[\varepsilon-\delta]$ change, while these could make SFG spectra show anisotropy. Similar results were shown in Wang's SFG work about the monolayer on a quartz surface.[43] With rotation of the quartz substrate around the surface normal, strong azimuthal angle phase effects shift the line shape dramatically.

5.4.2. SFG spectra on Cu(111)

To elucidate the intrinsic mechanism for such anisotropy of SFG spectra, Cu(111) could serve as a reference sample since the surface atomic arrangement of Cu(111) is well defined. Figure 5-7 shows a series of SFG spectra for azimuthal angles varying from 0° to 90° on a Cu(111) surface covered with an ODT self-assembled monolayer. In comparison of these SFG spectra, the peak position and spectral line-shape, as well as non-resonant background strongly depend on the azimuthal angle. Due to the strong non-resonant signal

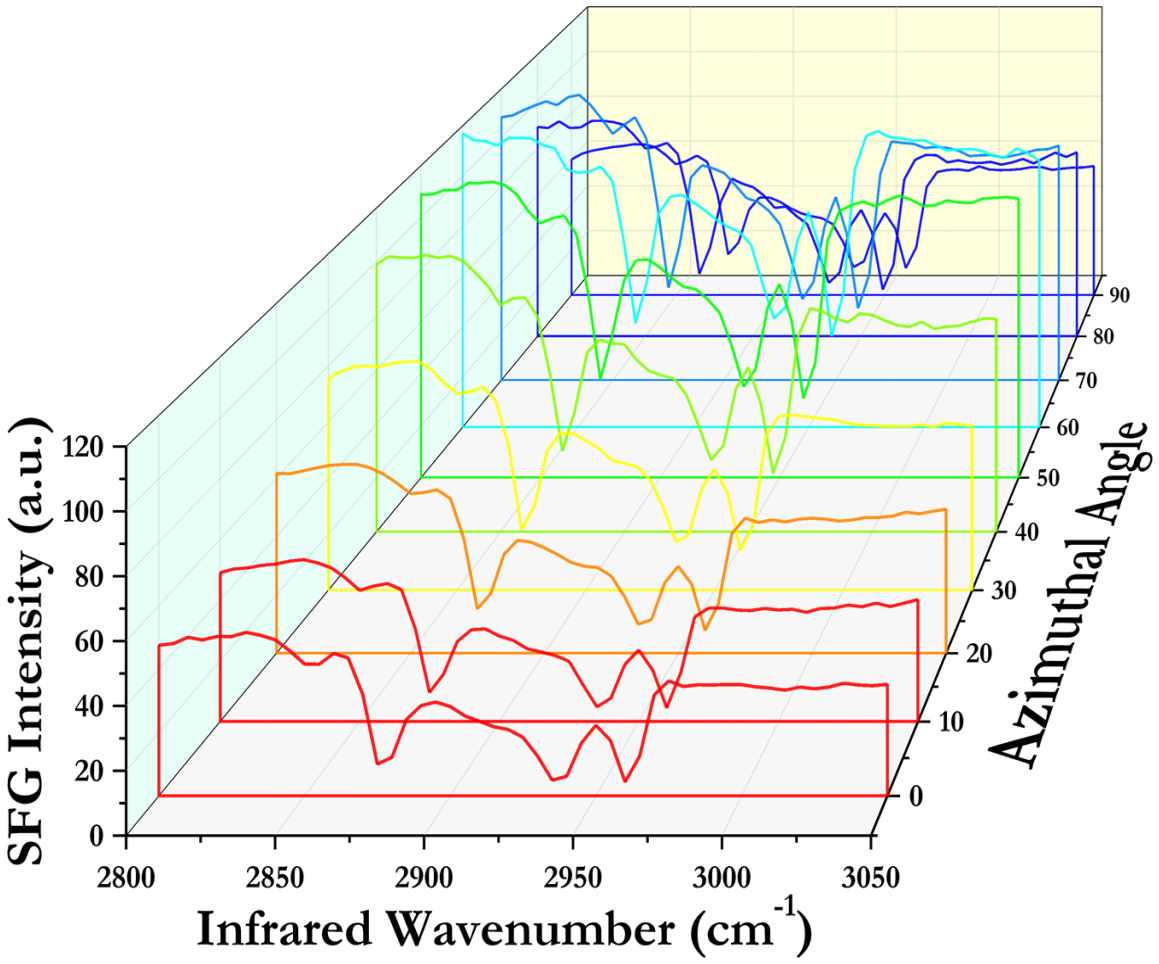

Figure 5-7. SFG spectra (2800-3050 cm^{-1}) of the Cu(111) surface with an ODT self-assembled monolayer for azimuthal angle varying from 0° to 90°.

results from the nearly free electrons in the metal surface, the resonant amplitudes for the methyl stretching mode could not be determined accurately.[44,45] It is necessary to extract the resonant contribution from the SFG spectra by fitting and compare it at the different azimuthal angles to analyze the monolayer epitaxial arrangement.

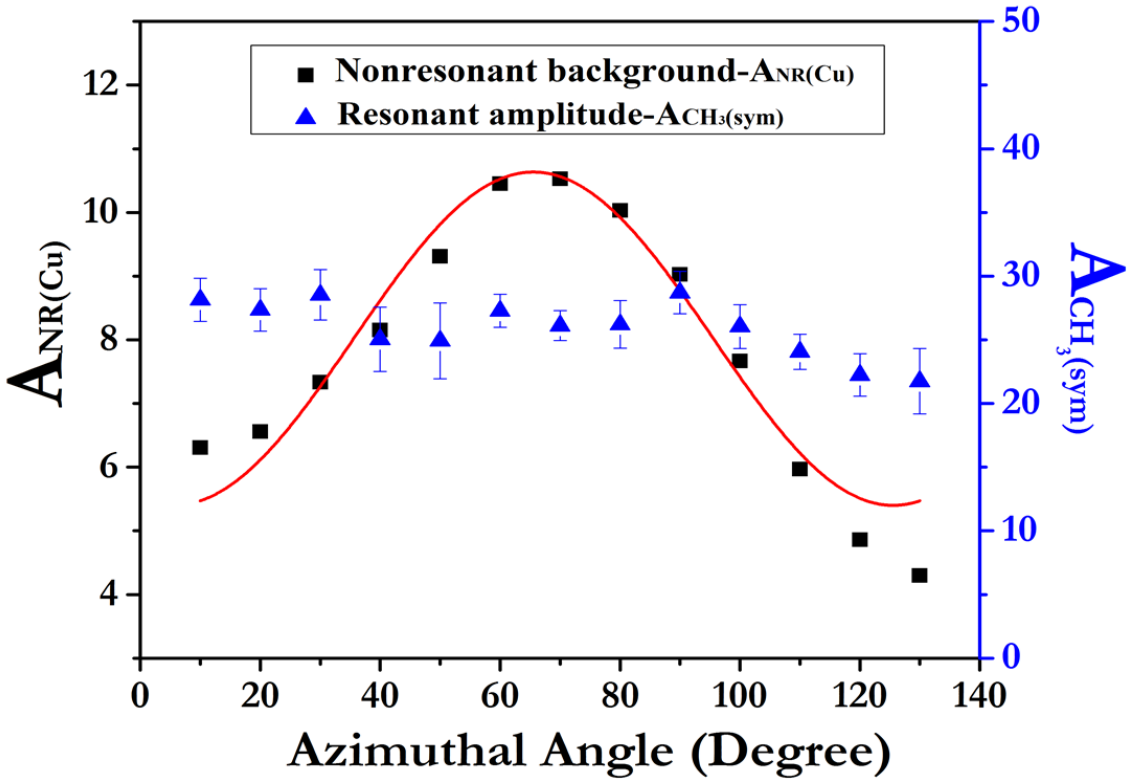

Figure 5-8. Nonlinear background and methyl symmetric stretching amplitude for azimuthal angles varying from 10° to 130°. The step width is 10°.

The symmetric stretching amplitude of the methyl group and non-resonant amplitude are obtained from the fitting to the series of SFG spectra in Figure 5-7 employing Equation 5-2 and plotted against the azimuthal angle as shown in Figure 5-8. The symmetric stretching amplitude of the methyl group is almost a constant from 10° to 130°, while the nonlinear background increases from 10° to the maximum at 70° and decreases

to the minimum at 130°. These observations suggest that symmetric stretching amplitudes of the methyl group shows no anisotropy response, which indicates that the molecular packing order is independent of the azimuthal angle.

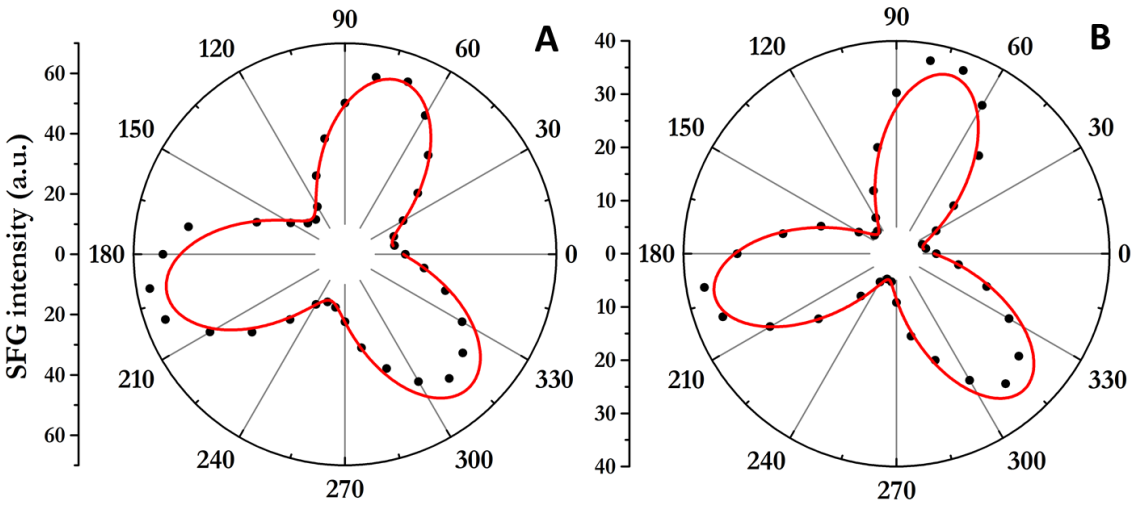

Figure 5-9. Rotational anisotropy of the SFG intensity from the ODT monolayer on Cu(111) at (A) 2880 cm^{-1}, (B) 3000 cm^{-1} monolayer. The solid red line shows the fitted curve to Equation 5-2.

Now let us compare the azimuthal angle dependencies of the SFG intensity, i.e., rotational anisotropy, at 2880 cm^{-1} (methyl symmetric stretching mode) and 3000 cm^{-1} (no peak). Figure 5-9 shows the SFG signal measured in the PPP polarization as a function of azimuthal angle at the step width of 20° for both 2880 cm^{-1} and 3000 cm^{-1}. Both the azimuthal angle dependencies of SFG intensity at 2880 cm^{-1} and 3000 cm^{-1} show a clear 3-fold symmetry. The 3-fold symmetry at 3000 cm^{-1} is observed where only the non-resonant component contributes to the SFG spectrum. A similar 3-fold symmetry shown from the SFG intensity at 2880 cm^{-1} might suggest the existence of lateral symmetry in the molecular assembly. The polar map is fitted by Equation 5-4 with the solid line.

$$I_{SF} = A \times [Sin(3\phi + \mathrm{B}) + C]^2$$ **Equation 5-2**

In which A and C are the isotropic and anisotropic contributions to the SFG intensity, respectively, and B is the phase correction. Fitting results are presented in Table 5-1. B values of 2880 cm^{-1} with 3000 cm^{-1} are very similar to each other, which denotes that the 3-fold symmetry at 2880 cm^{-1} is the same with the pattern at 3000 cm^{-1}. Such results preclude the possibility that the observed SFG anisotropy at 2880 cm^{-1} partially originates from the anisotropy of the orientation of the tilted alkyl chains. Because such possibility would give rise to an anisotropy pattern at 2880 cm^{-1} with an angle shift compared with 3000 cm^{-1}. Unless the distribution along the azimuthal angle of terminal methyl groups is taken to be a sum of three delta functions shifted by 120° in registry with underneath copper structure, and no torsional motion is allowed. Hence, for the present results, it indicates that the observed SFG anisotropy only results from the anisotropy of non-resonant signal.

Table 5-1. Fitting parameter for data in Figure 5-9

	A(a.u.)	B(rad)	C(a.u.)
2880 cm^{-1}	3.36	2.46	2.23
3000 cm^{-1}	3.53	2.48	3.13

In the present study, C_{3v} symmetry is assigned for the methyl group. There are 11 non-vanishing components for the second-order microscopic susceptibility, namely, β_{aac}, $\beta_{\mathrm{bb}c}$, β_{ccc}, β_{aca}, $\beta_{\mathrm{bc}b}$, β_{caa}, $\beta_{c\mathrm{bb}}$, β_{aaa}, $\beta_{\mathrm{bb}a}$, $\beta_{a\mathrm{bb}}$, $\beta_{\mathrm{ba}b}$.[46,47] For the r^+ mode,

there are three second-order microscopic susceptibilities, which is $\beta_{aac} = \beta_{\mathrm{bbc}}, \beta_{ccc}$. For the r⁻ mode, there are eight second-order microscopic susceptibilities.

$$\beta_{aca} = \beta_{\mathrm{bcb}}, \beta_{caa} = \beta_{\mathrm{cbb}}$$
$$\beta_{aaa} = -\beta_{\mathrm{bba}} = -\beta_{\mathrm{abb}} = -\beta_{\mathrm{bab}} \qquad \textbf{Equation 5-3}$$

It is reasonable to assume some degree of coupling between the monolayer with underlying copper structure. Therefore the monolayer epitaxial arrangement on microcrystalline surface is not isotropic. On the basis of this consideration, there are 8 non-vanishing macroscopic susceptibility components which is χ_{zzz} , χ_{xxz} , χ_{xzx} , χ_{zxx} , χ_{zxz} , χ_{xzz} , χ_{zzx} , and χ_{xxx} for the PPP polarization combination. So the effective amplitude of resonant mode can be written as:

$$\begin{aligned}\chi_{eff} = N_s[&F_{zzz}\langle\chi_{zzz}\rangle - F_{xxz}\langle\chi_{xxz}\rangle - F_{xzx}\langle\chi_{xzx}\rangle + F_{zxx}\langle\chi_{zxx}\rangle \\ &+ F_{zxz}\langle\chi_{zxz}\rangle - F_{xzz}\langle\chi_{xzz}\rangle + F_{zzx}\langle\chi_{zzx}\rangle - F_{xxx}\langle\chi_{xxx}\rangle]\end{aligned} \qquad \textbf{Equation 5-4}$$

Considering the incident angle and refractive indices on copper of SFG beam and 1064 beam are not much different, the Fresnel factors F_{zxx} and F_{xzx} are approximately the same, as well as F_{zxx} and F_{xzx} . Therefore, the third, fourth, fifth, and sixth term in Equation 5-4 cancel each other out. According to IR selection rules, only the vibrational modes with component positioned along the surface normal could be observed.[48,49] Besides that, the x, y component of IR electric field is always screened in the metal medium, so the F_{zzx} and F_{xxx} is approximately close to zero. To simplify the analysis, we consider only the nonzero elements which is the first and second term as follows:

$$\chi_{eff} = N[F_{zzz}\langle\chi_{zzz}\rangle - F_{xxz}\langle\chi_{xxz}\rangle] \qquad \textbf{Equation 5-5}$$

For the symmetric stretching vibrational mode,

$$\begin{aligned}\chi_{eff,r^+} &= N_s[F_{zzz}\langle\chi_{zzz}\rangle - F_{xxz}\langle\chi_{xxz}\rangle] \\ &= \frac{1}{2}N_s[\beta_{ccc}\langle\cos\theta\rangle + \beta_{aac}\langle\cos\theta\rangle - \beta_{ccc}\langle\cos^3\theta\rangle + \beta_{aac}\langle\cos^3\theta\rangle] \\ &+ N_s[\beta_{aac}\langle\cos\theta\rangle + \beta_{ccc}\langle\cos^3\theta\rangle - \beta_{aac}\langle\cos^3\theta\rangle]\end{aligned} \qquad \textbf{Equation 5-6}$$

For the asymmetric stretching vibrational mode,

$$\begin{aligned}\chi_{eff,r^-} &= N_s[F_{zzz}\langle\chi_{zzz}\rangle - F_{xxz}\langle\chi_{xxz}\rangle] \\ &= \frac{1}{2}N_s[\beta_{ccc}\langle\cos\theta\rangle + \beta_{aac}\langle\cos\theta\rangle - \beta_{ccc}\langle\cos^3\theta\rangle + \beta_{aac}\langle\cos^3\theta\rangle] \\ &+ N_s[\beta_{aac}\langle\cos\theta\rangle + \beta_{ccc}\langle\cos^3\theta\rangle - \beta_{aac}\langle\cos^3\theta\rangle]\end{aligned} \qquad \textbf{Equation 5-7}$$

Inspection of above analysis, as expected, no azimuthal anisotropy of the symmetric stretching vibrational mode and asymmetric stretching vibrational mode is calculated for the methyl group on metal surface. The reason for the disappearance of the anisotropy is the enhanced electric field which is normal to the surface, while the parallel component of electric field is screened due to the boundary conditions of the electric field on metal surface.[44,50] That makes the effective IR transition diploe for the symmetric stretching and anti-symmetric stretching mode orient along the surface normal. Hence, an azimuthal isotropy of methyl group is observed, regardless of isotropic random azimuthal orientation or locked orientation corresponding with copper substrate existing in the monolayer. Previous SFG calculation works on metal surface also proved that the isotropic tensor component $F_{zzz}\langle\chi_{zzz}\rangle$ dominate the SFG signal on metal surface.[51] Vice versa, SFG

measurement is indeterministic whether there has the specific epitaxial arrangement in the monolayer on metal surface; however, the orientation angle information could be reliably and unambiguously determined from spectral fitting. Considering metal surface always contributes a very large screen effect to the electric field parallel to the metal surface, this conclusion is able to apply on all the monolayer on metal surface.

Previously, Uosaki et al. reported the presence of 3-fold anisotropy of SFG intensity during the resonant region of adsorbed octadecyl monolayer formed on a hydrogen-terminated Si (111) surface. They suggested that such 3-fold anisotropy were due to the 3-fold epitaxial arrangement of the monolayer on silicon substrate.[21] Since the silicon is a semiconductor material with relative low electric conductivity, the screen effect to the electric field parallel with the surface from silicon substrate is not as strong as copper. Besides that, the ordered lateral structure is easier to form on silicon surface due to the existence of more defects and oxidation on copper. In general, the lateral order of monolayer is easily revealed on silicon surface instead of copper surface.

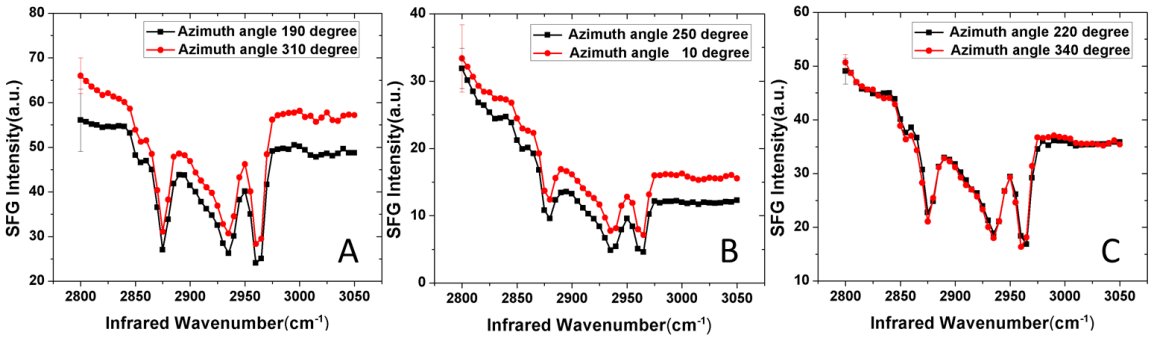

Figure 5-10. The comparison of SFG spectra in different azimuthal angle for A (190° and 310°); B (250° and 10°); C (220° and 340°)

Figure 5-10 shows the SFG spectra measurement at 10°, 250° in Figure 5-10A; 220° and 340° in figure 5-10B, 190° and 310° in Figure 5-10C. There has a 3-fold symmetry in

the surface structure of Cu (111). Since the SFG signal could be regards as the interference between monolayer with underneath copper substrate. In general, epitaxial arrangement in the molecular packing would break such 3-fold symmetry of SFG response. However, there does not show any difference on the SFG spectra between 10° with 250°, 220° with 340°, as well as 190° with 310°. That proves previous statement that no SFG anisotropy response will be evidently shown up even there has a clear epitaxial arrangement in the molecular packing.

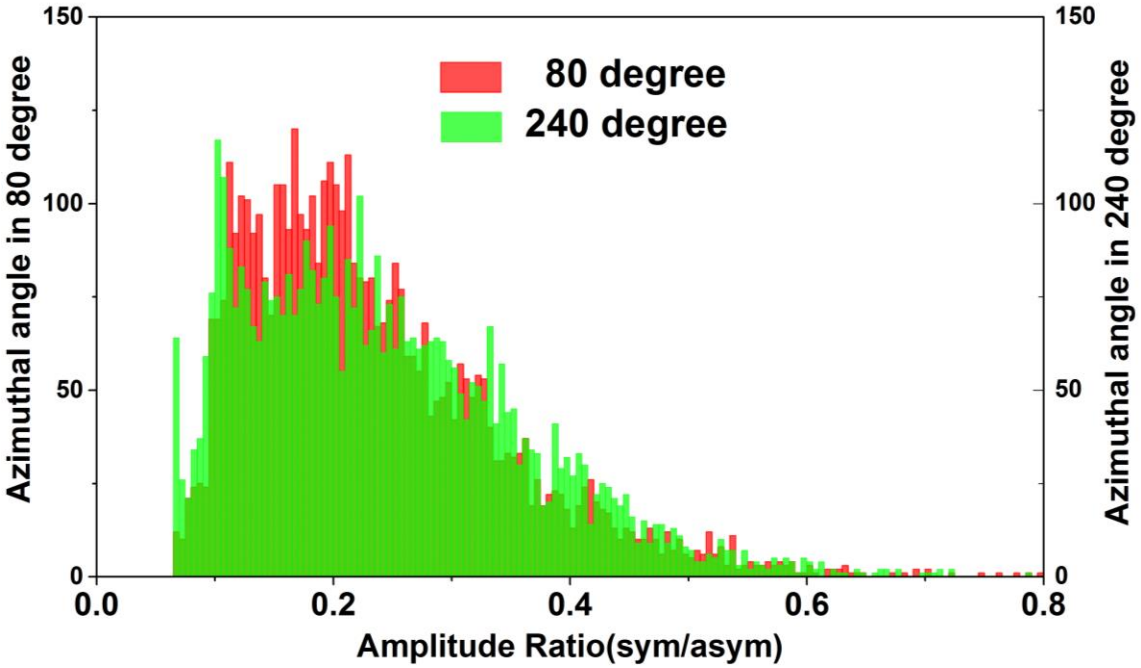

Figure 5-11. Histogram of amplitude ratios ($CH_{3\text{-sym}}/CH_{3\text{-asym}}$) of methyl group on copper with azimuthal angle 80° (red) and 240° (red), respectively.

To further elucidate whether the resonant amplitude of the molecular is dependent of the azimuthal angle, the evaluation of SFG imaging data of methyl group on copper with azimuthal angle 80° and 240° is carried out by employing statistical methods represented in the form of histogram distributions. Comparing these two histograms of amplitude ratio

in Figure 5-11, the ratio distribution keeps consistent when the ratio distribution shifts from 80° to 240°. That can be understood because azimuthal angle transformation could not influence the local spectrum interpretation about the conformation order of monolayer. Therefore, the interpretation of SFG spectrum is isolated from the azimuthal angle. As long as the fitting parameter are reliable, the molecular conformation order of molecular at different crystal domain could be deduced and compared. That provides tremendous new information on the structure and interactions of these molecular at a given crystal grain. It also demonstrates unique power of SFG imaging that need to be further explored in surface chemistry study on metal surface.

5.4.3. Tilt angle of methyl group and histogram analysis

A representative SFG image (2980 cm^{-1}) with azimuthal angle 80° is shown in Figure 5-12A, with the corresponding EBSD image of the same area in Figure 5-12B. Four domains, each with different crystal index, can be identified in the SFG image and EBSD image, and are labeled in Figure 5-12A (1-4). Comparing the EBSD and SECCM maps, it is more evident that the regions of distinctly different SFG signal correspond to particular grain structure by EBSD shown in Figure 5-12 B. To elucidate monolayer heterogeneity in different crystal domain, the evaluation of SFG imaging data from the SAMs monolayer on such copper surface is carried out by employing statistical methods represented in the form of spatial (contour maps) and histogram distributions. In Figure 5-12C, the fitted results of the amplitude ratio ($CH_{3\text{-}sym}/CH_{3\text{-}asym}$) is mapped onto the surface coordinates to visualize differences in spatial distribution for the copper surface. Upon closer inspection of the histogram of amplitude ratio in Figure 5-12C, each regions owns its feature ratio

distribution, which suggests that the underneath grain structure on copper surface would dramatically influence molecules packing behavior which cause the orientation angle

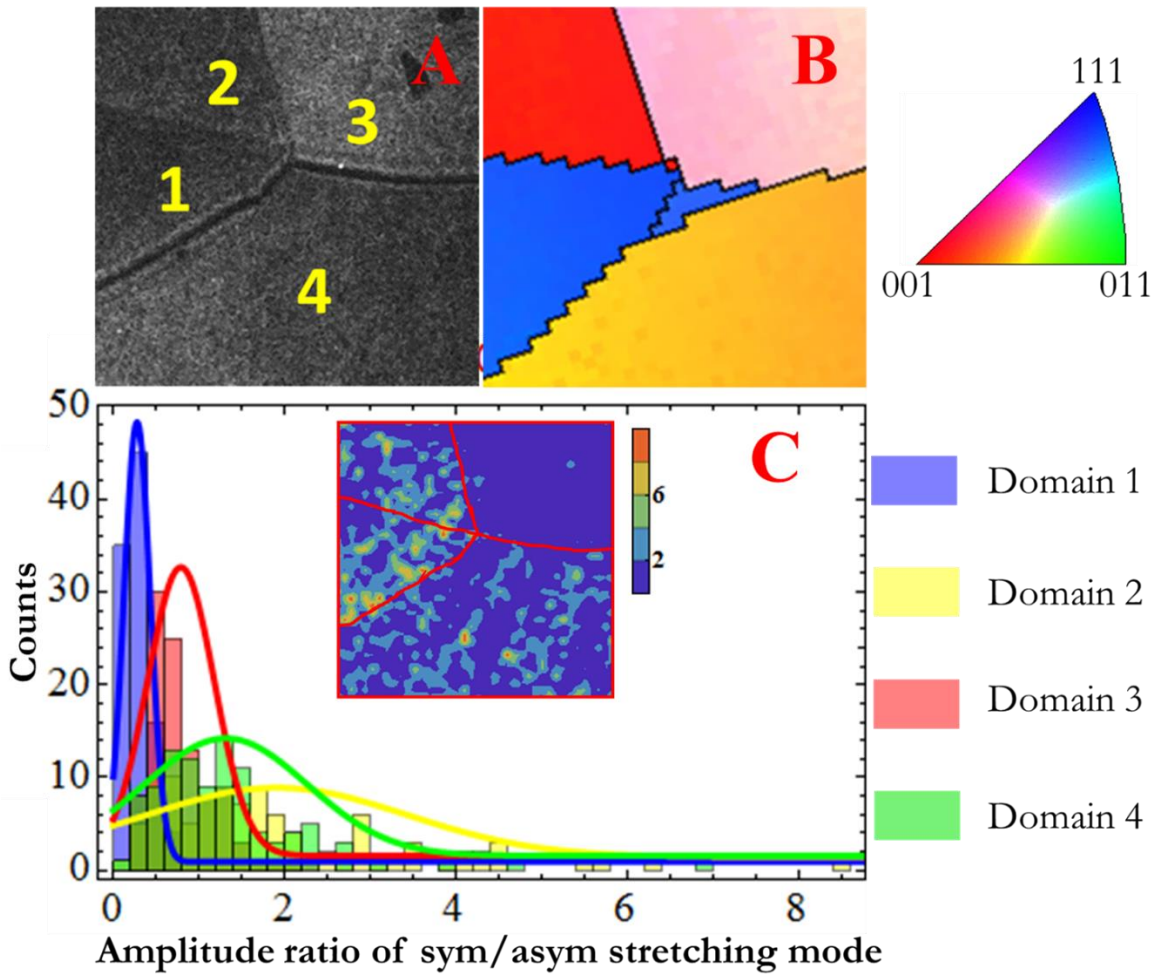

Figure 5-12. (A) Representative SFG image (2980 cm^{-1}) of ODT on microcrystalline copper surface with azimuthal angle 80°. (B) Corresponding EBSD map with the color coded orientation map of the scanned area. (C) Corresponding histogram and contour map of amplitude ratios ($CH_{3\text{-}sym}/CH_{3\text{-}asym}$) of methyl group on copper with azimuthal angle 80°.

varies in different regions. These structure dependent relative conformation order is evident and highlights that on polycrystalline copper surface, the molecular packing behavior is strongly structure dependent at the microscopic level. Similar observation has already been confirmed by other similar studies on copper surface.[52-55]

5.4.4. Non-resonant response of the copper

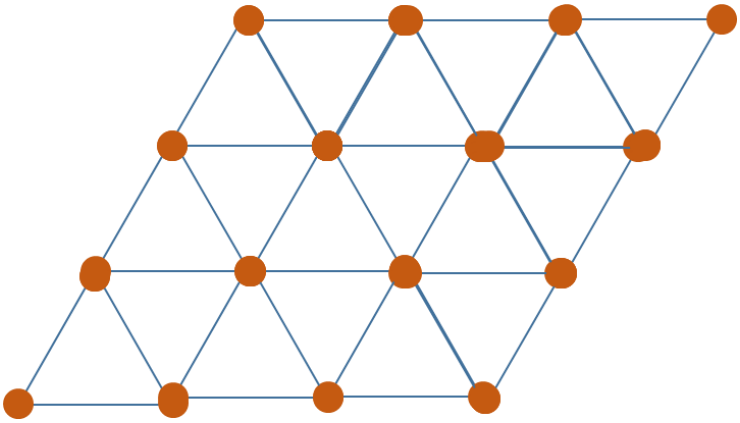

Figure 5-13. Surface structure of Copper (111).

A phenomenological macroscopic theory of the second harmonic generation electronic response from the cubic centrosymmetric crystal surface have been developed by Sipe et al.[56] The effective second order polarization from copper contains both contributions from the surface and bulk medium. Both contribution has isotropic and anisotropic components, based on the crystal symmetry of copper substrate. In the bulk medium of centrosymmetric materials such as copper, the second order dipole response is equal to zero. The SFG/SHG signal could arise from higher order nonlinear sources with electric quadrupole or magnetic dipole symmetry. While the surface contribution to the SFG signal is primarily dipolar since the inversion symmetry is broken on surface.[28] The contribution arises from a few nanometer within the escape depth of the light radiation. Consequently, the surface and bulk contributions can be comparable which cause the signal composition complicated. In general, it is not possible to separate out the surface and bulk effects for cubic centrosymmetric materials. However, the anisotropy of SFG intensity, which is the result of interference of bulk with surface, is quite discernible. Figure 5-12

presents the surface structure on Cu (111). Thus if the first layer of copper atom on Cu (111) into account, the symmetry is C_{6v}; however, the symmetry lowers to the C_{3v} if additional one atomic layer from Cu (111) was taken into account.

The second order polarization vector can be split into its components perpendicular and parallel to the surface. The former is sensitive, to the interfacial electric field and the latter probes the rotational symmetric of the sample surface.[57] Thus different polarization combination would present different anisotropy pattern.

Besides that, it is need to be mentioned that in optically flat metal surfaces, there exist many local nanometer size structures, such as terrace, step, and defects, which have been observed by probe scanning microscopy.[19,20] In such cases, the microscopic symmetry of the structures, would allow some specific tensor elements to exist. If the domains consists of these structure are smaller than the spot size of the laser radiation, there would be a "superposition" of the symmetries. That is, we may observe a lower symmetry than expected if the newly introduced tensor is of different symmetry.[58]

In principle, quantitative assignment of second order susceptibility tensor elements being responsible for anisotropy pattern in different polarization combination is beyond the scope of this report. Nevertheless, this works provides a reliable framework to analyze the local SFG spectra highly affected by the underneath crystal structure. That is the power of SFG imaging that need to be explored in the future studies.

5.5. Conclusions

In conclusion, the structure of an ODT monolayer formed on a microcrystalline copper was studied by the combination of the SFG microscopy, EBSD and SHG. SFG imaging technique provide detailed information and understanding of the molecular composition, orientation and conformation order of adsorbed monolayer on the surface through quantitative measurement and analysis of SFG images. Clear domain structure with obvious brightness contrast revealed in the SFG images demonstrate grain structure existed on copper surface, and confirmed by corresponding EBSD image. The azimuthal angle cause the spectra phase shift which cause the anisotropy of SFG spectra in different azimuthal angle. Besides that, the anisotropy SFG response on each grain is different between each copper facet which reveals the heterogeneity of SAMs monolayer on various crystal grain was revealed in the SFG images suggested that the underneath structure influence the molecular behavior of adsorbed monolayer.

Resonant contribution was separated from the SFG spectrum and confirmed as a constant as the rotational angle varies from 0 degree to 120 degree. The analysis of the SFG spectral profiles, we have shown for the first time that the contribution from the ZZZ component of the resonant nonlinear susceptibility is dominant in the observed resonant signals. The dependence of the phase angle on the azimuthal angle was different between the resonant and the non-resonant contributions, because the phase angle for the non-resonant part of the nonlinear polarization is composed of the sum of all <ijk> components whereas only ZZZ component for the resonant part. These observation is of major fundamental importance for SFG data analysis on metal surface toward a better understanding of heterogeneous catalysis and corrosion research in future.

5.6. References

(1) Ulman, A. *Chem. Rev.* **1996**, *96*, 1533.

(2) Krämer, S.; Fuierer, R. R.; Gorman, C. B. *Chem. Rev.* **2003**, *103*, 4367.

(3) Love, J. C.; Estroff, L. A.; Kriebel, J. K.; Nuzzo, R. G.; Whitesides, G. M. *Chem. Rev.* **2005**, *105*, 1103.

(4) Poirier, G. E. *Chem. Rev.* **1997**, *97*, 1117.

(5) Zhao, J.; Moretto, J.; Le, P.; Franzen, S. *J. Phys. Chem. B* **2015**, *119*, 2827.

(6) Qiao, L.; Ge, A.; Liang, Y.; Ye, S. *J. Phys. Chem. B* **2015**, *119*, 14188.

(7) Li, Z.; Weeraman, C. N.; Gibbs-Davis, J. M. *J. Phys. Chem. C* **2014**, *118*, 28662.

(8) He, X.; Wu, C.; Rajagopal, K.; Punpongjareorn, N.; Yang, D. S. *Phys. Chem. Chem. Phys.* **2016**.

(9) Porter, M. D.; Bright, T. B.; Allara, D. L.; Chidsey, C. E. *J. Am. Chem. Soc.* **1987**, *109*, 3559.

(10) Laibinis, P. E.; Whitesides, G. M.; Allara, D. L.; Tao, Y. T.; Parikh, A. N.; Nuzzo, R. G. *J. Am. Chem. Soc.* **1991**, *113*, 7152.

(11) Bourg, M.-C.; Badia, A.; Lennox, R. B. *J. Phys. Chem. B* **2000**, *104*, 6562.

(12) Bain, C. D.; Biebuyck, H. A.; Whitesides, G. M. *Langmuir* **1989**, *5*, 723.

(13) Bain, C. D.; Troughton, E. B.; Tao, Y. T.; Evall, J.; Whitesides, G. M.; Nuzzo, R. G. *J. Am. Chem. Soc.* **1989**, *111*, 321.

(14) He, X.; Wang, Y.; Yang, Z.; Ma, Y.; Yang, Y. *Appl. Phys. B* **2010**, *100*, 773.

(15) He, X.; Wang, Y.; Liu, W.; Yang, Z.; Du, X.; Liu, Y.; Yang, Y. *Chem. Phys. Lett.* **2011**, *502*, 184.

(16) Yamada, R.; Uosaki, K. *Langmuir* **1997**, *13*, 5218.

(17) Bumm, L.; Arnold, J.; Charles, L.; Dunbar, T. D.; Allara, D.; Weiss, P. *J. Am. Chem. Soc.* **1999**, *121*, 8017.

(18) Laibinis, P. E.; Whitesides, G. M. *J. Am. Chem. Soc.* **1992**, *114*, 9022.

(19) Casero, E.; Darder, M.; Pariente, F.; Lorenzo, E.; Martín-Benito, J.; Vázquez, L. *Nano Lett.* **2002**, *2*, 577.

(20) O'Dwyer, C.; Gay, G.; Viaris de Lesegno, B.; Weiner, J. *Langmuir* **2004**, *20*, 8172.

(21) Nihonyanagi, S.; Miyamoto, D.; Idojiri, S.; Uosaki, K. *J. Am. Chem. Soc.* **2004**, *126*, 7034.

(22) Aaronson, B. D.; Chen, C.-H.; Li, H.; Koper, M. T.; Lai, S. C.; Unwin, P. R. *J. Am. Chem. Soc.* **2013**, *135*, 3873.

(23) Martinez-Lombardia, E.; Maurice, V.; Lapeire, L.; De Graeve, I.; Verbeken, K.; Kestens, L.; Marcus, P.; Terryn, H. *J. Phys. Chem. C* **2014**, *118*, 25421.

(24) Lapeire, L.; Martinez Lombardia, E.; Verbeken, K.; De Graeve, I.; Kestens, L. A. I.; Terryn, H. *Corros. Sci.* **2013**, *67*, 179.

(25) Climent, V.; Feliu, J. M. *J. Solid State Chem.* **2011**, *15*, 1297.

(26) Koper, M. T. *Nanoscale* **2011**, *3*, 2054.

(27) Yeganeh, M.; Dougal, S.; Polizzotti, R.; Rabinowitz, P. *Phys. Rev. Lett.* **1995**, *74*, 1811.

(28) Malyk, S.; Shalhout, F. Y.; O'Leary, L. E.; Lewis, N. S.; Benderskii, A. V. *J. Phys. Chem. C* **2013**, *117*, 935.

(29) Martinez-Lombardia, E.; Gonzalez-Garcia, Y.; Lapeire, L.; De Graeve, I.; Verbeken, K.; Kestens, L.; Mol, J. M. C.; Terryn, H. *Electrochim. Acta* **2014**, *116*, 89.

(30) Cimatu, K.; Baldelli, S. *J. Am. Chem. Soc.* **2006**, *128*, 16016.

(31) Hedberg, J.; Leygraf, C.; Cimatu, K.; Baldelli, S. *J. Phys. Chem. C* **2007**, *111*, 17587.

(32) Cimatu, K.; Baldelli, S. *J. Am. Chem. Soc.* **2008**, *130*, 8030.

(33) Fang, M.; Baldelli, S. *J. Phys. Chem. Lett.* **2015**, *6*, 1454.

(34) Shen, Y. R. *Proc. Natl. Acad. Sci.* **1996**, *93*, 12104.

(35) Bain, C. D. *J. Chem. Soc. Faraday Trans.* **1995**, *91*, 1281.

(36) Buck, M.; Himmelhaus, M. *J. Vac. Sci. Technol. A* **2001**, *19*, 2717.

(37) Shen, Y. R. *Nature* **1989**, *337*, 519.

(38) Zhu, X.; Suhr, H.; Shen, Y. *Phys. Rev. B* **1987**, *35*, 3047.

(39) Zhuang, X.; Miranda, P.; Kim, D.; Shen, Y. *Phys. Rev. B* **1999**, *59*, 12632.

(40) Harris, A. L.; Chidsey, C. E. D.; Levinos, N. J.; Loiacono, D. N. *Chem. Phys. Lett.* **1987**, *141*, 350.

(41) Cimatu, K. A.; Baldelli, S. *J. Phys. Chem. C* **2009**, *113*, 16575.

(42) Fang, M.; Santos, G.; Chen, X.; Baldelli, S. *Surf. Sci.* **2015**, 648, 35.

(43) Fu, L.; Chen, S. L.; Wang, H. F. *J. Phys. Chem. B* **2015**.

(44) Superfine, R.; Guyot-Sionnest, P.; Hunt, J.; Kao, C.; Shen, Y. *Surf. Sci.* **1988**, *200*, L445.

(45) Harris, A.; Chidsey, C.; Levinos, N.; Loiacono, D. *Chem. Phys. Lett.* **1987**, *141*, 350.

(46) Shen, Y. R. Principles of nonlinear optics. Wiley: **1984**.

(47) Hirose, C.; Akamatsu, N.; Domen, K. *Appl. Spectrosc.* **1992**, *46*, 1051.

(48) Fan, J.; Trenary, M. *Langmuir* **1994**, *10*, 3649.

(49) Greenler, R. G. *J. Chem. Phys.* **1966**, *44*, 310.

(50) Miragliotta, J.; Polizzotti, R.; Rabinowitz, P.; Cameron, S.; Hall, R. *Chem. Phys.* **1990**, *143*, 123.

(51) Tanaka, Y.; Lin, S.; Aono, M.; Suzuki, T. *Appl. Phys. B Lasers O* **1999**, *68*, 713.

(52) Jones, D. A. *Principles and prevention of corrosion*; Macmillan, **1992**.

(53) Roberge, P. R. *Corrosion engineering: principles and practice*; McGraw-Hill New York, **2008**.

(54) Cimatu, K.; Baldelli, S. *J. Phys. Chem. C* **2007**, *111*, 7137.

(55) Santos, G. M.; Baldelli, S. *J. Phys. Chem. C* **2013**, *117*, 17591.

(56) Sipe, J.; Moss, D.; Van Driel, H. *Phys. Rev. B* **1987**, *35*, 1129.

(57) Pettinger, B.; Bilger, C.; Lipkowski, J.; Schmickler, W. *Second Harmonic Generation Anisotropy from Single Crystalline Electrode Surfaces*; Marcel Dekker, Inc.: New York, **1999**.

(58) Yamada, C.; Kimura, T. *Phys. Rev. B* **1994**, *49*, 14372.

CHAPTER 6. Chemical Mapping of CO Adsorption on a Polycrystalline Platinum Surface Investigated by Sum Frequency Generation Microscopy

6.1. Introduction

The gas/metal interface is ubiquitous in ambient chemical process such as corrosion and gas catalysis.[1] The identification of gas adsorption and reaction dynamics on metal surface under ambient pressure is of critical importance, because most reactions are performed at ambient pressure. The carbon monoxide(CO) adsorption on platinum has been extensively studied since the early work of Langmuir,[2,3] served as a model system to study various aspects of structure and bonding of adsorbed molecules at transition metal surface.[4] As an excellent catalyst associated with the oxidation of H_2, and CO at room temperature,[5,6] a more comprehensive understanding of CO adsorption on platinum is very important at ambient pressure condition. Meanwhile the different crystal grains of platinum have been reported to exhibit remarked anisotropies for adsorption of simple molecular.[7] It is apparent that the adsorption characteristics and binding state of the reactants vary on the heterogeneous platinum surface, and this may significantly affects the catalytic dynamics of the reaction.[8] However, a fundamental understanding of these heterogeneous effects is still lacking. Chemical and spatial mapping the CO adsorption on polycrystalline platinum is essential to elucidate the CO molecular behavior on heterogeneous platinum surface.[8]

Various methods such as Photoelectron Spectroscopy(PES),[6,9] Infrared Reflection-Adsorption Spectroscopy(IRAS),[10] Low Energy Electron Diffraction(LEED),[11] Temperature Programmed Desorption(TPD)[12] have been developed to detect the CO molecular adsorption on platinum surface with varied atom surface information. The PES used in the imaging mode of Photoemission Electron Microscopy (PEEM)[12] technique combined with Scanning Tunneling Microscopy (STM)[13] provide varying degrees of spatial, temporal, and chemical resolution of surface. However, most of these techniques could be only performed on well-defined surface in Ultra-High Vacuum (UHV) systems. Only a few complete surface reaction mechanisms have been derived which are mainly based on studying system carried out under UHV condition (pressure gap).[14] Thus modeling of technical processes which usually take place under ambient pressure emphasizes the importance of developing diagnostic techniques for molecular level study of adsorbed species under practical catalytic condition.

SFG as a laser spectroscopic technique which is able to overcome pressure gap has been used to investigate the CO adsorption on platinum for more than three decades.[14-19] Based on previous SFG and IRAS results, CO molecular linear bonded to one platinum atom has the vibrational frequency of 2040-2010 cm^{-1}. CO coordinated to two or three platinum atoms has the vibrational frequency of 1840-1800 cm^{-1} and 1750-1700 cm^{-1}, respectively.[20] On the polycrystalline platinum surface, only linear bonded CO could be observed.[4,21] The linear bonded CO stretching frequency is dramatically influenced by several factors include temperature,[19] CO pressure,[17] surface coverage, dipole-dipole coupling,[16] different sites[14] (kinks, steps, and terraces) as well as different surface crystal plane.[16] The SFG resonant intensity is proportional to the CO surface coverage.[14,18] For the

disorder polycrystalline platinum surface, lineally bonded configuration CO is more likely to adsorb on the step site (vibrational frequency locates around 2065-2078 cm^{-1}) than terrace site (vibrational frequency around 2086-2097 cm^{-1}) when the surface coverage is low.[10] While SFG technique cannot provide the heterogeneous surface information due to measuring an average response over the probe local area. This work aims at a characterization of CO stretching vibration on the polycrystalline platinum surface via SFG imaging to get a better understanding CO adsorption on heterogeneous platinum surface.

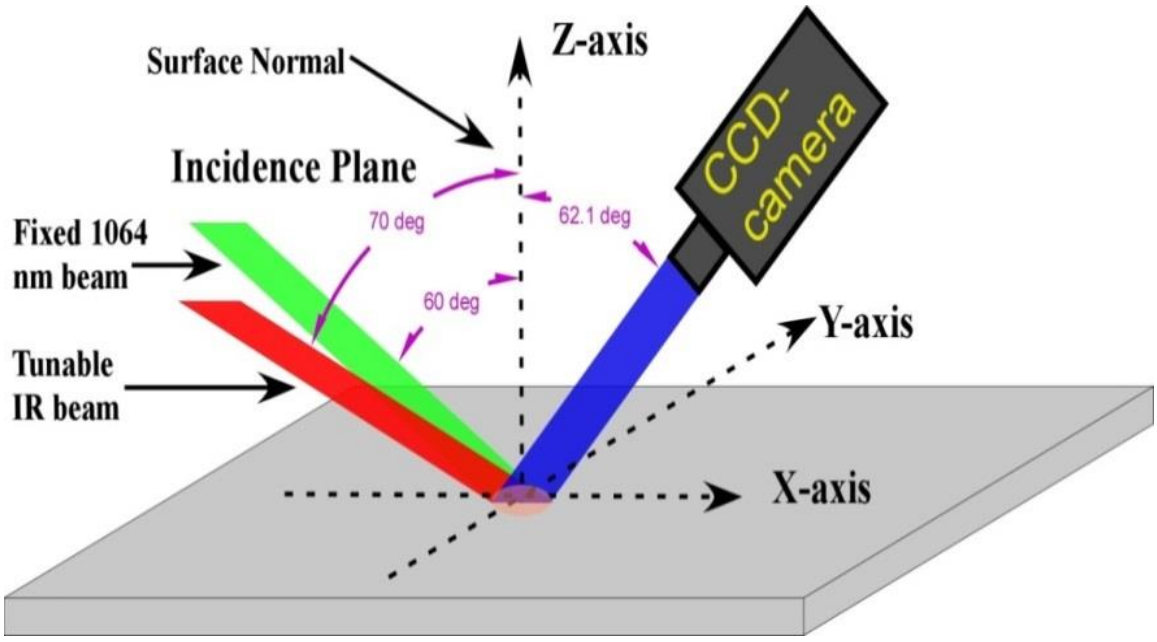

Figure 6-1: Schematic diagram of SFG imaging.

Generally gas adsorption on metal is very fast in the ambient pressure. Take a nitrogen/solid system in 300 K for example; suppose the nitrogen stick coefficient is 1 and surface atom density is $10^{15}/cm^2$, it takes 10 ns to form monolayer on surface if nitrogen pressure is 1 atm. Even the nitrogen pressure is lowered down to 10^{-6} Torr, monolayer formation time is about 3 seconds.[22] Thus developing a UHV-SFG-Imaging system is

essential to the research of CO adsorption on platinum which prepare a clean platinum surface (impurity coverage ≤ 1%) in UHV, free from common atmospheric contaminants before ambient pressure CO gas is introduced.

6.2. Theory background

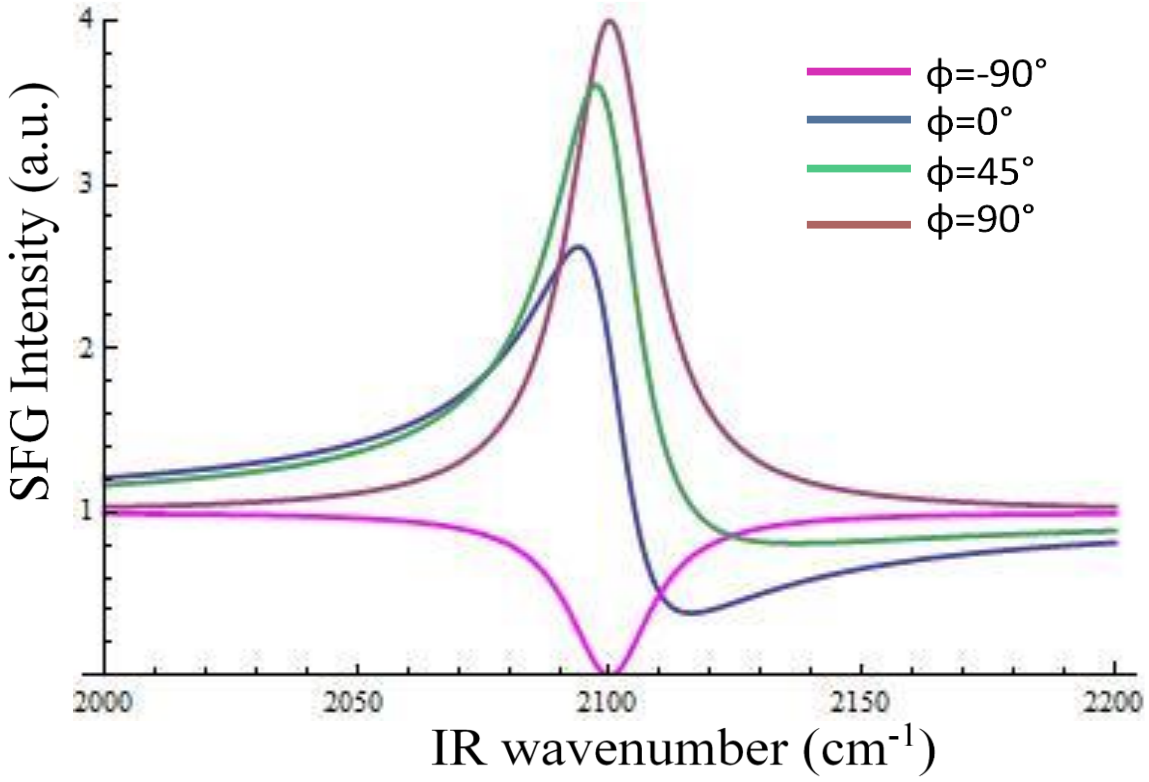

Figure 6-2: Simulation of a SFG spectrum line shape with relative phase shift (ϕ) shown in Equation 2-12 is equal to -90°, 0°, 45°, 90°, which a single resonance at 2100 cm^{-1}.

SFG is a second-order nonlinear optical process in which a tunable infrared beam is spatially and temporally overlapped with a visible beam on the surface to generate a sum frequency output as shown in Figure 6-1.[23] SFG is a highly surface specific technique. Since, the SFG process is forbidden in bulk medium with inversion symmetry under the dipole approximation.[24]

The second-order susceptibility tensor $\chi_{eff}^{(2)}$, which can be described as the sum of a non-resonant part $\chi_{\mathrm{NR}}^{(2)}$ and resonant part $\chi_{\mathrm{R}}^{(2)}$, relates the induced second-order polarization response to the incident light intensity. The $\chi_{eff}^{(2)}$ is bridged to molecular hyperpolarizability $\beta^{(2)}$ through ensemble average over all possible molecular orientation shown in Equation 2-13.[25] Equation 2-12 is the basis equation for the nonlinear model fitting of SFG spectrum used for orientation analysis and mapping results. The Figure 6-2 presents the different SFG spectra line shapes of relative non-resonant phase (ϕ).

6.3. Experiment section

6.3.1. UHV-SFG-imaging setup

The polycrystalline platinum surface is mounted on sample stage in the UHV chamber. The sample stage is mounted on a sample holder which fastens to the magnetic transfer arm, so the sample stage can be transferred linearly from the main chamber to the SFG cell for 12 inches distance and rotated 360° around transfer arm. The magnetic transfer arm is attached to a XYZ manipulator, which can rotate, tilt and translate to give more flexibility of sample stage.

6.3.2. SFG imaging setup

SFG imaging was described in detail elsewhere.[26] The incidence angle of the IR and 1064 pump beams is set at 70º and 60º, while the emit angle of SFG beams is set at 62.1º, respectively from surface normal shown in Figure 6-1. The SFG microscope is set with a reflection configuration collecting the intermediated SFG beam profile. A Roper

Scientific CCD camera with 1024×1024 pixels array is used for signal collection. By continuously scanning IR frequency from 2000 to 2150 cm^{-1} in the fixed rate, total 31 images are produced and each image represents every 5 cm^{-1} IR wavenumber range. A series of images is stacked and extracted SFG spectrum via ImageJ software. Every SFG image is 1024×1024 pixels and 1 pixel is corresponding with about 1 μm distance on the surface.

6.3.3. Platinum preparation and TPD characterization

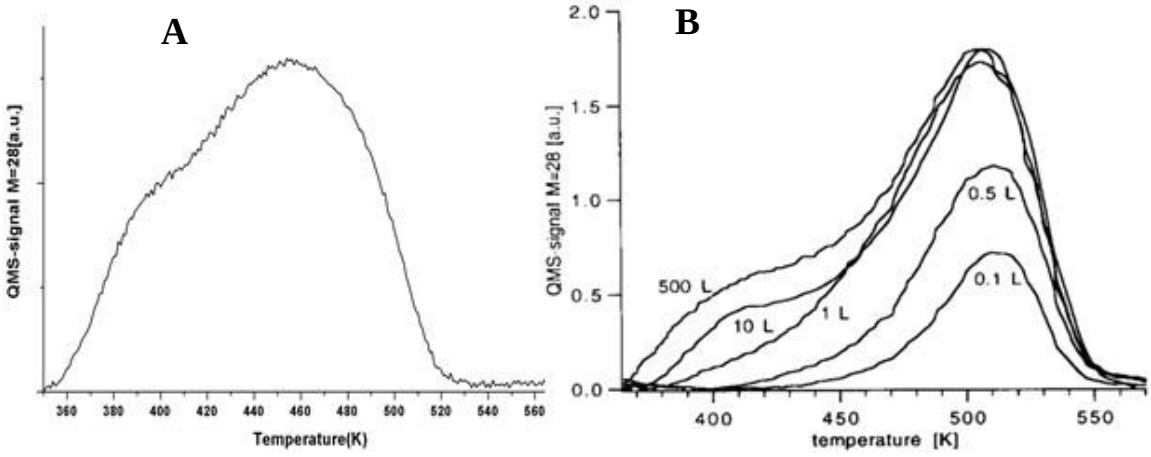

Figure 6-3: (A) TPD spectrum from this experiment; (B) TPD spectrum in Ertl's work.[27]

The platinum surface is prepared by using a standard method of successive polishing down to 0.01 μm diamond-ethanol slurry to produce a mirror-like surface and put into pirani solution for 30 min. Then platinum is mounted on sample stage in the UHV chamber. After pumping UHV down to base pressure, several cycles argon ion sputtering followed by surface oxidation at 800 K with oxygen pressure 10^{-6} Torr are applied. Then 120 Langmuir CO gas is dosed on sample at 330 K and 1 K/s linearly heating rate are applied to obtain a TPD spectrum. Keep annealing and ion sputtering cycle until obtaining

a stable TPD spectrum. Sample stage is transferred to the SFG cell and about 1 Torr CO combined 400 Torr N_2 is introduced into the SFG cell immediately. 2000-2150 cm^{-1} IR wavenumber range is used in the SFG imaging to obtain 31 SFG images into a stack.

TPD spectra of CO on platinum surface shown in Figure 6-3(A) has two peaks, which are located around 400 K and 460 K, respectively. This spectra exhibited similar features with the results reported by Ertl's work shown on Figure 6-3(B) on a polycrystalline platinum foil[27] and Bradshaw's work on a stepped platinum surface.[10] Hence, the polycrystalline platinum surface could be considered as a clean surface. Based on Bradshaw's assignment, the low temperature peak on TPD spectrum is resulted from the CO desorbed from terrace area while the high temperature peak is resulted from the CO desorbed from the step area.

6.4. Results and discussions

Figure 6-4A shows the SFG image of CO on platinum when the IR frequency is 2070 cm^{-1}. The whole SFG image is cut into 10×10 pixels squares with 10000 region of interest (ROI). Consequently, 10000 SFG spectra are extracted. Contour map of resonant amplitude and histogram of resonant frequency are obtained based on fitting each SFG spectrum corresponding with the 10000 ROIs via Equation 2-12 as shown in Figure 6-4B and Figure 6-4C. Meanwhile, a 750×750 pixels black square is employed for cropping the SFG image and extracting the corresponding SFG spectra, as well as another four 20×20 pixels square of different colors as shown in Figure 6-4A. The five spectra and fitting lines in five squares (based on equation 2-12) are shown in Figure 6-4D and the fitting parameters are listed in table 6-1. The different color of fitting line and word shown on

Figure 6-4A and Table 6-1 is corresponding with the different color squares shown on Figure 6-4A.

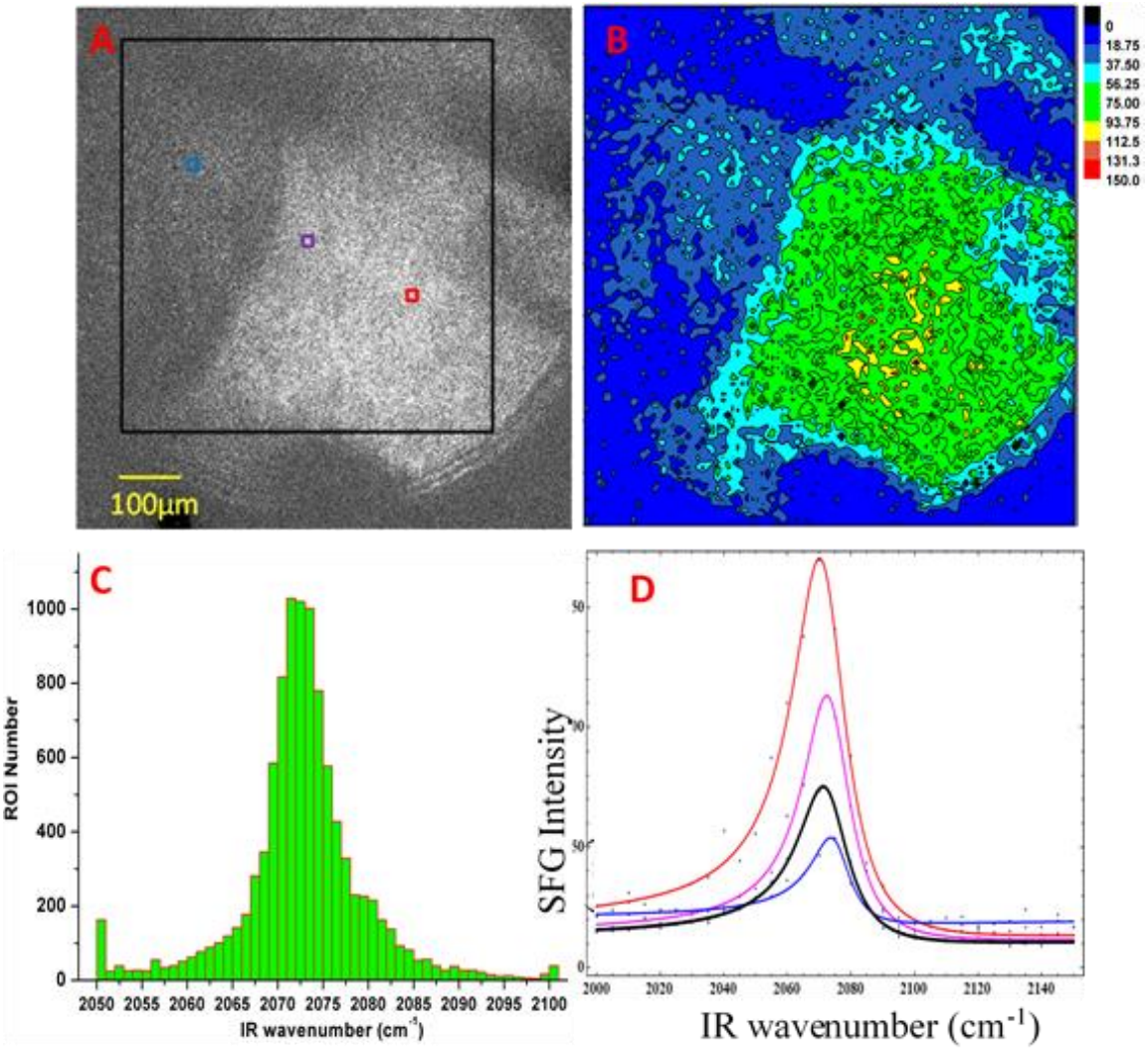

Figure 6-4: (A) SFG image of CO on platinum in 2070 cm^{-1} range. (B) Contour map of the resonant amplitude A_R. (C) Histogram of frequency (ω_q). (D) SFG spectrum (dot) and fitting line of corresponding color square area.

Based on Table 6-1 and Figure 6-4C, the resonant frequency of CO is around 2067-2077 cm^{-1}, which is unambiguously assigned to the vibration frequency of CO linearly bonded to platinum atom on the surface step. Previous studies demonstrated that the long time ion gun sputtering causes a formation of three dimensional defect structure on

platinum surface.[16] TPD results also proves that most of CO molecular desorbs from the surface step site. The domain structure shown in the Figure 6-4(A,B) is similar with Ertl's PEEM map on polycrystalline platinum domain shown in Figure 6-5.[28] The varying crystallographic orientation on polycrystalline platinum originates from the different coverage domain appears on surface.

Table 6-1. Fitting parameter of SFG spectrum in different color square, respectively

Square	A_{NR}	φ	A_q	$\omega_q(cm^{-1})$	$\Gamma(cm^{-1})$
750×750	3.48	1.02	52.44	2072.74	9.66
20×20	4.06	0.96	95.90	2071.53	10.22
20×20	3.65	1.06	65.87	2073.53	9.12
20×20	4.51	0.97	22.75	2075.34	7.48

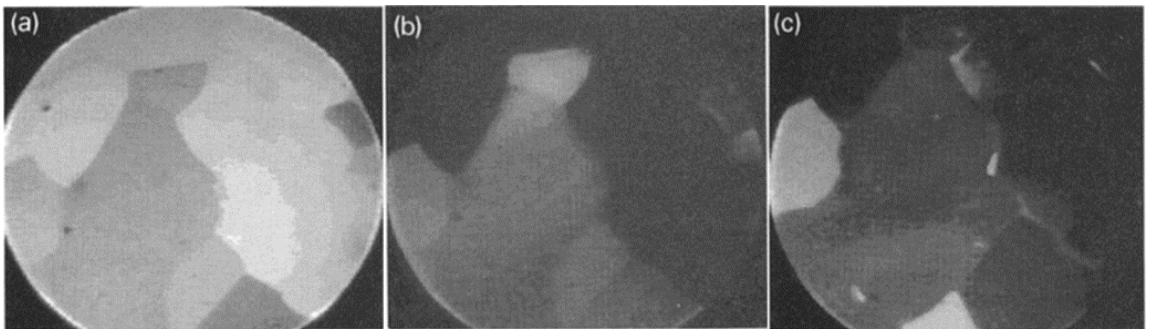

Figure 6-5: PEEM imaging (600×600 μm) of (A) clean platinum surface (B) after saturation with assorted oxygen at 433 K (C) under stationary reaction conditions at 433 K with $P(O_2)=4\times10^{-4}$ mbar, $P(CO)=1.22\times10^{-5}$ mbar.(Reproduced from Ertl's papers[28]).

Figure 6-6 demonstrates the statistically analysis of the SFG image about CO adsorption on the polycrystalline platinum surface. As shown in the histogram and contour map, it is clear that the resonant frequency of CO stretching vibration varies on different crystal domain areas.

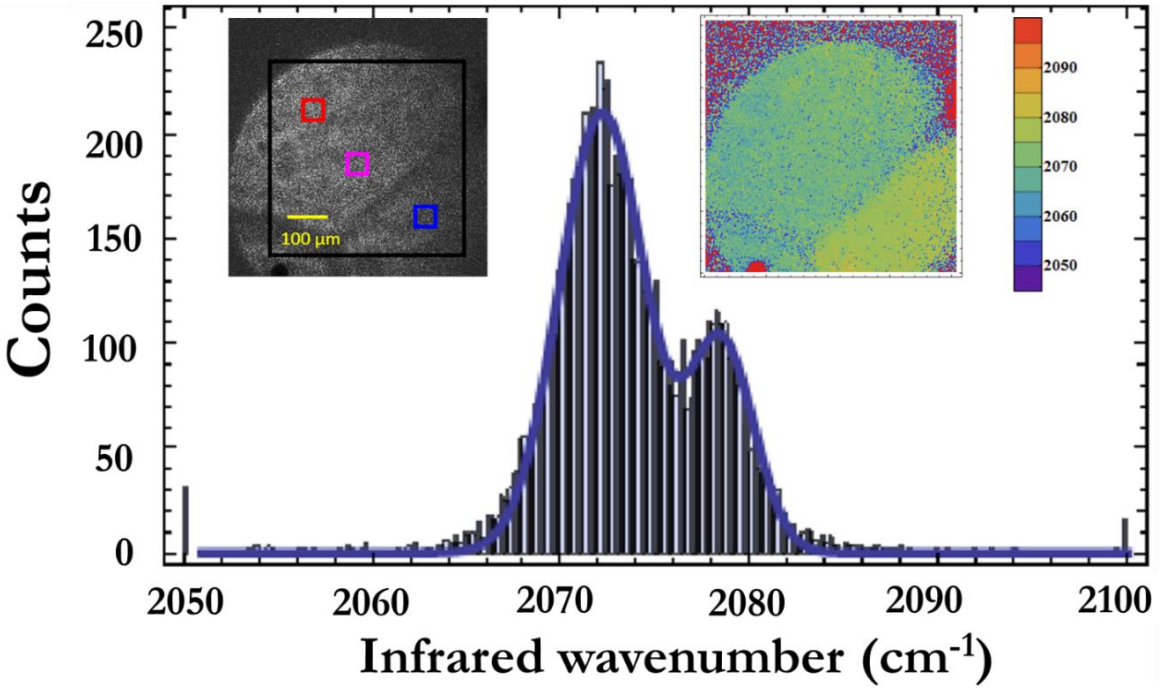

Figure 6-6: Statistically analysis about CO resonant frequency distribution on polycrystalline Pt surface.

6.5. Conclusion

UHV-SFG imaging set up IS successfully developed and applied on the CO adsorption on polycrystalline platinum under ambient pressure. TPD results demonstrates that a clean platinum surface is obtained in UHV and CO gas adsorbed on polycrystalline platinum surface at room temperature. The stretching vibration mode of linearly bonded of CO on polycrystalline platinum surface is identified by the SFG imaging. The resonant frequency of CO stretching vibration varies on different crystal domain areas. The domain structure on SFG image is related with the varying crystallographic orientation on polycrystalline platinum surface.

6.6. Reference:

(1) Myers, D. *Surfaces, interfaces, and colloids*; Wiley-Vch New York etc., **1999**.

(2) Vogel, D.; Spiel, C.; Suchorski, Y.; Urich, A.; Schlögl, R.; Rupprechter, G. *Surf. Sci.* **2011**, *605*, 1999.

(3) Langmuir, I. *T. Faraday Soc.* **1922**, *17*, 621.

(4) Klünker, C.; Balden, M.; Lehwald, S.; Daum, W. *Surf. Sci.* **1996**, *360*, 104.

(5) Barteau, M. A.; Ko, E. I.; Madix, R. J. *Surf. Sci.* **1981**, *102*, 99.

(6) Collins, D.; Spicer, W. *Surf. Sci.* **1977**, *69*, 114.

(7) McCabe, R.; Schmidt, L. *Surf. Sci.* **1977**, *65*, 189.

(8) Hopster, H.; Ibach, H.; Comsa, G. *J. Catal.* **1977**, *46*, 37.

(9) Norton, P.; Goodale, J.; Selkirk, E. *Surf. Sci.* **1979**, *83*, 189.

(10) Greenler, R. G.; Burch, K. D.; Kretzschmar, K.; Klauser, R.; Bradshaw, A.; Hayden, B. *Surf. Sci.* **1985**, *152*, 338.

(11) Ertl, G.; Neumann, M.; Streit, K. *Surf. Sci.* **1977**, *64*, 393.

(12) Lauterbach, J.; Haas, G.; Rotermund, H.; Ertl, G. *Surf. Sci.* **1993**, *294*, 116.

(13) Borg, A.; Hilmen, A.-M.; Bergene, E. *Surf. Sci.* **1994**, *306*, 10.

(14) Härle, H.; Lehnert, A.; Metka, U.; Volpp, H.-R.; Willms, L.; Wolfrum, J. *Chem. Phys. Lett.* **1998**, *293*, 26.

(15) Cimatu, K.; Baldelli, S. *J. Am. Chem. Soc.* **2006**, *128*, 16016.

(16) Klünker, C.; Balden, M.; Lehwald, S.; Daum, W. *Surf. Sci.* **1996**, *360*, 104.

(17) Su, X.; Cremer, P. S.; Shen, Y. R.; Somorjai, G. A. *Phys. Rev. Lett.* **1996**, *77*, 3858.

(18) Härle, H.; Lehnert, A.; Metka, U.; Volpp, H. R.; Willms, L.; Wolfrum, *Appl. Phys. B-Lasers O.* **1999**, *68*, 567.

(19) Härle, H.; Mendel, K.; Metka, U.; Volpp, H. R.; Willms, L.; Wolfrum, J. *Chem. Phys. Lett.* **1997**, *279*, 275.

(20) Kitamura, F.; Takahashi, M.; Ito, M. *Surf. Sci.* **1989**, *223*, 493.

(21) Baldelli, S.; Markovic, N.; Ross, P.; Shen, Y.-R.; Somorjai, G. *J. Phys. Chem. B* **1999**, *103*, 8920.

(22) Umrath, W. *Leybold, Cologne* **1998**.

(23) Potterton, E.; Bain, C. *J. Electroanal. Chem.* **1996**, *409*, 109.

(24) Buck, M.; Himmelhaus, M. *J. Vac. Sci. Technol. A* **2001**, *19*, 2717.

(25) Lu, R.; Gan, W.; Wu, B. H.; Chen, H.; Wang, H. F. *J. Phys. Chem. B* **2004**, *108*, 7297.

(26) Cimatu, K.; Baldelli, S. *J. Phys. Chem. B* **2006**, *110*, 1807.

(27) Ertl, G. *Surf. Sci.* **1994**, *299–300*, 742.

(28) Lauterbach, J.; Haas, G.; Rotermund, H. H.; Ertl, G. *Surf. Sci.* **1993**, *294*, 116.

CHAPTER 7. SMMMARY AND OUTLOOK

The work presented in this dissertation has mostly been focused on the surface chemistry studies on metal surface via SFG imaging. The study demonstrates that the analytical capabilities of SFG imaging offer valuable molecular level information regarding the molecular properties on heterogeneous metal surface. The main results are summarized together with an outlook on possible further development and studies.

The SFG imaging technique was developed to evolve from the SFG spectroscopy which relies on averaged signal into a surface microscopic technique. It could not only define the real spatial heterogeneity of the surface adsorbate on metal surface, but also visualize the relationship of the surface molecular properties with underneath copper substrate. Such ultimate advantage of SFG imaging brings new insight into studying dynamic processes including catalysis, corrosion and biology process on metal surface. Major observations in spatial correlation of surface molecule property such as monolayer orientation, conformation, and phase information with local metal structure have been achieved. In addition, the dynamic chemical process on metal surface is monitored as a transformation of the non-resonant phase and background of SFG spectra. The new generation SFG imaging setup is developed with higher spatial resolution and easier alignment strategy.

This first study focuses on the application of the new generation SFG imaging setup to measure the ambient pressure methanol adsorption on polycrystalline copper surface. It is shown that the methoxy species is generated by exposing the polycrystalline copper surface to methanol vapor at room temperature. In addition, the oxygen exposure brings a

direct effect on the surface coverage and conformation order of methoxy monolayer. By employing the statically analysis of SFG image, the monolayer order influenced by the oxygen exposure is demonstrated. The observation that the monolayer orientation distribution without oxygen is statistically broader than with oxygen proves the oxygen exposure promotes the surface adsorption of methanol and generates a more compact methoxy monolayer on copper surface. The second study focuses on the CO adsorption on a polycrystalline platinum surface via SFG imaging. SFG spectra identify the linearly bonded of CO adsorbed on the polycrystalline platinum surface. The statistical analysis of SFG image demonstrates that the resonant frequency of CO stretching vibration varies on the different crystal domain areas. In brief, these two studies address the unique power of SFG imaging in studying gas/metal interface and *in-situ* monitoring catalysis process with a significantly higher sensitivity to monolayer order.

SFG imaging has also been used to characterize ODT monolayer on microcrystalline copper surface wherein micrometer size crystal domain existed on copper surface. The crystal grain and grain boundaries of the copper surface are mapped in the SFG image based on the strong brightness contrast of the SFG signal across the boundary. Local SFG spectra reveal significant difference with each other, as well as the average SFG spectra, indicating the heterogeneity of the copper surface resulting from copper grains with distinct crystallographic facets and orientations. The SFG spectra demonstrate a feature anisotropy in different crystal domain. Such anisotropy resulted from the individual surface atom structure in different crystal grain. With the aid of statistical analysis of SFG imaging, the microcrystalline copper surface demonstrated a well-separated spatial distribution for non-resonant phase, orientation and conformation representing distinct

monolayer property in each crystal domain area. The statistical analysis allow to compare orientation distributions in different crystal grain and correlate the relationship between monolayer orientations with underneath copper structure.

A decade of SFG imaging studies has provides enlightening insights into a number of molecular level surface science studies on metal surface that were previous inaccessible previously. Currently, SFG imaging is becoming a more widespread technique. The development could be proved by the significant increase in the number of groups starting SFG imaging research. It can be expected that its range of applications will be significantly extended in the future. Besides that, with the progress in laser technology, the development of more powerful and stable laser removes the major obstacles to performing SFG imaging experiment. The SFG imaging continues to require less expertise. Plenty of room left for further development is concerned with improvement of higher spatial resolution and image acquisition time.

The field in which SFG imaging has already been applied very successfully and in which it is expected to make further significant contributions in the future is corrosion since it bridges the pressure gap and identified the surface heterogeneity.[1,2] Besides that, the unique opportunities for studies of dynamics and kinetics at metal surface have opened up new dimensions for the application of SFG imaging in heterogeneous catalysis. Biology will also likely to be a major field in which SFG imaging would make a significant contribution to understanding of cell, tissue, lipid layer on the molecular scale.

Reference:

(1) Cimatu, K.; Baldelli, S. *J. Am. Chem. Soc.* **2006**, *128*, 16016.

(2) Fang, M.; Santos, G.; Chen, X.; Baldelli, S. *Surf. Sci.* **2016**, *648*, 35.

APPENDIX A. Roles of Oxygen for Methanol Adsorption on Polycrystalline Copper Surface Revealed by Sum Frequency Generation Imaging Microscopy

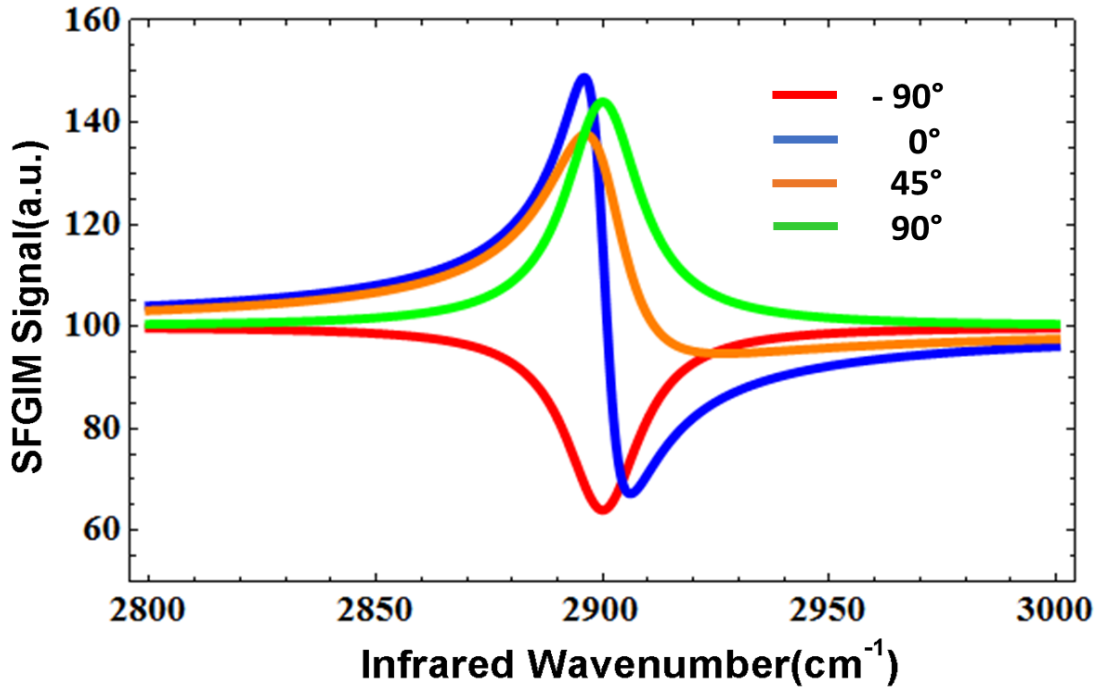

Figure A-1: Simulation curve of a SFG spectrum line shape with relative phase shift (ϕ) shown in equation 3 is equal to -90°,0°,45°,90°, which a single resonance at 2900 cm^{-1}.

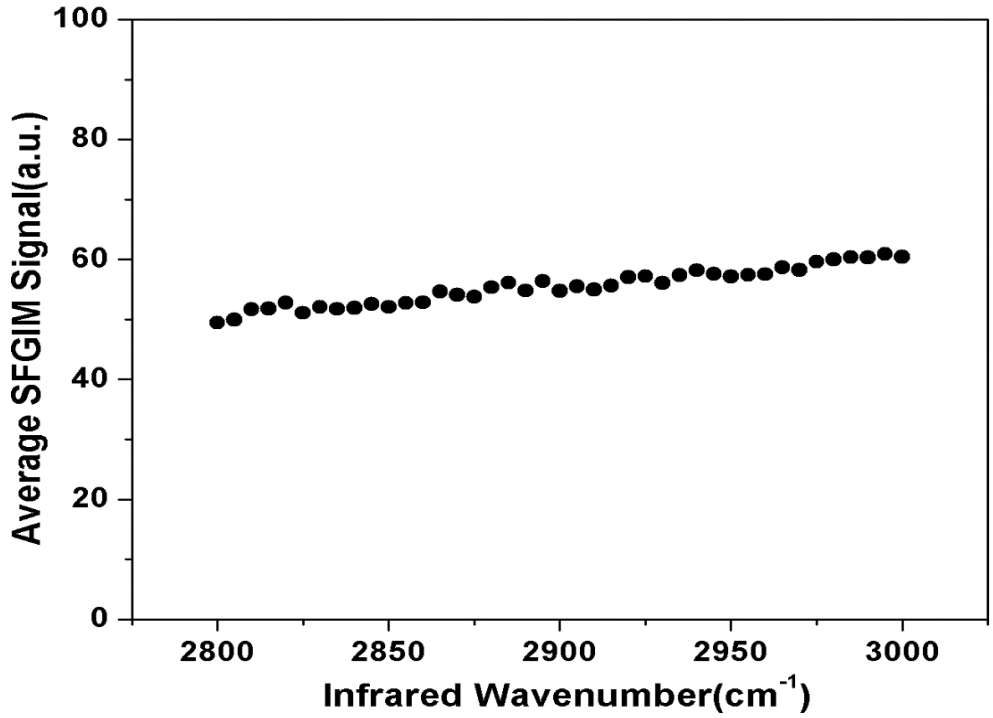

Figure A-2. The PPP-SFG spectrum of pure copper.

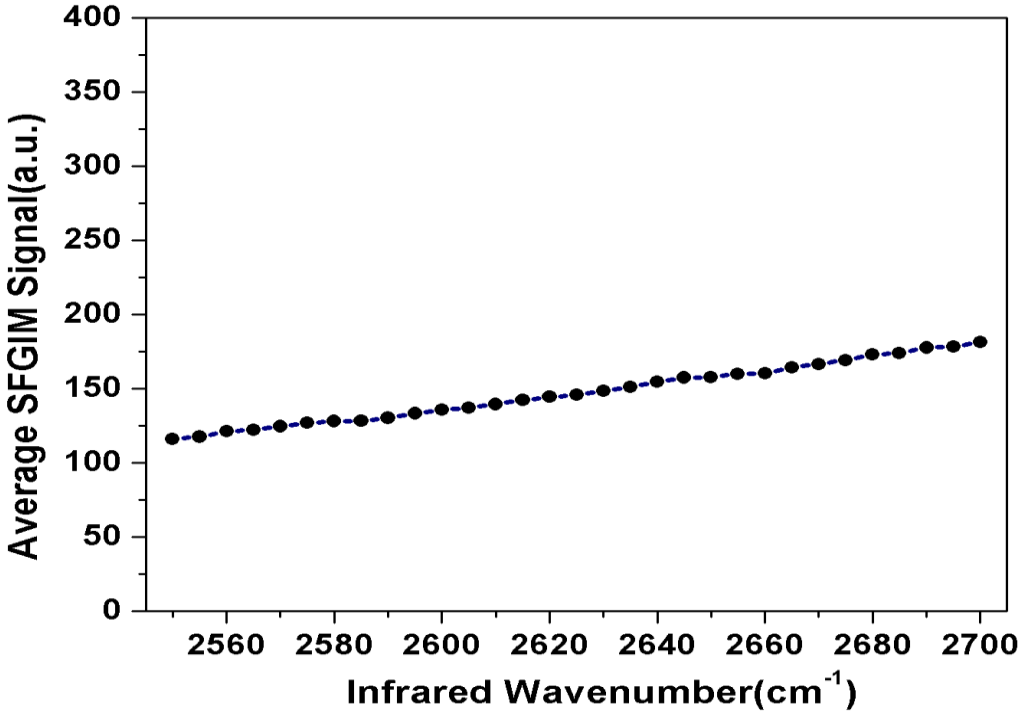

Figure A-3. The PPP-SFG spectrum of ambient pressure methanol (CH_3OD) with atmospheirc oxygen pressure in OD vibrational range.

APPENDIX B. Grain Structures and Boundaries on Microcrystalline Copper Covered with an Octadecanethiol Monolayer Revealed by Sum Frequency Generation Microscopy

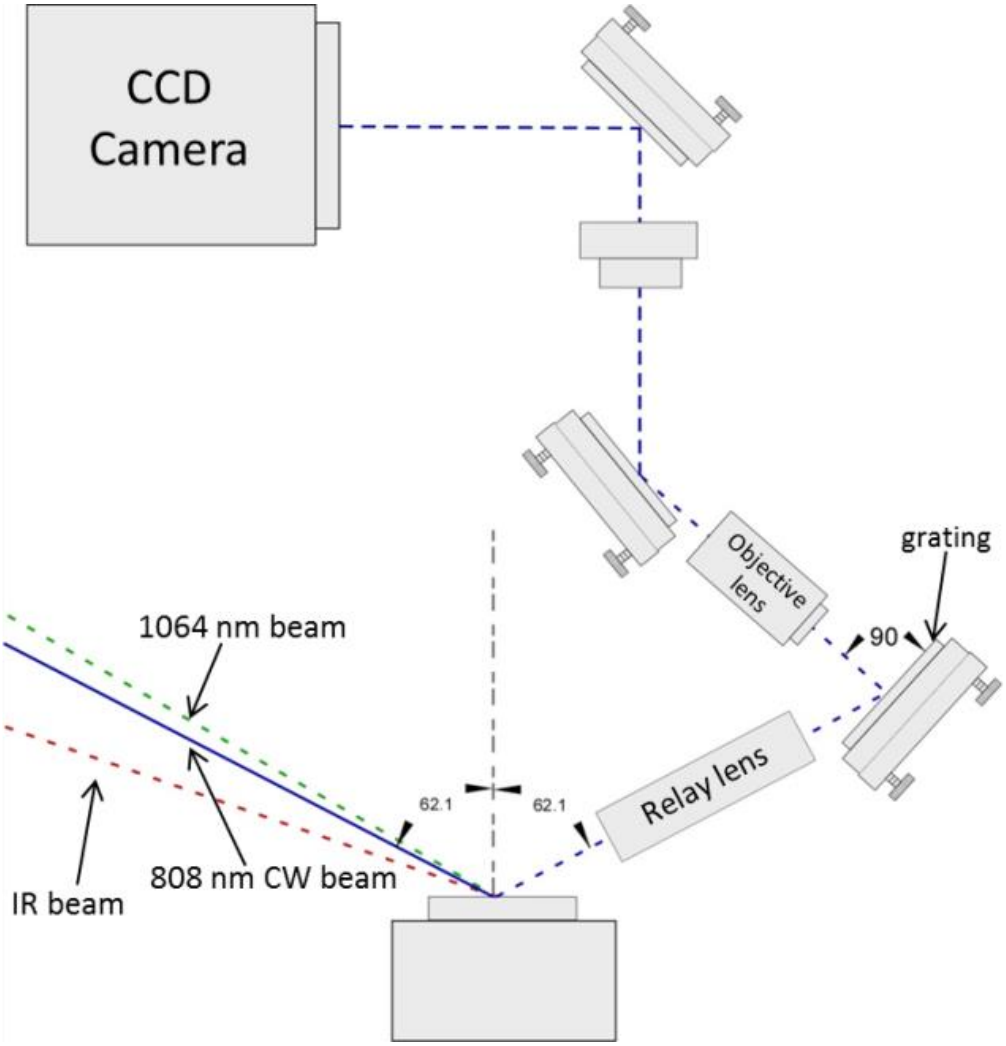

Figure B-1. Schematic diagram of SFG microscope and optical microscopes (wavelength, 808 nm).

Table B-1. Fitting parameters for SFG spectra in Figure 4-2(a)-2(f), respectively.

Azimuth angle	**0°**					
	A_{NR}(a.u.)	**Phase(ϕ)**	**A(r^+)**	**ω (r^+)**	**A(r^-)**	**ω (r^-)**
Average	22.35	1.35	37.8	2883	52.1	2969
Domain 1	21.85	0.96	39.6	2883	80.1	2972
Domain 2	12.28	2.70	89.7	2878	7.30	2969
Azimuth angle	**180°**					
	A_{NR}(a.u.)	**Phase(ϕ)**	**A(r^+)**	**ω (r^+)**	**A(r^-)**	**ω (r^-)**
Average	14.71	1.33	25.1	2882	37.4	2970
Domain 1	10.84	2.28	63.1	2880	19.6	2966
Domain 2	15.35	1.12	19.2	2882	49.4	2971

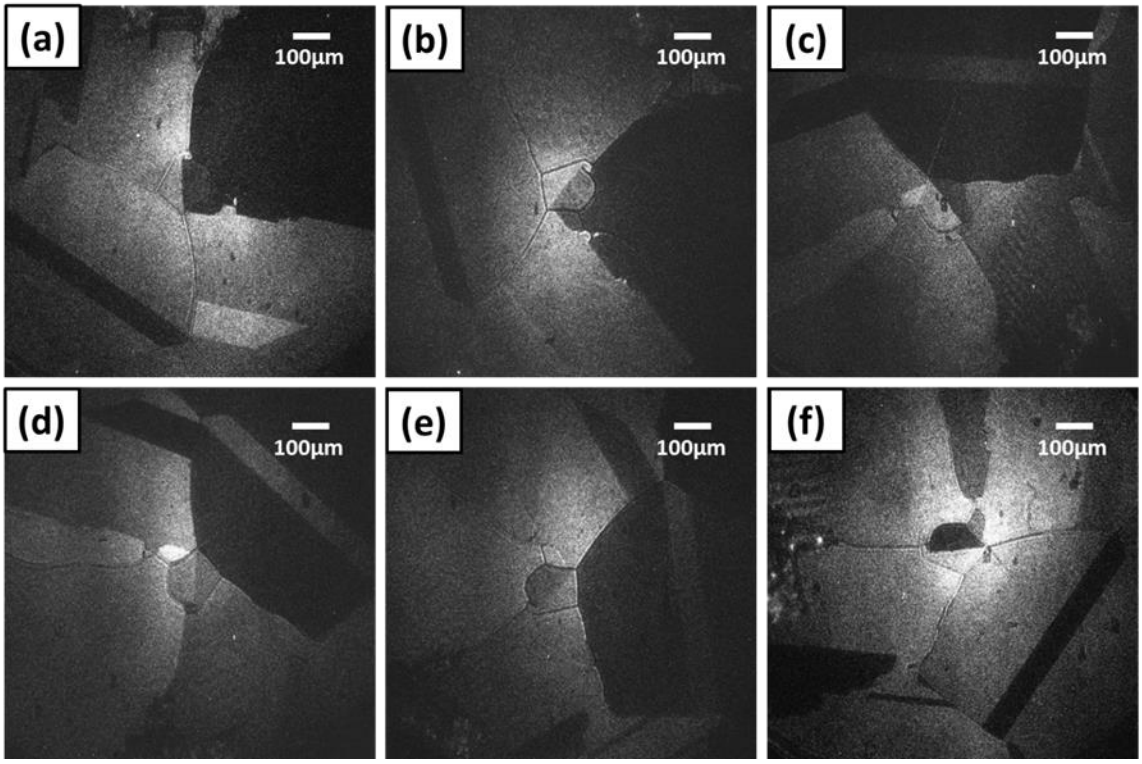

Figure B-2. Unprocessed SFG image (IR wavenumber: 2980 $cm^{-1)}$ of copper sample at the azimuth angle of 0°(a), 100°(b), 135°(c), 180°(d), 220°(e), and 320°(f), respectively.

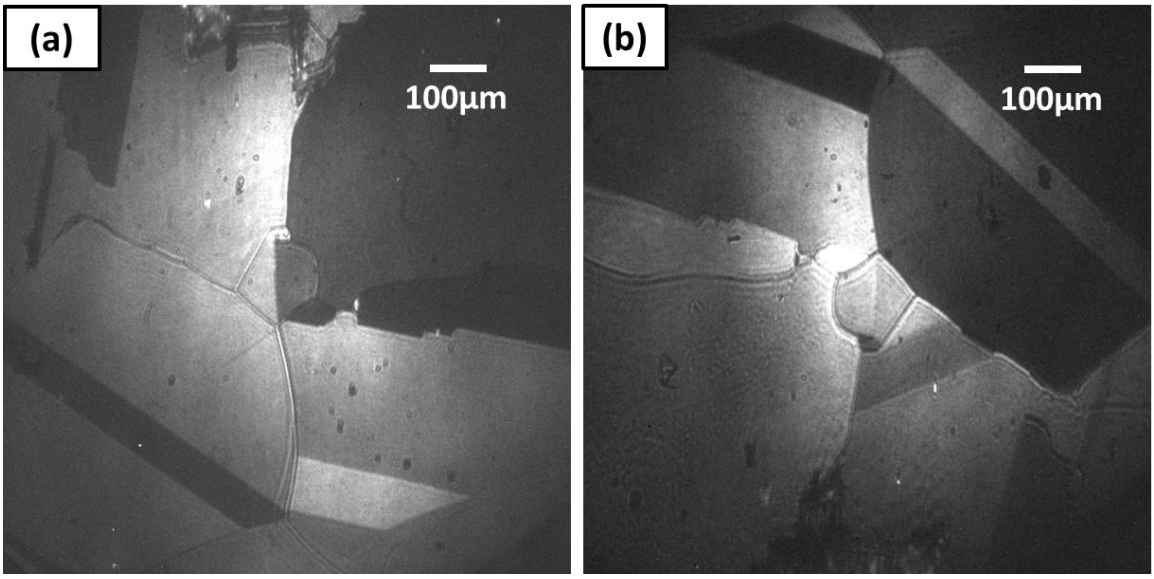

Figure B-3. Unprocessed SFG average image (IR wavenumber: 2700-3050 cm^{-1}) at the azimuth angle of 0° (a) and 180° (b), respectively.

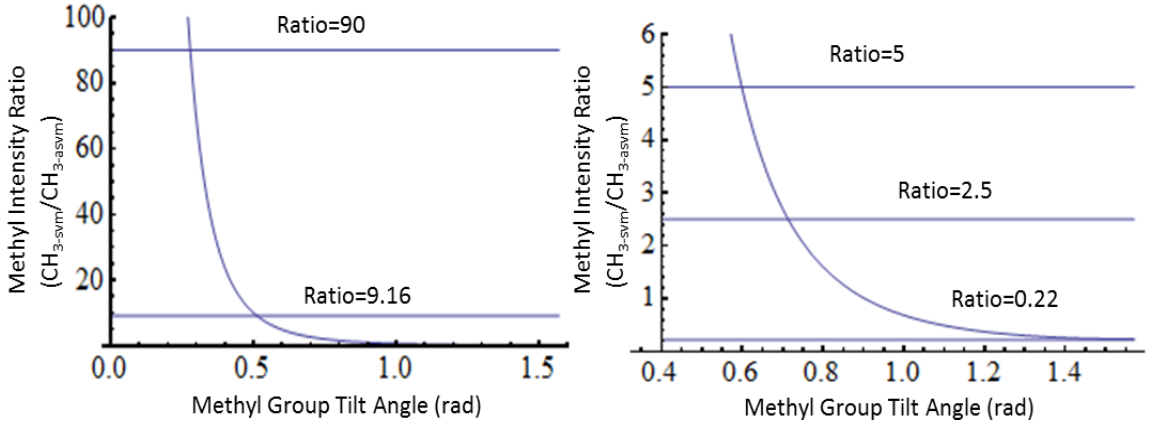

Figure B-4. Theoretical curve simulating the amplitude ratio of $CH_{3\text{-sym}}/CH_{3\text{-asym}}$ as the function of the tilt angle of methyl group.

Theoretical background of Figure B-4:

In this work, the orientation analysis is based on the amplitude ratio of $CH_{3\text{-sym}}/CH_{3\text{-asym}}$.[1-3] The methyl group is approximately treated as C_{3v} symmetry. A δ function distribution is assumed for the tilt angle of methyl group, isotropic distribution is assumed

for the rotation angle and azimuthal angle. The C-H bond polarizability model and formulas from Hirose et al.[4] and Wang et al.[5] is used. Fresnel factors were calculated based on the model presented by Zhuang et al.[6]

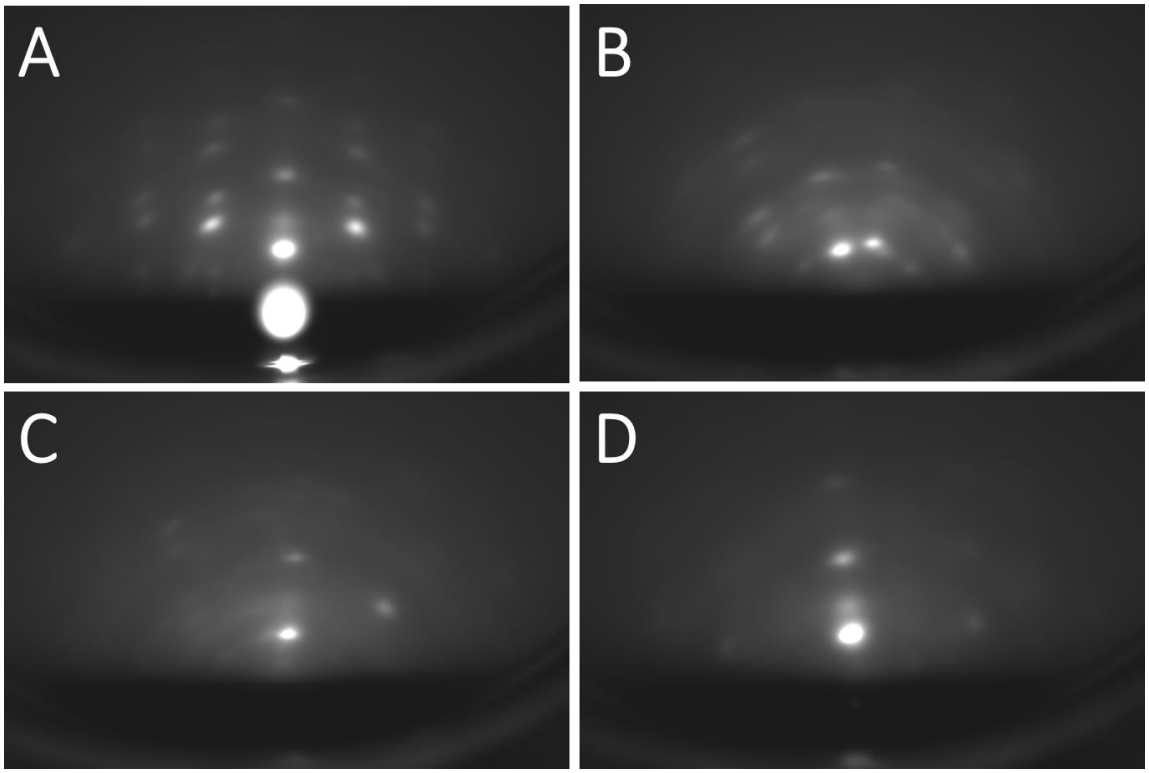

Figure B-5: (A-D) RHEED patterns of four different area on the microcrystalline copper surface.

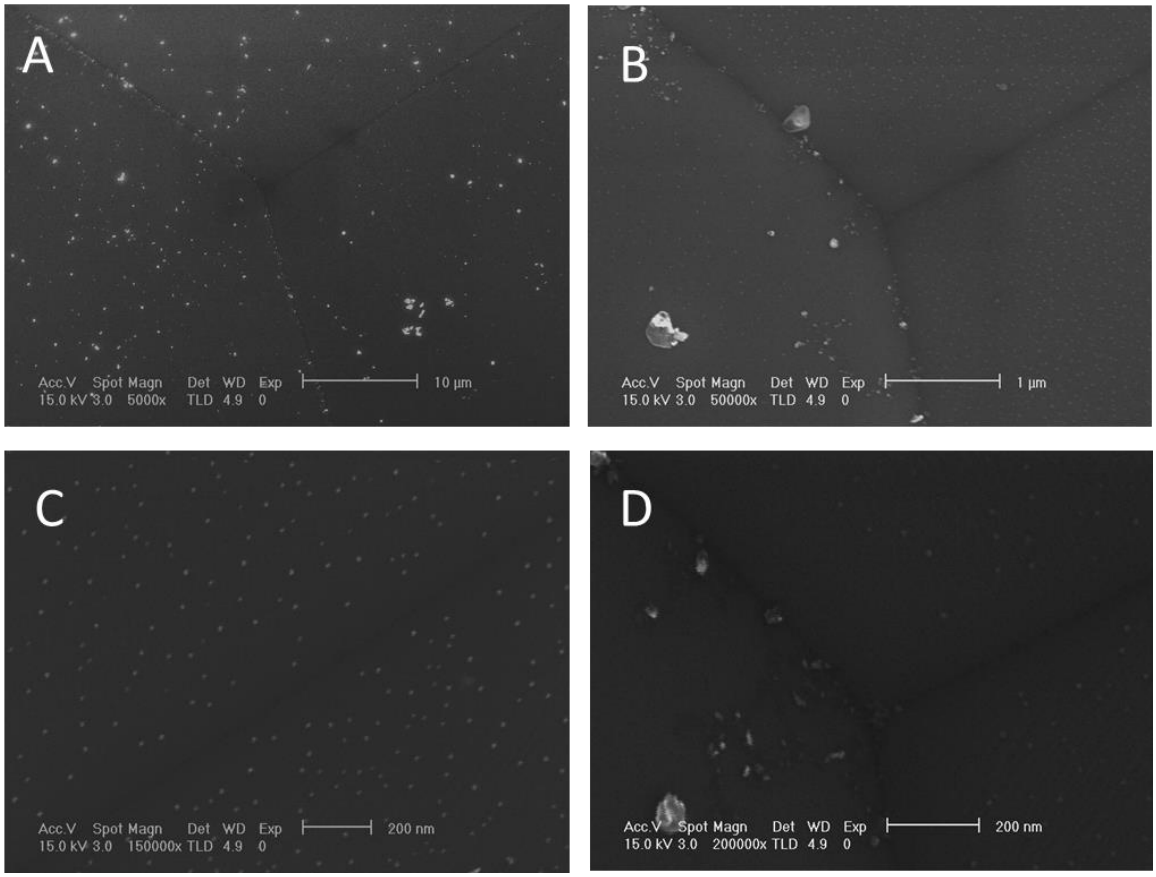

Figure B-6: (A-D) SEM image of microcrystalline copper surface in different position

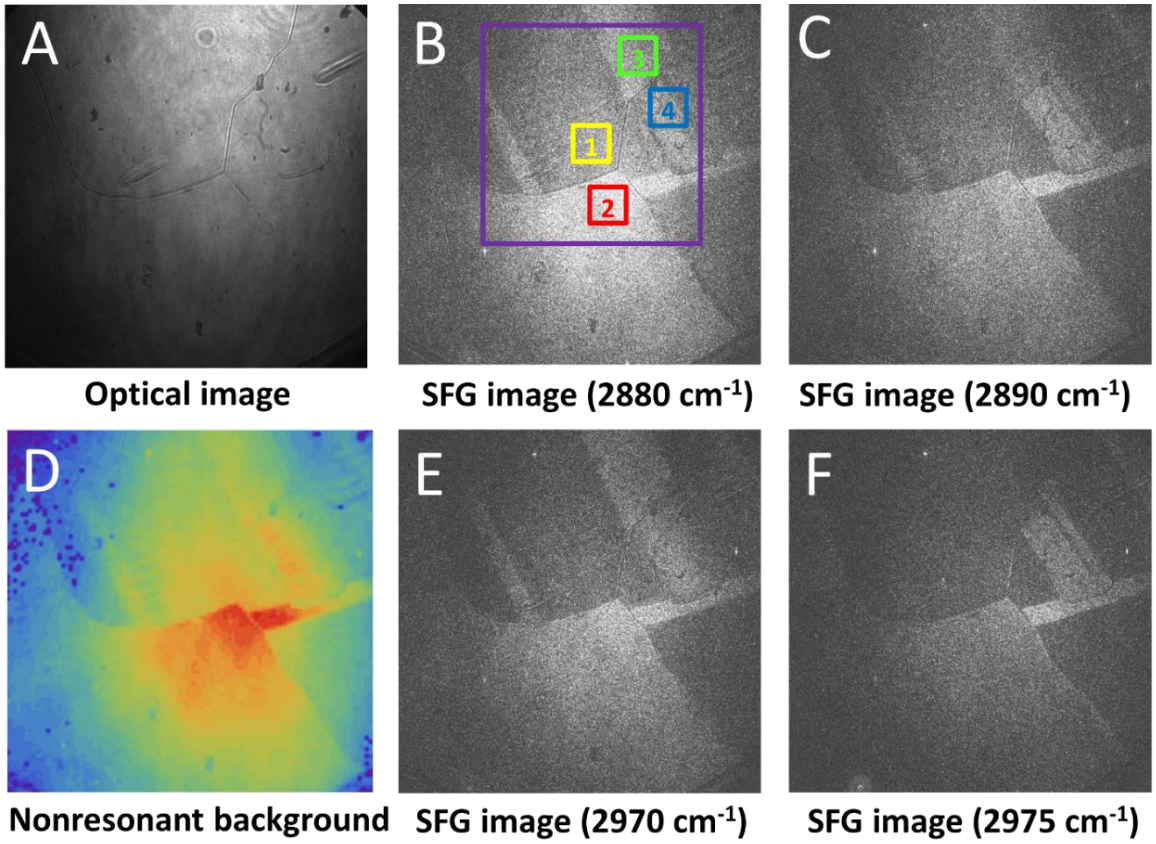

Figure B-7: (A) Optical image, (B, C, E, F) SFG image and (D) chemical image of microcrystalline copper surface in different position

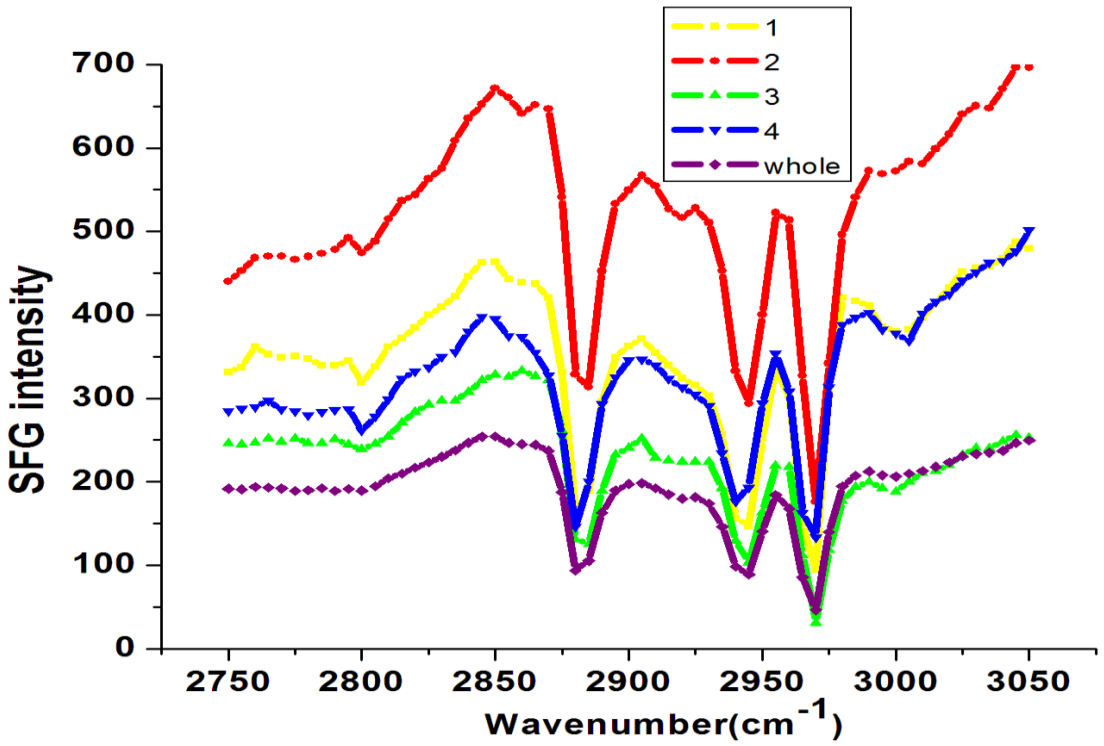

Figure B-8: SFG spectra in different area shown in Figure B-7

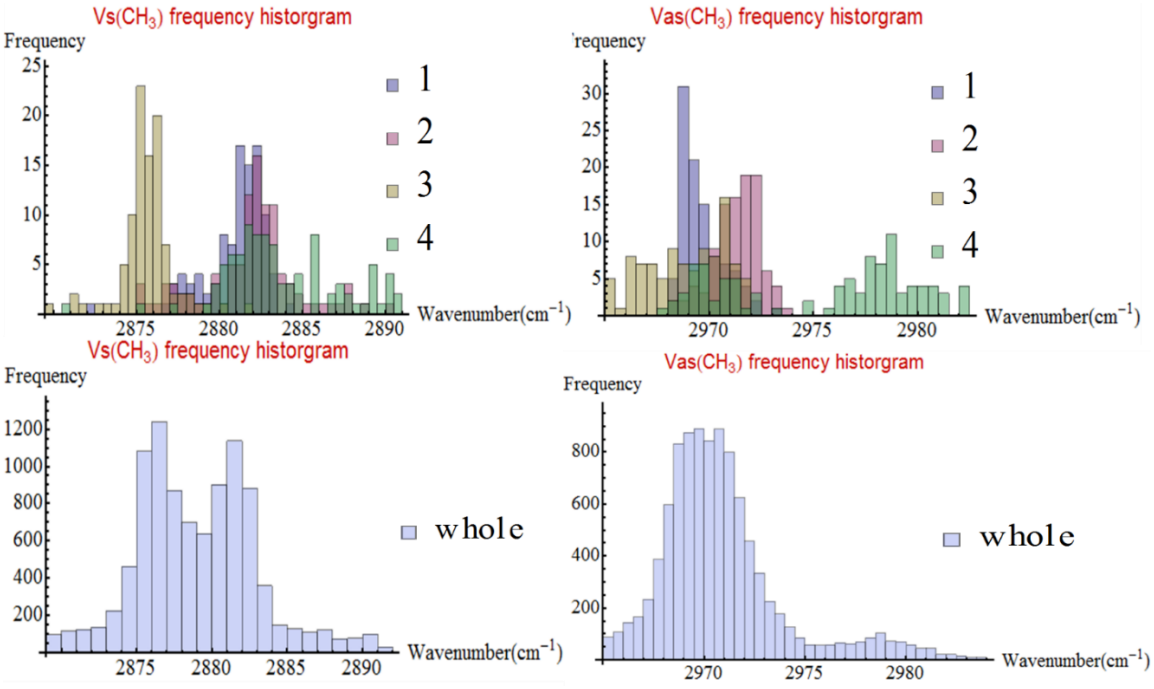

Figure B-9: Resonant frequency distribution in different area shown in Figure B-7

Reference:

(1) Guo, Z.; Zheng, W.; Hamoudi, H.; Dablemont, C.; Esaulov, V. A.; Bourguignon, B. *Surf. Sci.* **2008**, *602*, 3551.

(2) Cecchet, F.; Lis, D.; Guthmuller, J.; Champagne, B.; Caudano, Y.; Silien, C.; Mani, A. A.; Thiry, P. A.; Peremans, A. *Chemphyschem* **2010**, *11*, 607.

(3) Zhang, H. P.; Romero, C.; Baldelli, S. *J. Phys. Chem. B* **2005**, *109*, 15520.

(4) Hirose, C.; Yamamoto, H.; Akamatsu, N.; Domen, K. *J. Phys. Chem.* **1993**, *97*, 10064.

(5) Wang, H. F.; Gan, W.; Lu, R.; Rao, Y.; Wu, B. H. *Int. Rev. Phys. Chem.* **2005**, *24*, 191.

(6) Zhuang, X.; Miranda, P. B.; Kim, D.; Shen, Y. R. *Phys. Rev. B* **1999**, *59*, 12632.

APPENDIX C. Conformation Order of an Octadecanethiol Monolayer on Microcrystalline Copper Revealed by Sum Frequency Generation Microscopy

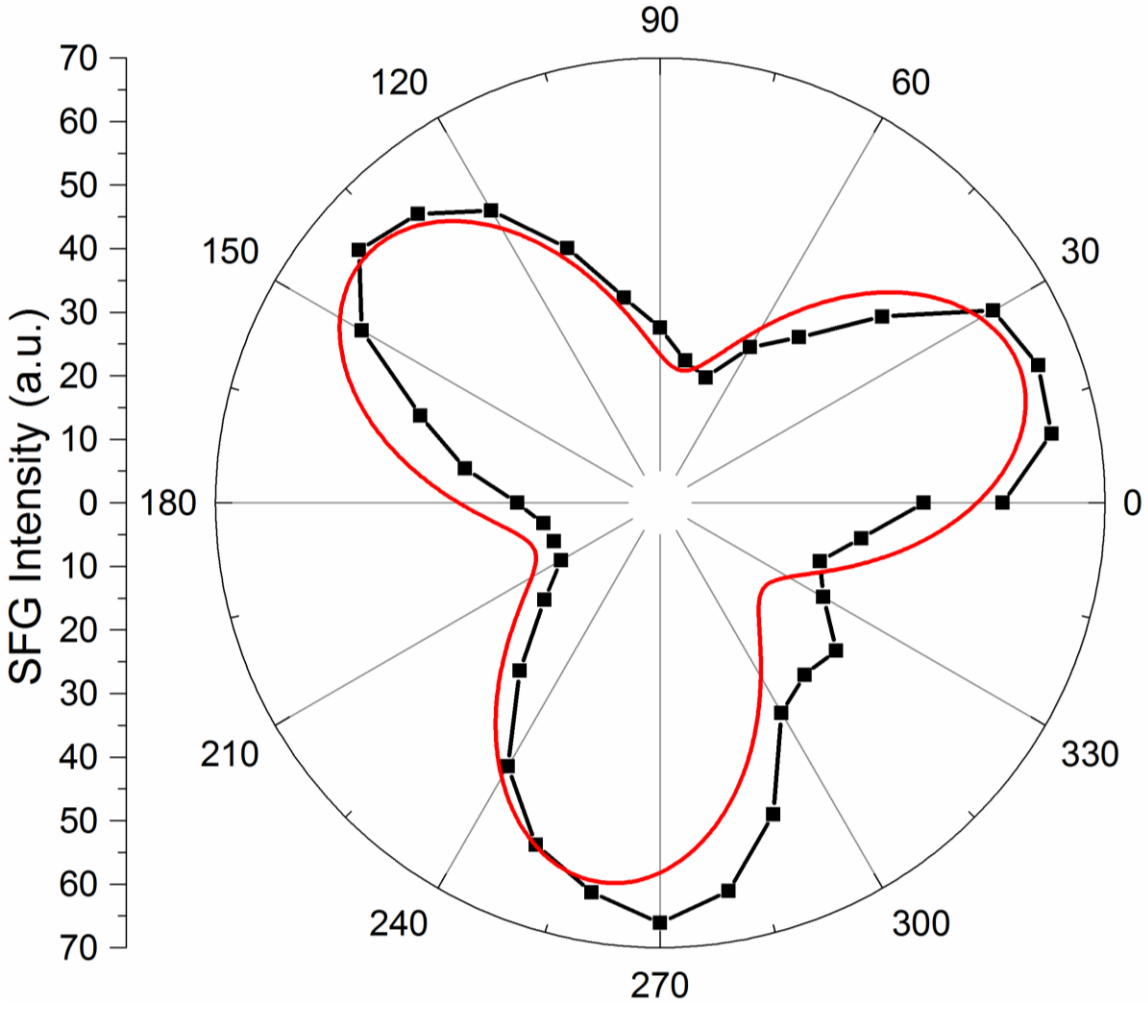

Figure C-1. Rotation anisotropy of the SFG intensity of pure Cu (111) at 3000 cm^{-1} monolayer. The solid line shows the fitted curve to Equation 5-2.

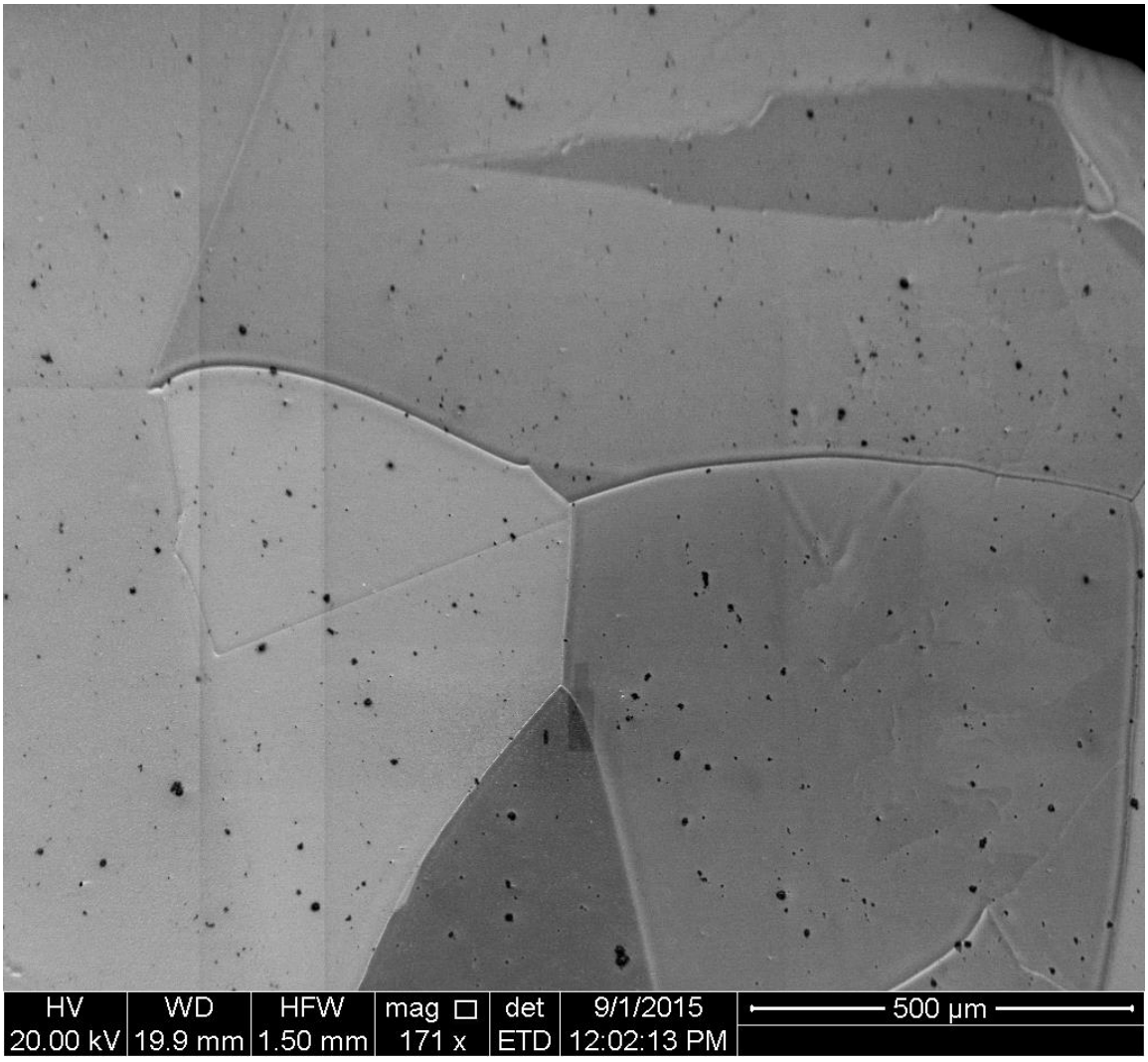

Figure C-2. SEM imaging of the copper surface with ODT monolayer

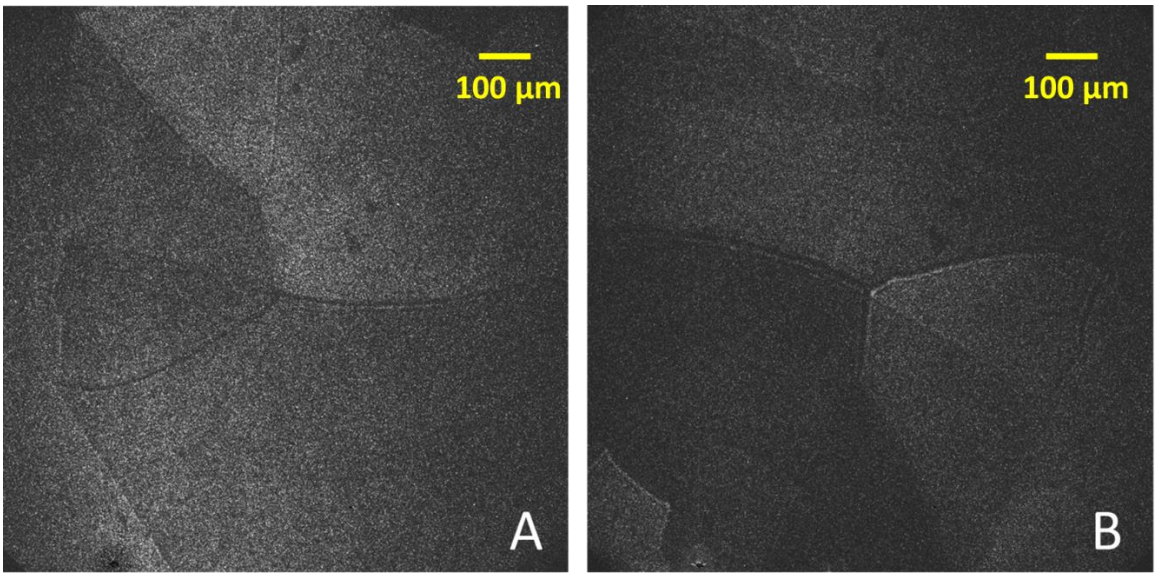

Figure C-3. SFG image (2980cm^{-1}) of the copper surface with ODT monolayer with azimuthal angle of 80°(A) and 240°(B), respectively.

APPENDIX D. Octadecanethiol (ODT) Monolayer on Copper & Silver Strips Pattern Surface

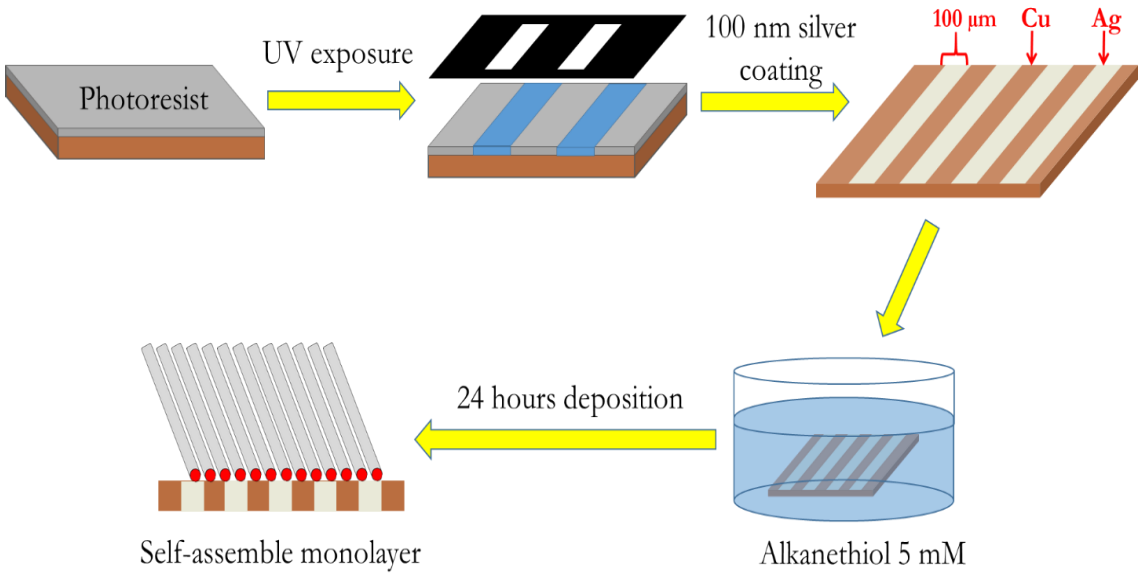

Figure D-1: Experimental schematic sketch of sample preparation about Ag/Cu bimetal sample surface

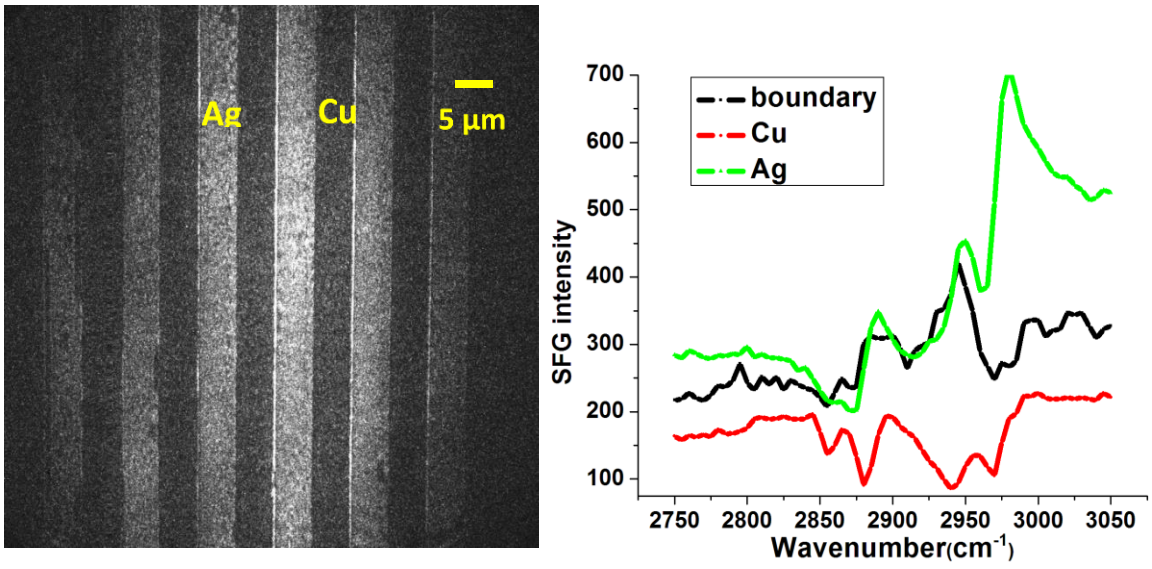

Figure D-2: (A) SFG image of octadecanethiol (ODT) on copper & silver strips pattern surface (2980cm^{-1}). (B) PPP SFG spectrum of octadecanethiol (ODT) on copper & silver strips pattern surface.

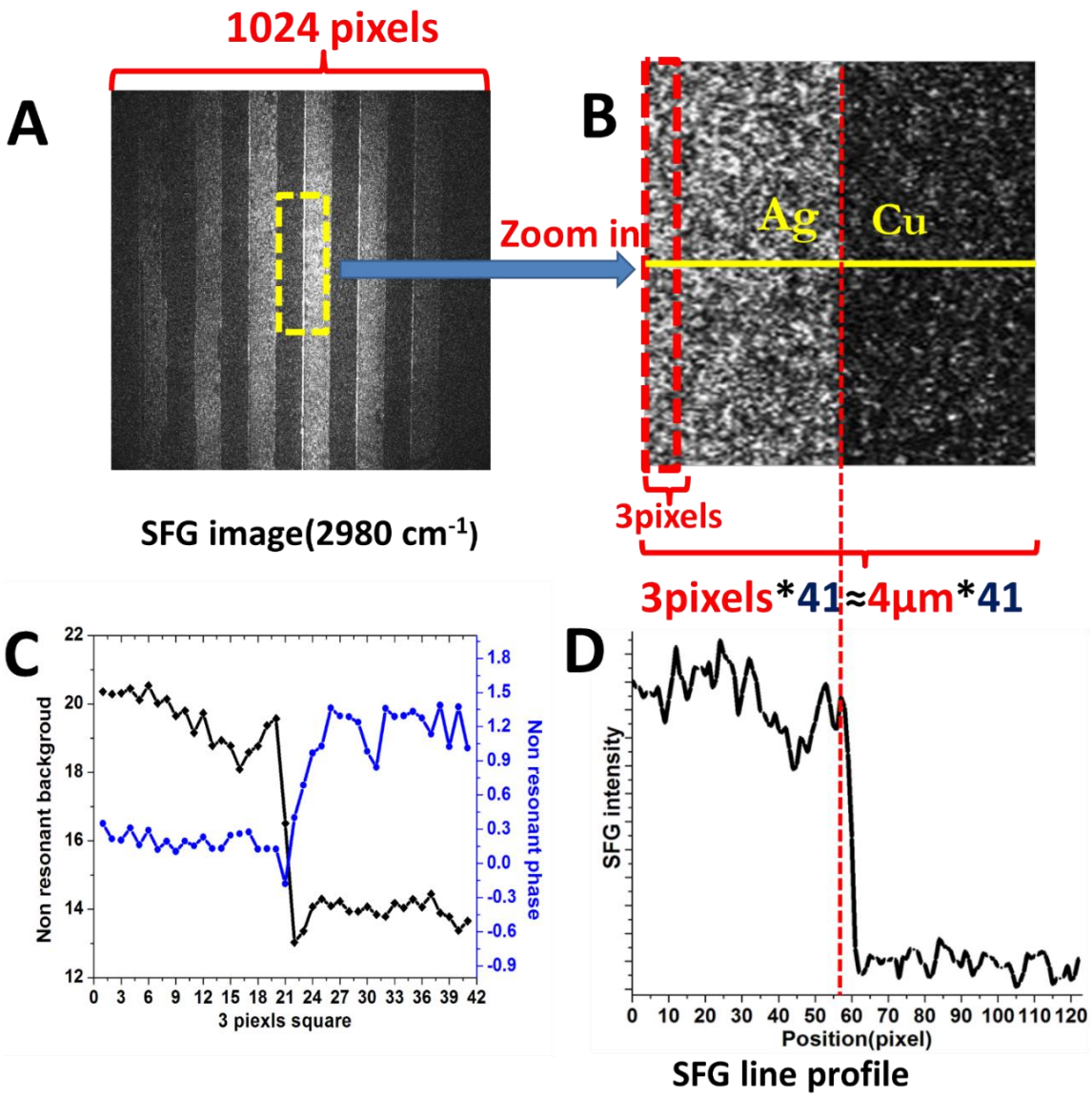

Figure D-3: (A) SFG image (B) Magnified SFG image of octadecanethiol (ODT) on copper & silver strips pattern surface (2980cm^{-1}). (C) Fitting results of non-resonant background and nonlinear phase. (D) Lineprofile across the SFG image.